Phil. Trans. R. Soc. Lond. A **301**, 163–181 (1981) [163]
Printed in Great Britain

ON NEWTONIAN AND NON-NEWTONIAN FLOW IN COMPLEX GEOMETRIES

BY T. COCHRANE†, K. WALTERS AND M. F. WEBSTER
Department of Applied Mathematics, University College of Wales, Aberyswyth SY23 3BZ, U.K.

(*Communicated by Sir Granville Beynon, F.R.S. – Received 7 October* 1980)

[Plates 1–13]

CONTENTS

A flow visualization technique by means of an expanded laser beam and trace amounts of particulate additives is used to study the behaviour of Newtonian and non-Newtonian elastic liquids in a number of complex geometries. Particular attention is paid to the effect of fluid elasticity on the flow characteristics.

Attempts are made to simulate numerically the observed flows by using finite-difference techniques. The agreement between theory and experiment is very satisfactory.

1. INTRODUCTION

Many fluids of industrial importance exhibit flow characteristics that cannot be predicted on the basis of the Navier–Stokes equations (cf. Walters 1980). Such fluids are called non-Newtonian. The polymer melts and polymer solutions used in plastics processing and fibre spinning are well known examples of non-Newtonian fluids, as are multigrade oils, liquid detergents, paints and printing inks. In industry, such fluids are often processed in complex geometries and there is a widely acknowledged need to understand the behaviour of non-Newtonian fluids in flows involving abrupt changes in geometry. This is especially so if the

† Present address: Department of Medical Electronics and Computing, St Bartholomews Hospital, London EC1A 7BE, U.K.

fluids in question have a built-in memory of past deformation and can be classified as non-Newtonian *elastic* liquids. There is then an important interplay between fluid memory and the rapid changes in flow characteristics expected near abrupt changes in geometry.

In a steady simple shear flow with velocity components given (in a rectangular Cartesian reference frame x^i)† by

$$v^1 = qx^2, \quad v^2 = v^3 = 0, \tag{1}$$

where q is a constant velocity gradient or shear rate, elastic liquids have corresponding stress components given by

$$\left.\begin{aligned} p^{12} &= \tau(q) = q\eta(q), \\ p^{11}-p^{22} &= \nu_1(q), \quad p^{22}-p^{33} = \nu_2(q). \end{aligned}\right\} \tag{2}$$

The viscosity $\eta(q)$ is usually a monotonic decreasing function of the shear rate q, and the corresponding normal stress differences ν_1 and ν_2 (especially ν_1) can be substantial and important.

In an extensional flow, the relevant extensional viscosity can be very high indeed (especially for some mobile polymer solutions), implying that such materials offer much higher resistance to stretching motions than they do to a shearing flow (cf. Petrie 1979).

In the experiments to be described in §2, we have chosen to work with the so-called Boger (1977/8) fluid which is a dilute solution of polyacrylamide in a syrup–water base. Over a reasonable range of shear rates, the Boger fluid can have a viscosity that is sensibly constant and yet possess a first normal stress difference ν_1 that is significantly greater than the shear stress, indicating a high level of elasticity in the fluid. To a sufficient approximation, ν_1 is found to be a quadratic function of shear rate q, and ν_2 is zero (cf. Walters 1980, p. 13; Keentok *et al.* 1980).

A note of caution is in order at this point. Rheometrical measurements over a reasonable shear-rate range (0–100 s^{-1}, say) may indicate that the Boger test fluid has a so-called 'second-order' behaviour, but conditions near abrupt changes in geometry are very severe and may represent circumstances that are well outside the rheometrical measurements made on the test fluid. This means that we should not necessarily expect second-order behaviour to pertain at all points of a complex flow field. At the same time, the use of the Boger fluid has a significant advantage over other test polymer solutions in that we are at least able to compare flow characteristics for elastic and Newtonian liquids at essentially the same Reynolds number, and the often dominating shear-thinning effect found in other test fluids is not so conspicuous. This means that changes in flow characteristics between the Boger fluid and a corresponding Newtonian syrup–water mixture can be mainly attributed to elastic memory effects.

In this paper, we shall investigate the flow behaviour of Newtonian and elastic liquids in a number of complex geometries. Our motivation is threefold. First, we have a general interest in the overall flow characteristics of fluids in complex geometries. Secondly, we wish to investigate how these characteristics are affected by fluid elasticity. Lastly, we are concerned with the possibility of numerically simulating the flows by using modern developments in computing mathematics.

† We use standard tensor notation. Covariant indices are written as subscripts, contravariant indices as superscripts, and the usual convention for repeated indices is assumed.

2. Experimental

(*a*) *Apparatus*

The flow system is shown schematically in figure 1. The bulk of the 10 l of test fluid is contained in the reservoir (A). The fluid is circulated by a Watson–Marlow type HRSV variable flow-rate peristaltic pump (B). Damping bottles (C) are introduced as a buffer volume to smooth out the flow. The test fluid flows through a long entry tube, through the test geometry (D) and back to the main reservoir. A by-pass system (E) is included to allow variation of the flow rate through the geometry. Flow rates are measured by timing the collection of a given volume of fluid through the measuring arm (F). Temperature is controlled to within 0.5 °C by the water bath (G) which has both an electric heating coil and a water-cooled coil.

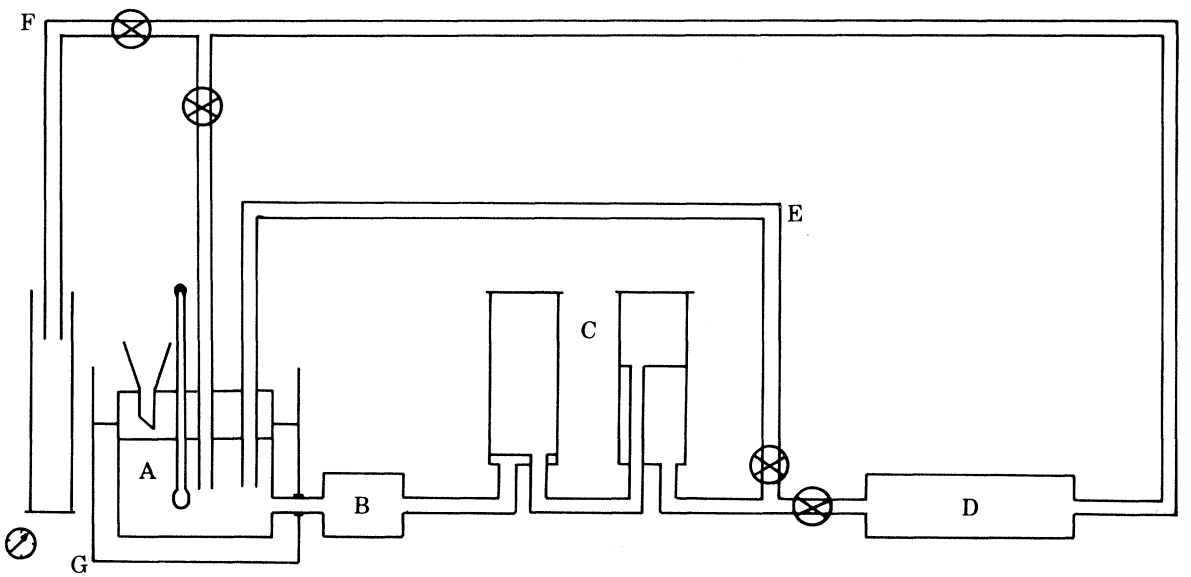

Figure 1. The flow system: A, reservoir; B, pump; C, damping bottle; D, test geometry; E, by-pass; F, flow-rate measurement arm; G, temperature control bath.

Typical flow rates range from 0–20 ml s^{-1} for a Newtonian liquid of viscosity 0.1 Pa s. This allows a maximum Reynolds number of approximately 40.

All the test sections have a depth of 20 mm and the various cross sections available are shown schematically in figure 2, together with the relevant dimensions.

In the present investigation, interest centres on flow visualization. In the past, opaque dyes have often been used for this purpose. Usually one has to insert the dye upstream of the region of interest and wait for the flow pattern to develop before photographing it against a high contrast background. Often, the streamlines are not clearly defined. A further disadvantage is that the test fluid is contaminated by successive additions of dye and soon becomes opaque to any illumination.

Several workers have recently used small tracer particles in conjunction with optical illumination to visualize steady flows. Mackley (1978) has studied Newtonian and non-Newtonian flow between rotating rollers, while Cable & Boger (1978) have used the technique to examine

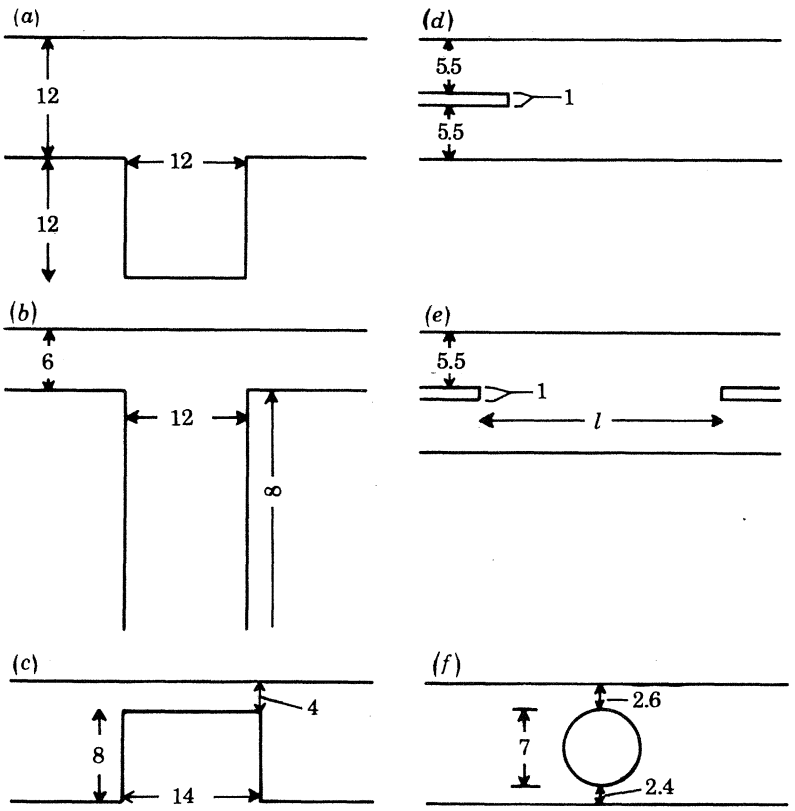

FIGURE 2. Schematic diagram of experimental geometries; all dimensions are in mm: (*a*) square hole, (*b*) deep hole, (*c*) protuberance, (*d*) mixing and separating (reversed), (*e*) mixing and separating, variable gap *l*, (*f*) cylinder.

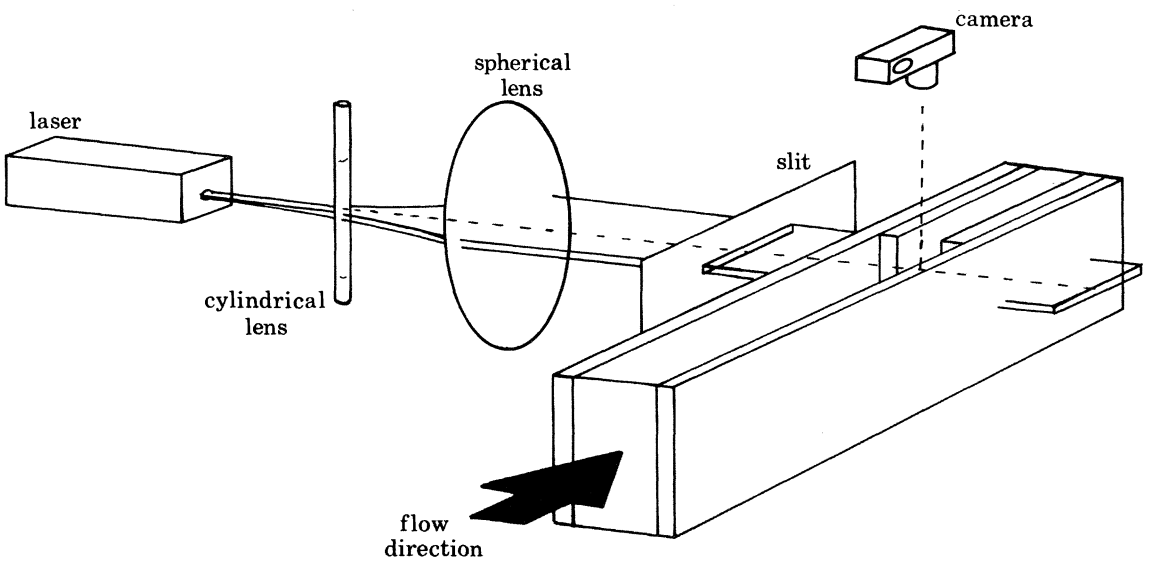

FIGURE 3. Flow-visualization apparatus.

vortex characteristics in tubular entry flows. More recently still, interest has centred on flows past bluff bodies, flows past a cavity or hole and flows near a sharp corner (Taneda 1979).

In the present work, we have resorted to a simple visualization technique which requires only trace amounts of particulate additives and which uses an expanded laser beam as illuminating source. A diagram of the arrangement is shown in figure 3.

A 5 mW helium–neon laser (Spectra Physics Model 120) is spread into a narrow sheet of light by means of a cylindrical lens. This sheet is collimated by using a large spherical lens. The collimated strip of light illuminates the plane of interest. This is then photographed by using a conventional camera mounted vertically above the flow. Since the amount of light available is low, a fairly fast film speed is necessary. We have used Kodak Tri-x Pan or Ilford HP 5 film uprated in development to 1200 ASA equipment film speed. If necessary, neutral density filters can be included in the optical path to control the degree of continuous illumination of the flow field.

The principle of the method is simple. Small particles, contained in and moving with the fluid, scatter light on entering the measuring plane. When developed, the photographs of the streaklines give a visual representation of the flow.

The selection of ideal scattering particles will depend on the liquid under investigation. After detailed consideration, we have found it convenient to use Hostalen GUR, a high density polyethylene powder (Hoechst, U.K.) as the seeding material. The grain size of this powder when in suspension is of the order of 0.1 mm diameter and the particles have a density of 0.94 g cm^{-3} so that they are suitable for liquid media having a density near that of water. They are also inert, have good light scattering characteristics and are of a fairly uniform size. For more dense media, polyvinyl chloride particles with a density of 1.4 g cm^{-3} may be used.

As an optimum concentration, we have found it convenient to use 2 g of powder in every 10 l of liquid.

(*b*) *Test fluids*

The Newtonian liquids used in the experiments are high maltose syrup–water mixtures, whose viscosities are determined by using a Brookfield viscometer.

The so-called Boger (1977/8) liquid provides a convenient elastic test liquid. It is a dilute solution of polyacrylamide in a mixture of water and maltose syrup (C.P.C., U.K.). The polymer concentration and the ratio of water to syrup must be carefully chosen to ensure that the viscosity is as independent of shear rate as possible. When this process is optimized, the corresponding first normal stress difference ν_1 is reasonably approximated by a quadratic relation of the form

$$\nu_1 = 2\eta_0 \lambda q^2, \tag{3}$$

where η_0 is the viscosity (now assumed constant) and λ is a relaxation time. The product of λ and a typical shear rate is the Weissenberg number W. (Inspection of figure 2 reveals that most of the geometries have an unambiguous fully developed Poiseuille-flow region before a protuberance, slot or obstacle is encountered. The characteristic shear rate used in the Weissenberg number is taken to be $\bar{U}/L$, and the Reynolds number R is $\rho \bar{U} L/\eta_0$, where ρ is the density, $\bar{U}$ is the mean velocity and L is a characteristic length, which is taken as the width of the fully developed Poiseuille-flow channel.)

Characterizing an elastic liquid by means of a constant viscosity η_0 and a relaxation time λ (or, equivalently, characterizing a flow by using a Reynolds number R and Weissenberg

number W) is an idealization, but a useful one as we attempt to compare flow characteristics for elastic and Newtonian liquids. (The Weissenberg number is of course zero for a Newtonian liquid.)

The rheometric behaviour of the Boger liquids is obtained from a Weissenberg Rheogoniometer R16 model which provides (η, q) and (ν_1, q) data (see figure 4). Liquids B1 and B3 clearly have the desired properties of a Boger liquid but marked shear-thinning behaviour is evident in liquid B2. We have nevertheless characterized all *three* liquids in terms of a density ρ, a viscosity η_0 and a relaxation time λ, the relevant values being estimated to be as in table 1.

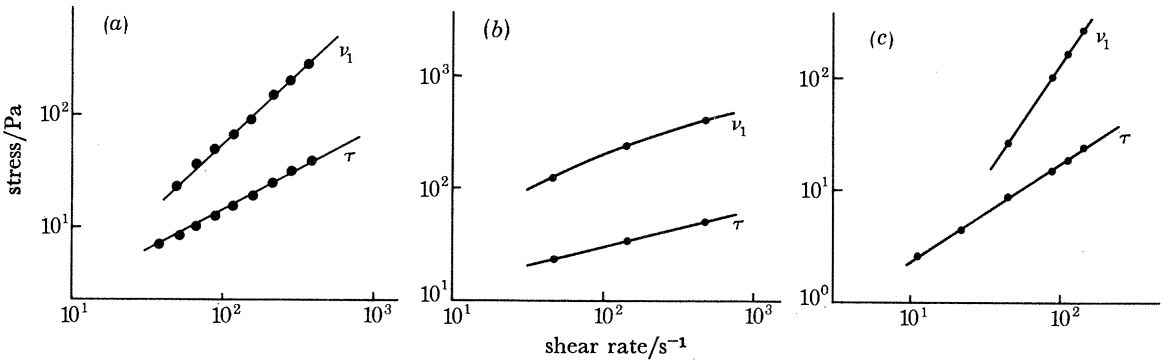

FIGURE 4. Rheometric data for the test liquids used: (*a*) liquid B1, (*b*) liquid B2, (*c*) liquid B3.

TABLE 1. ESTIMATED DENSITY, VISCOSITY AND RELAXATION TIME FOR LIQUIDS B1–B3

liquid	ρ/(g cm^{-3})	η_0/(Pa s)	λ/s
B1	1.3	0.126	0.03
B2	1.3	0.3	0.03
B3	1.35	0.18	0.034

(*c*) *Flow visualization*

In a small number of the flow visualization photographs, some of the streamlines are seen to end abruptly at solid boundaries, which is impossible if the flow is truly two-dimensional. In figures 5*d* and 6*b*, *d* (plates 1 and 2), this is essentially an illusion caused by the positioning of the camera, but, in figures 10*b*, *d* (plate 6), it is caused by a *three*-dimensional effect which is present in some of the high Reynolds number situations. That the flow under extreme conditions has a significant three-dimensional component is easily verified by rotating the laser through 90° and observing the flow in the vertical plane. The spiralling flow observed in figure 8 (plate 4) is also a three-dimensional effect.

A suitable and important first example of the flow visualization technique is provided by flow over a two-dimensional hole (figures 2*a*, *b*). It is a situation that has generated a significant literature (see, for example, Walters 1975, p. 75; Hou *et al.* 1977) and it has also led to controversy (Han & Yoo 1980). Some of the points at issue are elucidated by the present study.

Figure 5 contains a comparison of the flow of Newtonian and elastic liquids over a square hole at two relatively low Reynolds numbers. The asymmetry in the recirculating vortex caused by fluid inertia in the Newtonian case is clearly counteracted by fluid elasticity. Indeed, one of the features of flow over a hole is the opposing asymmetries resulting from inertia and elasticity. This is most clearly seen in figure 7 (plate 3) for the deep wide hole.

Another dominant feature is also evident from figures 6 and 7, namely the lower positioning of the vortex in the hole for the elastic liquids accompanied by the lowering and distortion of the separation streamline.

The deep hole allows investigation of the flow below the dominant initial recirculating vortex and, as expected, a very weak secondary vortex is present (figure 8).

We now consider flow past a protuberance (see figure 2*c*). Photographs of the streamlines for a Reynolds number of 5 are given in figure 9 (plate 5). There is no strong vortex behaviour† and the only feature meriting specific comment is the increased curvature of the streamlines for the elastic liquid. Downstream vortices are clearly in evidence at higher values of the Reynolds number (figure 10), and the main effect of elasticity is to decrease the vortex size and change the curvature of the dividing streamline between the mainstream and the vortex flows. There is also a clearly defined movement in the position of the vortex node.

Mixing flow (see figure 2*d*) leads to interesting flow characteristics as the ratio of the flow rates in the two inlet arms is varied (for a fixed mean flow rate in the downstream wide channel). It will be seen from figures 11 and 12 (plates 7 and 8) that, as the flow rate in the bottom arm is reduced, an important recirculating vortex develops which is attached to the lower surface. The presence of the vortex forces the stream in the bottom arm through a narrow gap adjacent to the barrier. The main effect of elasticity is again to change the curvature of the dividing streamline and to alter the position of the vortex with respect to the edge of the barrier. There is also evidence, not discernible from the figures, that the intensity of the vortex is reduced by the presence of elasticity. (The available experimental data in figures 11 and 12 for Newtonian and elastic liquids are at different Reynolds numbers, but the stated conclusions were confirmed by several visual inspections during the experimental programme.)

Separating flow is obtained by reversing the flow in the mixing geometry. Not surprisingly, the main features of the streamlines in separating and mixing flow are similar in general terms and we have simply chosen to show the interesting effect of elasticity on the recirculating vortex (figure 13, plate 9). We note with interest that, in contrast with the situation in mixing flow, the intensity of the vortex is observed to increase with elasticity in separating flow.

In many respects, combined mixing and separating flow (see figure 2*e*) provides the most interesting geometry of the present study. The flow directions and flow rates can be varied in numerous ways and the arrows on the various figures again indicate the direction and relative strength of the streams in the various arms.

Figures 14 and 15 (plates 10 and 11) show the streamlines for fixed flow rates and three values of the gap l. In general, some of the liquid entering the test section proceeds unidirectionally while some is reversed. Not surprisingly, unidirectional flow tends to dominate as l decreases but a reversed flow is still in evidence even with the smallest gap shown. In relative terms, the elastic liquid shows a stronger aversion to reversed flow than the Newtonian liquid, and unidirectional flow is clearly more in evidence in figure 15 than in figure 14. Another interesting contrast is the striking symmetry in figure 14 which is largely absent in figure 15. There is no doubt that the availability of a very refined mechanism for controlling the flow rates in the respective arms would also lead to symmetry for the elastic liquid in what is after all a symmetrical situation, but, other things being equal, we have found symmetry to be an elusive feature in the flow of highly elastic liquids.

† At very low Reynolds numbers, symmetrical streamline patterns arise about the obstruction, reflecting small weak vortex behaviour that changes negligibly with elasticity, both upstream and downstream of the obstruction.

Figure 16*a* (plate 12) is an attempt at obtaining symmetry for an elastic liquid, which is reasonably successful. It shows that conditions can exist for which all the flow is of the reversed kind. Figures 16*b* and 16*c* show how the flow characteristics change with different flow rates in the various arms, figure 16*c* having the form we would have anticipated from our study of mixing and separating flow.

The final geometry considered in the present study involves channel flow that is disturbed by a cylindrical obstacle (see figure 2*f*). The obstacle is in a slightly asymmetric position with respect to the channel. For the Newtonian liquid (figure 17*a*, plate 13) the asymmetry in the streamlines is barely discernible to the naked eye (if at all) whereas the asymmetry is *exaggerated* for the elastic liquid (figures 17*b*, *c*). This is yet another dramatic demonstration of the differences in flow characteristics found in Newtonian and elastic liquids. It supports our conclusion in regard to combined mixing and separating flow that symmetry is elusive for elastic liquids whenever there is a mechanism in the flow for promoting an asymmetry of any degree.

3. Theory

Attempts to simulate theoretically the flow of Newtonian and elastic liquids in complex geometries have had to await the advent of very high speed computers. Developments with respect to Newtonian fluids are now well advanced (see, for example, Kawaguti 1965; Roache 1972; Taylor & Hood 1973; Gallagher *et al.* 1978) but successful studies involving non-Newtonian liquids with high elasticity are of fairly recent origin (see, for example, Walters 1979; Leal 1979; Crochet & Bezy 1979).

To characterize the behaviour of highly elastic liquids flowing in complex geometries requires integral or implicit-differential rheological equations of state and in the latter case this means that the components of the stress tensor have to be treated as dependent variables along with the velocity components and the pressure. The basic problem involved in this complication has now been overcome (see, for example, Perera & Walters 1977), but confidence in numerical predictions for highly elastic liquids is still hampered by a number of factors, including

(i) the choice of the most appropriate rheological equation of state;

(ii) the correct strategy of handling re-entrant corners in the numerical simulation;

(iii) the extension of numerical algorithms to realistic values of the Weissenberg number where interesting changes in flow characteristics are observed in the corresponding experimental studies.

The first problem concerning rheological equations is not a serious one and, given that the best one can hope for currently is the qualitative (or at best semi-quantitative) prediction of observed behaviour, any one of a number of differential equations of the Oldroyd/Maxwell type or their integral equivalents (Court *et al.* 1981) can be chosen without invoking criticism. Certainly, for the Boger fluid, the so-called upper convected Maxwell model would be acceptable. This has equations of state given by

$$p_{ik} = -p\delta_{ik} + p'_{ik}, \tag{4}$$

$$p'^{ik} + \lambda_1 \, \mathfrak{d}p'^{ik}/\mathfrak{d}t = 2\eta_0 \, e^{(1)ik}, \tag{5}$$

where δ_{ik} is the Kronecker delta, p an isotropic pressure, $e^{(1)ik}$ is the (first) rate-of-strian tensor and $\mathfrak{d}/\mathfrak{d}t$ is the convected time derivative introduced by Oldroyd (1950); η_0 is a constant

viscosity coefficient and λ_1 is a relaxation time. For the simple shear flow given by (1), the corresponding stress distribution for the upper convected Maxwell model is given by

$$p^{12} = q\eta_0, \quad p^{11}-p^{22} = 2\eta_0\lambda_1 q^2, \quad p^{22}-p^{33} = 0. \tag{6}$$

It is clear that (6) is an acceptable representation of the rheometric behaviour of the Boger fluid discussed in §1. A variable viscosity behaviour can be introduced into the model in various ways. We find it appropriate to take

$$p'^{ik}+\lambda_1\frac{\delta}{\delta t}p'^{ik}+\mu_0 p'^j e^{(1)ik} = 2\eta_0\left(1+\lambda_2\frac{\delta}{\delta t}\right)e^{(1)ik}, \tag{7}$$

where μ_0 and λ_2 are positive constants with $\lambda_2 \leqslant \lambda_1$, in which case the viscosity in a simple shear flow is given by

$$\eta(q) = \eta_0[1+\mu_0\lambda_2 q^2]/[1+\mu_0\lambda_1 q^2]. \tag{8}$$

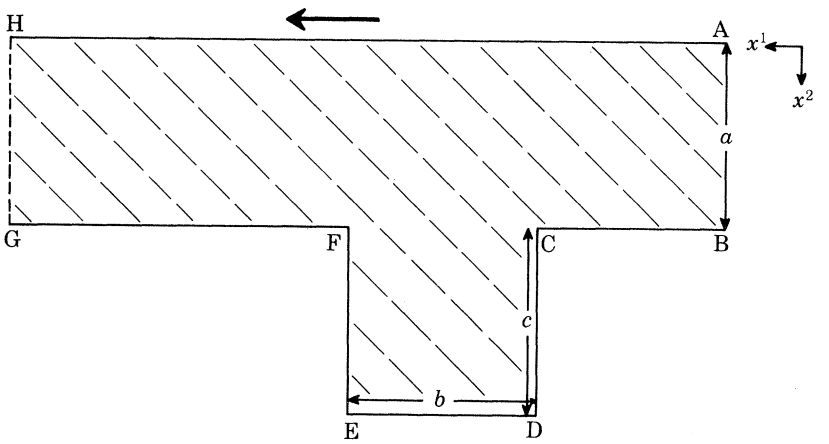

FIGURE 18. The square-hole geometry.

A more serious obstacle in the process of obtaining reliable numerical predictions concerns the correct strategy for handling re-entrant corners. The problem is far more acute for elastic models than it is for Newtonian liquids and really requires a detailed asymptotic-expansion analysis near the corner for its resolution (Holstein 1980). This is a non-trivial problem with no guarantee of ultimate success. To make headway, we have therefore used the most acceptable *simple* corner strategy available, namely an extension of that due to Kawaguti (1965). Its application to elastico–viscous flow problems is discussed by Perera & Walters (1977) and Davies *et al.* (1979).

In all existing simulation studies for highly elastic liquids there is an effective upper bound on the Weissenberg number above which the numerical scheme will not converge.† This is the case in the present study and we have not always been able to reach the Weissenberg levels we would have wished. At the same time, our simulations are sufficient to point to significant success in predicting the observed behaviour described in §2(*c*).

† It is well known that numerical algorithms for models with a variable viscosity behaviour can reach higher values of the Weissenberg number than corresponding algorithms for models with a constant viscosity. For this reason, we have occasionally been forced to work with model (7) rather than the simpler model (5).

Our overall numerical strategy follows closely that described by Davies *et al.* (1979). It is a square-mesh finite-difference representation which involves the decoupling of the nonlinear system of governing equations and the solving of the resulting linear systems by an S.O.R. iterative technique. Available computer store and time allowed approximately 2500 grid points in the flow geometry.

We shall outline the numerical procedure for the square-hole geometry (figures 2*a* and 18) which contains all the essential features of the present work.

We introduce non-dimensional variables through the substitutions†

$$\left.\begin{aligned} x^{1*} &= \frac{x^1}{L}, \quad x^{2*} = \frac{x^2}{L}, \quad v^{1*} = \frac{v^1}{\overline{U}}, \quad v^{2*} = \frac{v^2}{\overline{U}}, \\ p'^{ik*} &= p'^{ik}\frac{L}{\eta_0 \overline{U}}, \quad R = \frac{\rho \overline{U} L}{\eta_0}, \quad W = \frac{\lambda_1 \overline{U}}{L}, \end{aligned}\right\} \tag{9}$$

where L is a characteristic length (the width of the channel HG) and $\overline{U}$ is a characteristic velocity (the mean velocity across HG). The governing equations for a two-dimensional flow of model (5) are then

$$\omega = -\left(\frac{\partial^2\phi}{\partial(x^1)^2}+\frac{\partial^2\phi}{\partial(x^2)^2}\right), \tag{10}$$

$$R\left(\frac{\partial\phi}{\partial x^1}\frac{\partial\omega}{\partial x^2}-\frac{\partial\phi}{\partial x^2}\frac{\partial\omega}{\partial x^1}\right) = \frac{\partial^2 p'^{11}}{\partial x^1 \partial x^2}+\frac{\partial^2 p'^{12}}{\partial(x^2)^2}-\frac{\partial^2 p'^{12}}{\partial(x^1)^2}-\frac{\partial^2 p'^{22}}{\partial x^1 \partial x^2}, \tag{11}$$

$$p'^{11}\left(1-2W\frac{\partial v^1}{\partial x^1}\right)+W\left(v^1\frac{\partial p'^{11}}{\partial x^1}+v^2\frac{\partial p'^{11}}{\partial x^2}\right)-2Wp'^{12}\frac{\partial v^1}{\partial x^2} = 2\frac{\partial v^1}{\partial x^1}, \tag{12}$$

$$p'^{22}\left(1-2W\frac{\partial v^2}{\partial x^2}\right)+W\left(v^1\frac{\partial p'^{22}}{\partial x^1}+v^2\frac{\partial p'^{22}}{\partial x^2}\right)-2Wp'^{12}\frac{\partial v^2}{\partial x^1} = 2\frac{\partial v^2}{\partial x^2}, \tag{13}$$

$$-Wp'^{11}\frac{\partial v^2}{\partial x^1}-Wp'^{22}\frac{\partial v^1}{\partial x^2}+W\left(v^1\frac{\partial p'^{12}}{\partial x^1}+v^2\frac{\partial p'^{12}}{\partial x^2}\right)+p'^{12} = \left(\frac{\partial v^1}{\partial x^2}+\frac{\partial v^2}{\partial x^1}\right) \tag{14}$$

with $v^1 = \partial\phi/\partial x^2$, $v^2 = -\partial\phi/\partial x^1$, where ω and ϕ are the non-dimensional vorticity and stream function respectively, and we have dropped the star notation for convenience of presentation. Equations (10)—(14) are five equations in the five unknowns p'^{11}, p'^{22}, p'^{12}, ω and ϕ.

The boundary conditions on ϕ on the solid boundaries AH and BCDEFG are obtained from the no-slip condition $v^1 = v^2 = 0$. Those on HG and AB (boundaries which are assumed to be far enough away from the hole for the flow across them to be unaffected by the presence of the hole) are obtained from the known fully developed Poiseuille-flow prevailing over these boundaries. The related boundary conditions on the other dependent variables can be obtained by techniques that are now well documented (see, for example, Davies *et al.* 1979).

By using a method of inner and outer iterations, the rheological equations of state and the stress equations of motion are solved as three decoupled systems of equations in the stress components, ω and ϕ. At the same time, and in contrast to the work of Davies *et al.* (1979), a successful strategy is found to be to consider, within each inner stress iteration, the rheological equations as linearly coupled differential equations in p'^{11}, p'^{22} and p'^{12}.

Although the numerical scheme necessarily supplies values of the five variables p'^{11}, p'^{22}, p'^{12},

† For model (7), W is given by $W = (\lambda_1-\lambda_2)\,\overline{U}/L$, and the time constants λ_2 and μ_0 are non-dimensionalized by multiplying by $\overline{U}/L$.

ω and ϕ at each grid point, our interest in the present paper is restricted to the stream function ϕ which determines the flow field representation. Acceptable relative tolerance specifications for iterative convergence in the variables [ϕ, stress, ω] are also modified to [10^{-4}, 10^{-2}, 10^{-1}]. This choice is felt to be consistent with the discretized errors of the formulae used to approximate the governing equations. Furthermore, provided a local grid Reynolds number condition is satisfied which will guarantee a diagonally dominant vorticity matrix of equations, all vorticity derivatives are centrally differenced. Under-relaxation of the vorticity equation, and in some instances the stress equations (with a relaxation parameter of about 0.2) is often found to be a useful ploy in rendering convergent solutions when Gauss–Seidel iteration fails. Such points of numerical detail are fully discussed by Webster (1979) and Davies & Webster (1981).

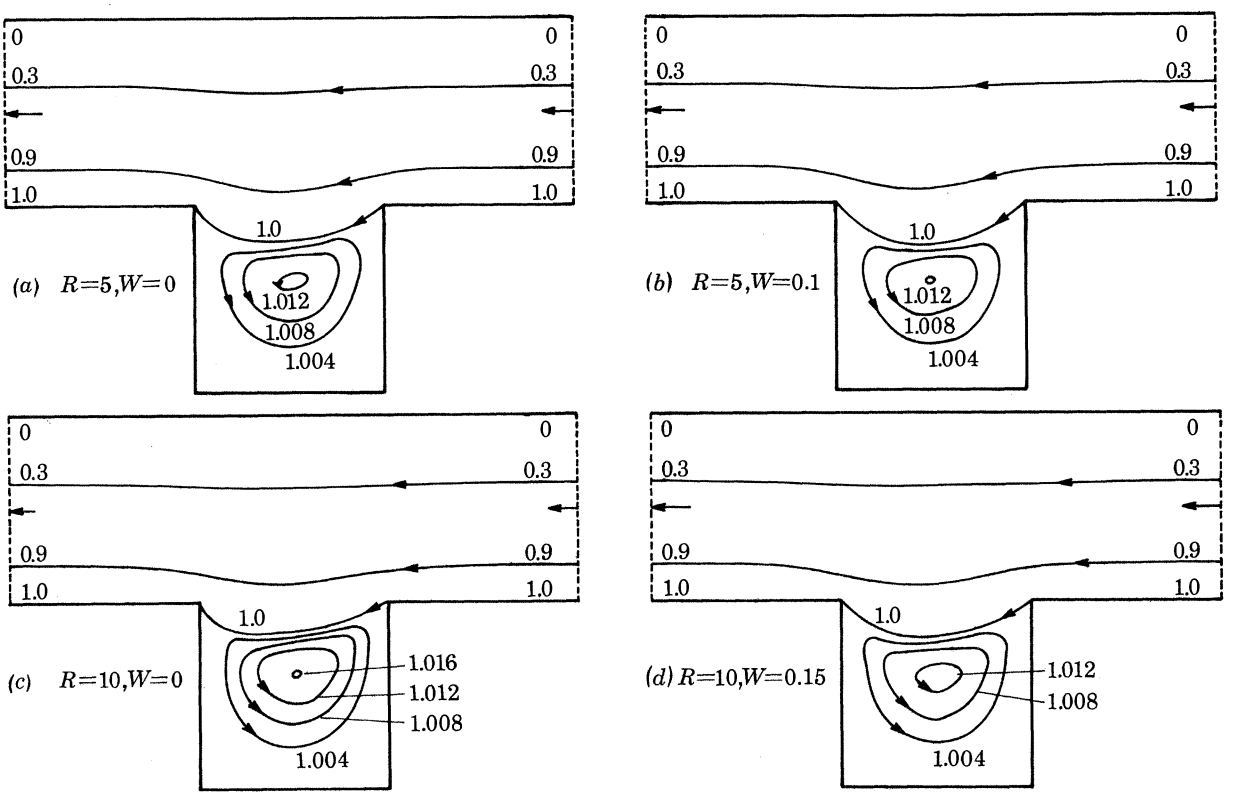

FIGURE 19. Numerical simulation for flow over a square hole.

Representative numerical predictions for the square-hole geometry are given in figure 19, the square grid used in the computation allowing 20 mesh lengths across AB. The numbers in this and subsequent figures correspond to ϕ-values. Figure 19 may be compared with the experimental data shown in figures 5 and 6. The initial symmetry which is known to be present when $R = W = 0$ is destroyed by the opposing influences of inertia and elasticity and there is a tendency for the vortex in elastic liquids to retreat deeper into the hole, although the numerical predictions in this respect are not as dramatic as the experimental results shown in figures 5 and 6. At the same time, the predictions for $W = 0$ are in excellent agreement with experiment. We were not able to obtain converged numerical solutions for values of W higher than 0.15 for $R = 10$.

The opposing influences of inertia and elasticity in determining flow characteristics and the lower positioning of the vortex in the hole as the elasticity is increased are even more dramatically demonstrated by the numerical simulations for the deep-hole geometry, for which 10 mesh lengths were used across AB (figures 20), which may be compared with the experimental results shown in figure 7. We were not able to obtain a converged numerical solution for $W = 0.75$ and even for $W = 0.38$, it was necessary to use model (7) rather than model (5).

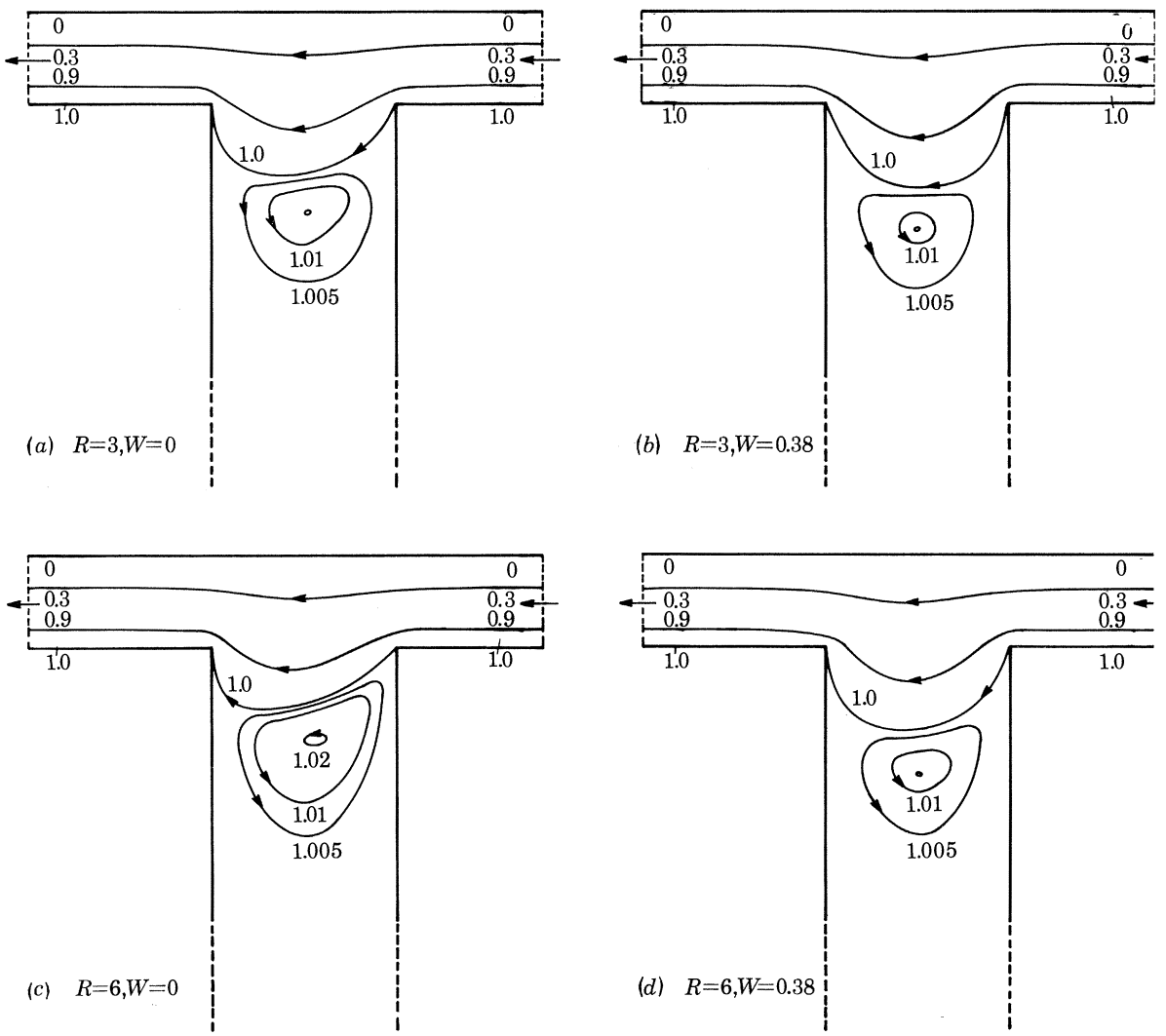

FIGURE 20. Numerical simulation for flow over a deep hole, model (7) being used in (*b*) and (*d*). Non-dimensional values of λ_1, λ_2 and μ_0 are $\lambda_1 = 0.45$, $\lambda_2 = 0.075$, $\mu_0 = 0.0007$.

Figure 21 contains Newtonian simulations for the deep-hole geometry which demonstrate the existence of a very weak secondary vortex of the sort indicated by the long-time-exposure experimental results shown in figure 8. Indeed, the predicted flow for $R = 20$ is in remarkably good agreement with the experimental results.

We have found the protuberance geometry to be the most difficult to handle in the numerical simulation program and it has been necessary to use model (7) to achieve even the modest values of W indicated in figures 22 and 23. For this geometry, the grid used allowed 15 mesh lengths over the wide-channel width.

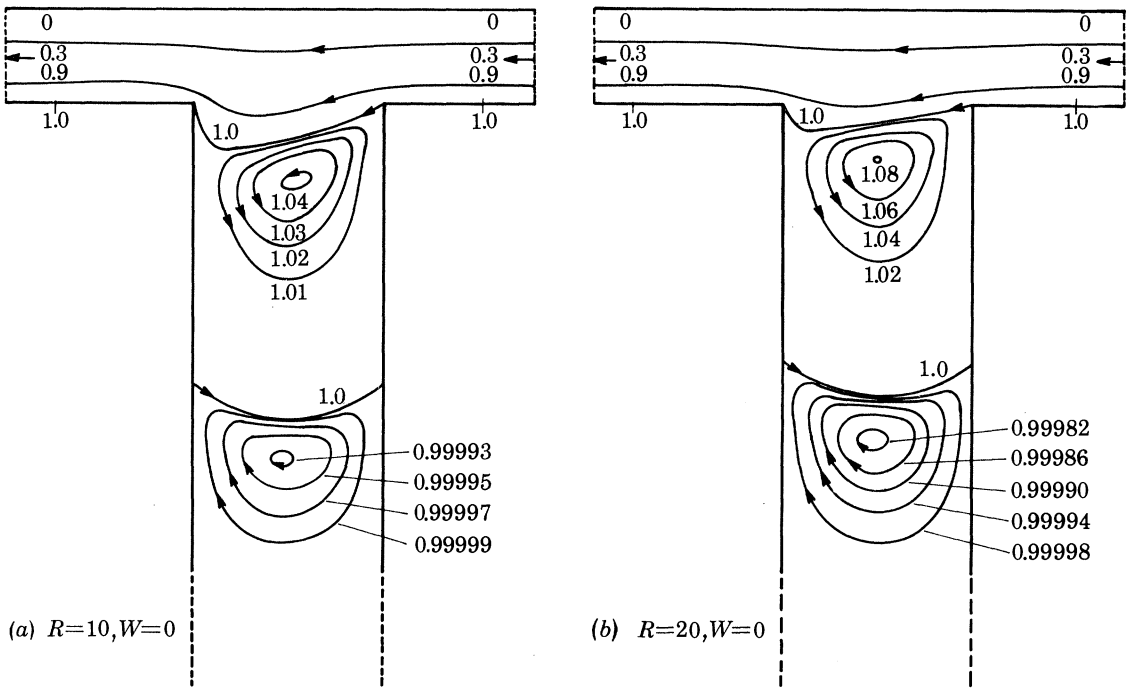

FIGURE 21. Numerical simulation for flow over a deep hole.

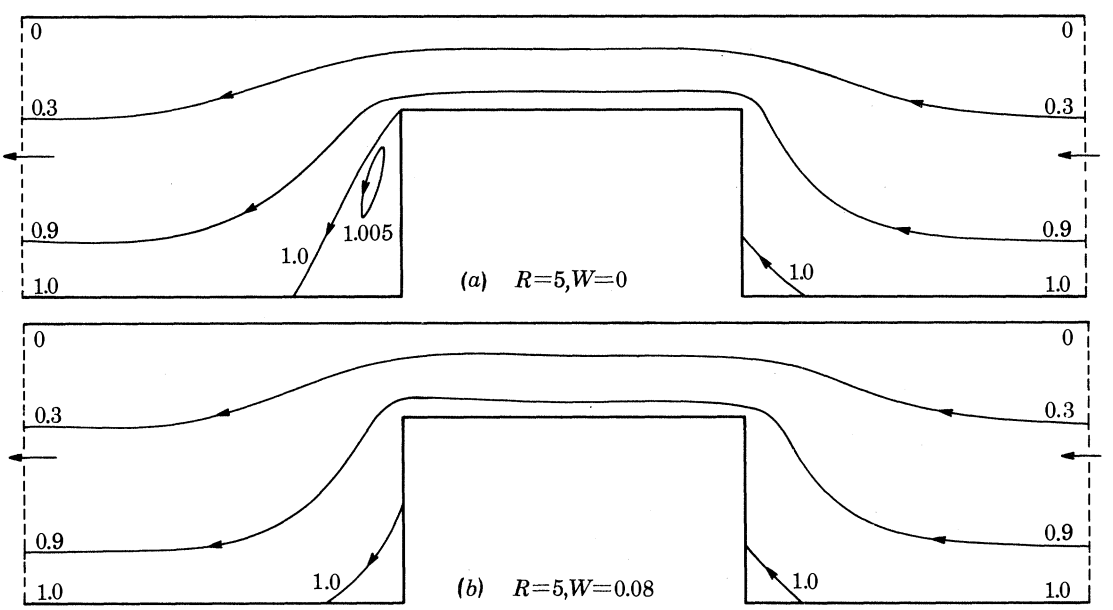

FIGURE 22. Numerical simulation for flow over a protuberance, model (7) being used in (*b*); $\lambda_1 = 0.09$, $\lambda_2 = 0.015$, $\mu_0 = 0.003$.

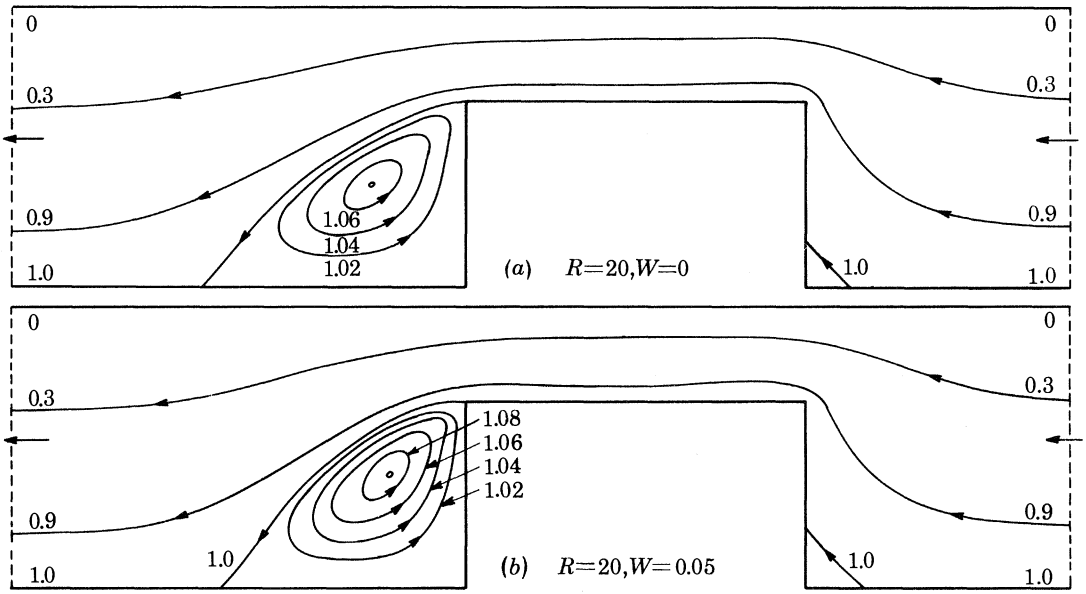

FIGURE 23. Numerical simulation for flow over a protuberance, model (7) being used in (*b*); $\lambda_1 = 0.06$, $\lambda_2 = 0.01$, $\mu_0 = 0.005$.

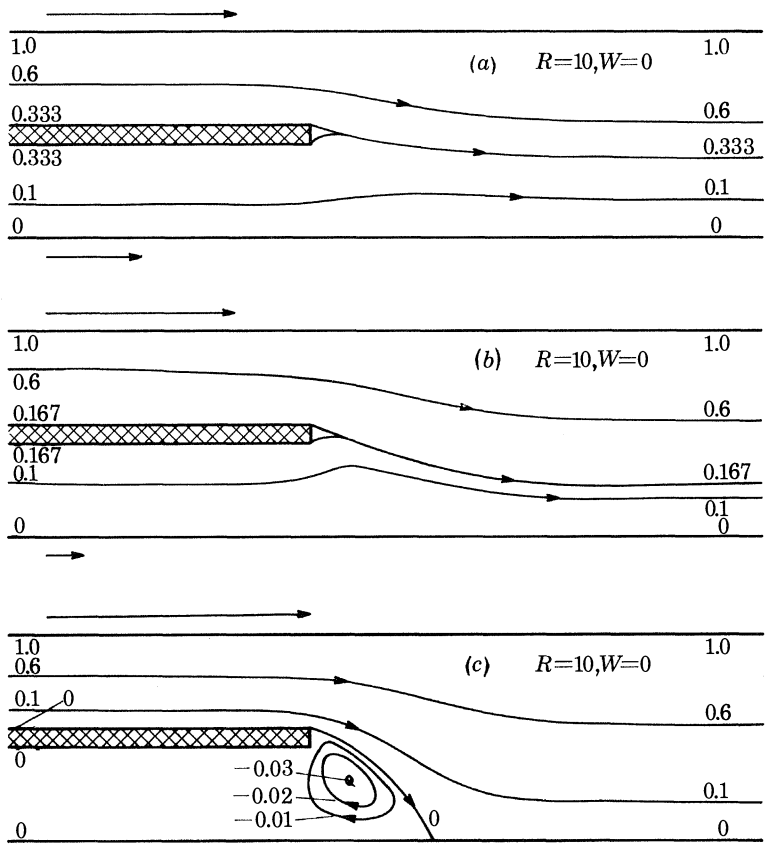

FIGURE 24. Numerical simulation for mixing flow. Ratio of flow rates is (*a*) 2:1, (*b*) 5:1, (*c*) no flow rate in bottom arm.

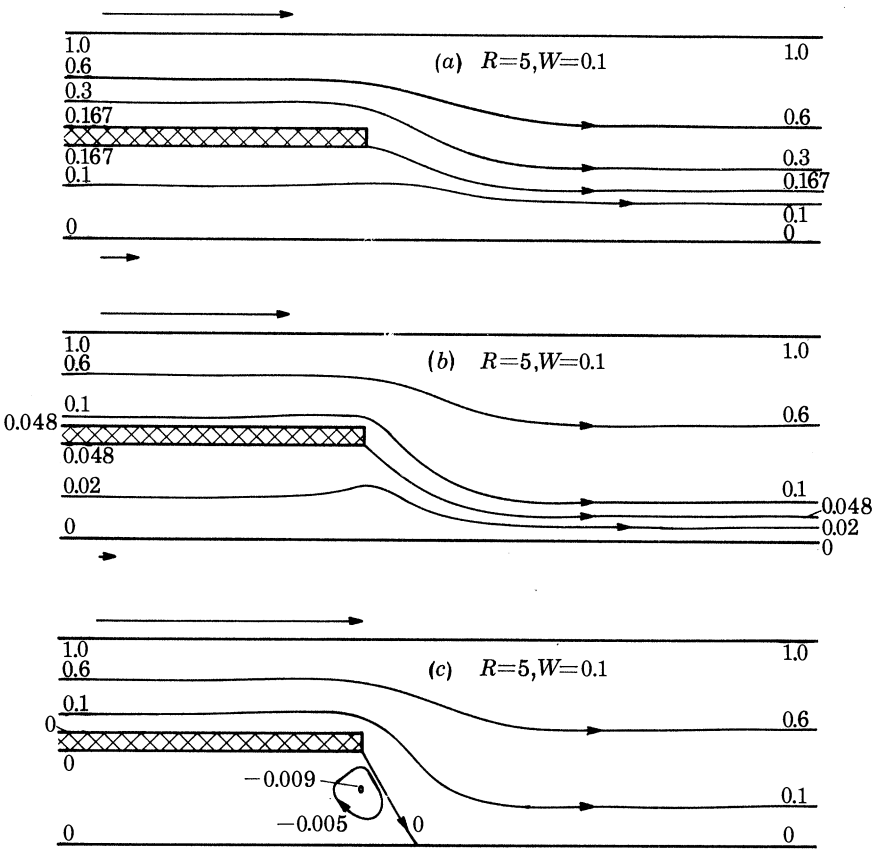

FIGURE 25. Numerical simulation for mixing flow. Ratio of flow rates is (*a*) 5:1, (*b*) 20:1, (*c*) no flow rate in bottom arm.

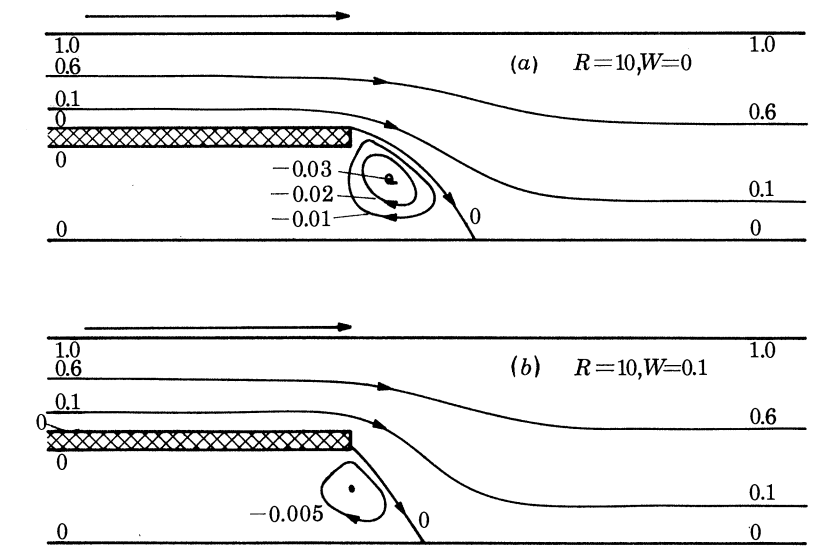

FIGURE 26. Numerical simulation for mixing flow; no flow rate in bottom arm.

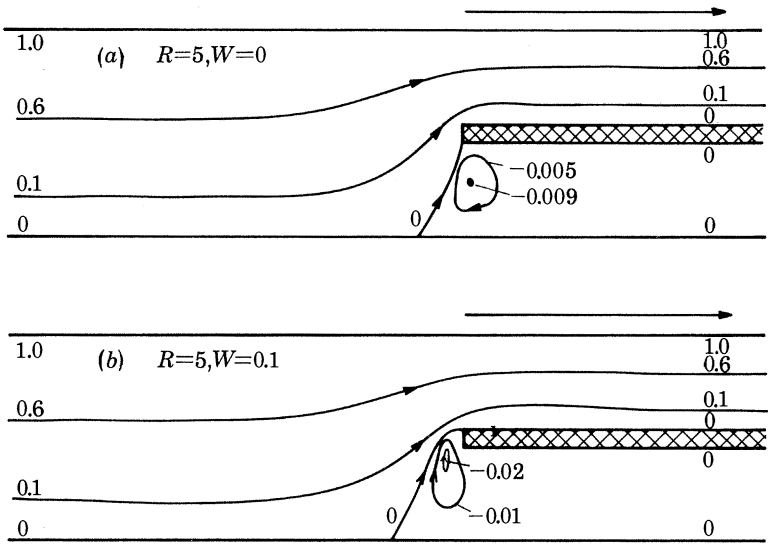

FIGURE 27. Numerical simulation for separating flow; no flow rate in bottom arm.

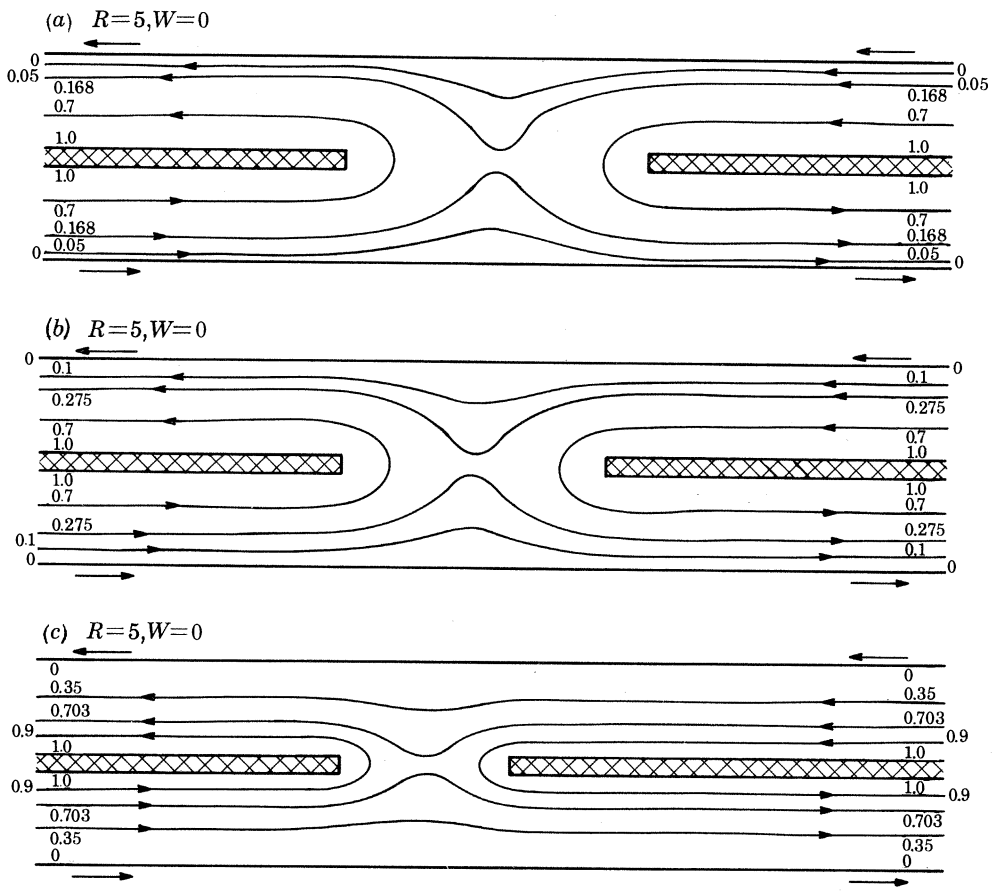

FIGURE 28. Numerical simulation for combined mixing and separating flow; equal flow rates in all arms.

The Newtonian simulations for $R = 5$ and $R = 20$ are both in reasonable agreement with the experimental results given in figures 9 and 10, and the trend of a decreasing size of downstream vortex with increasing elasticity is also apparent. In other respects, the simulations are hampered by the very small values of W attainable for this geometry.

Flow in the mixing geometry (figure 2*d*) has been amenable to numerical simulation, and the relevant predictions are given in figures 24–26. These may be compared with the experimental data of figures 11 and 12. The available grid allowed eleven mesh spaces across the wide channel; the barrier occupied one space, so that each of the narrow channels had a thickness of five mesh spaces. (This also applies to separating flow and combined mixing and separating flow discussed below.) $W = 0.1$ represents the upper limit of Weissenberg number (with the use of model (5)) for this geometry.

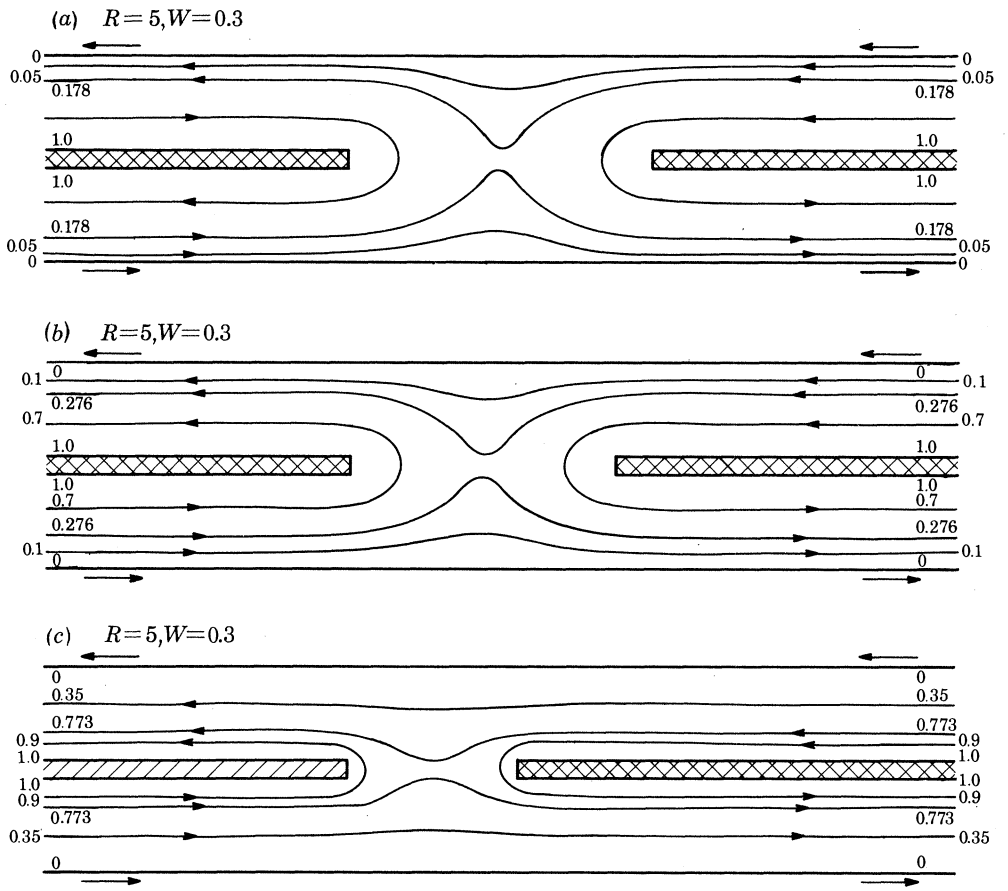

FIGURE 29. Numerical simulation for combined mixing and separating flow; equal flow rates in all arms.

The main conclusions to be drawn from the simulation of mixing flow may be summarized as follows. First, a recirculating vortex appears when the ratio of the flow rates in the two arms is approximately 20:1. This is in excellent agreement with the experimental observations.

Secondly, elasticity reduces the strength of the recirculating vortex and alters its position in general agreement with the experimental results.

Excellent simulation is also obtained for the associated separating flow, for which the flow directions in the mixing geometry are reversed. Figure 27 shows that elasticity increases the

strength of the vortex in this case and has the opposite effect on the movement of the vortex to that predicted and observed for mixing flow. This is in excellent agreement with the experimental observations (cf. figure 13).

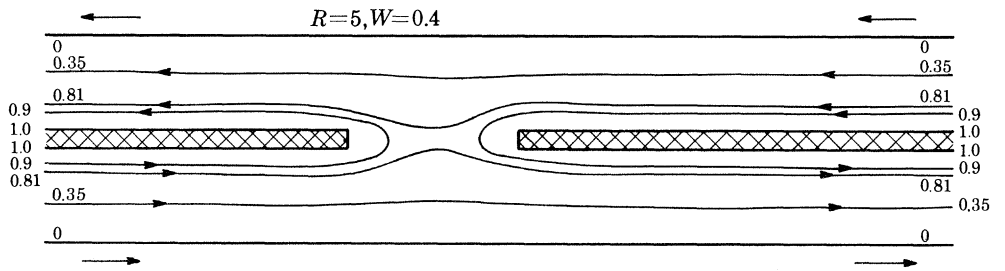

FIGURE 30. Numerical simulation for combined mixing and separating flow; equal flow rates in all arms.

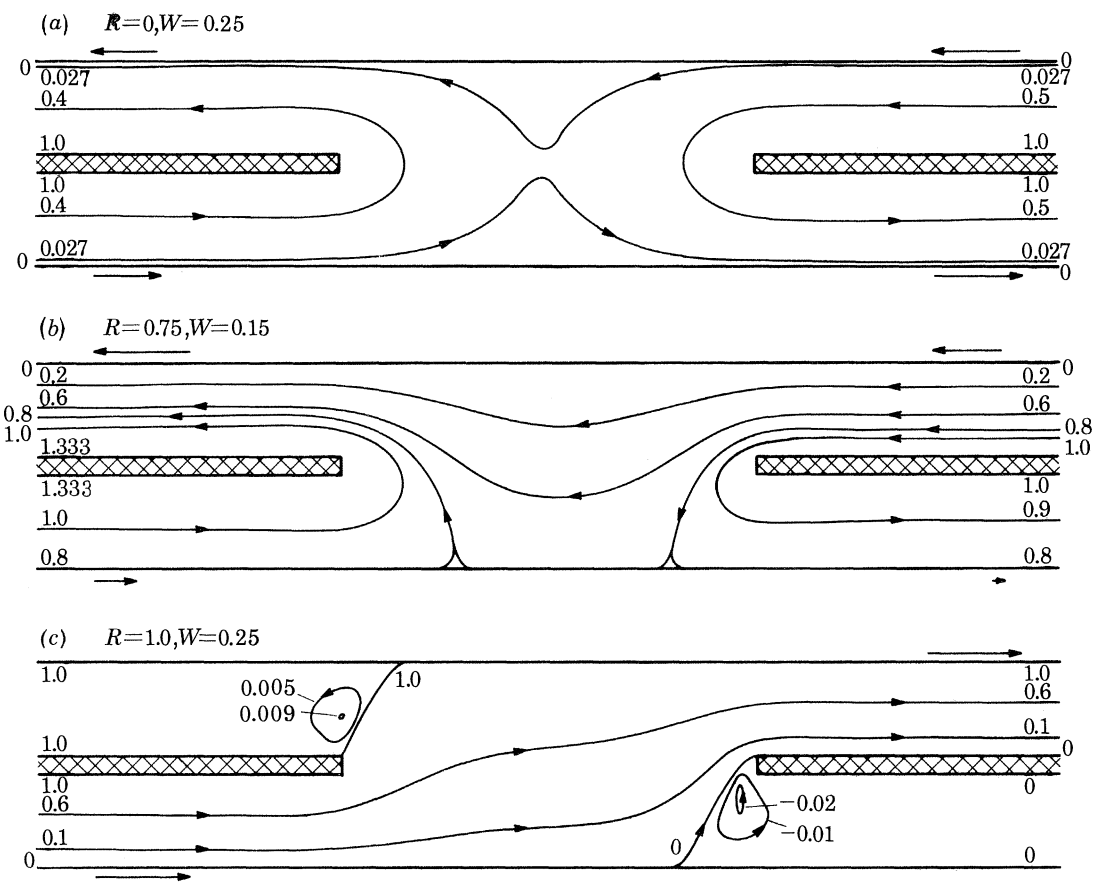

FIGURE 31. Numerical simulation for combined mixing and separating flow with relative flow rate in each arm indicated by length of arrows.

Combined mixing and separating flow provides a further demonstration of the power of the present numerical simulation technique. Figures 28–30 contain the relevant predictions when the flow rate in each arm is the same. These may be compared with the experimental results given in figures 14 and 15. Except for the narrow gap case, $W = 0.3$ represents the maximum value of the Weissenberg number attainable. We see that unidirectional flow tends to dominate

as the gap width l decreases, as one would expect, although a reversed flow still exists even with the smallest gap. Interestingly, the elastic liquid shows more inclination to follow unidirectional flow, in satisfying agreement with the conclusions reached in §2.

In the $R = 5$, $W = 0.4$ simulation for the narrow gap there is the suggestion of the type of asymmetry shown in figure 15*c*.

We have attempted to simulate the complex flows described in figure 16 and have been able to attain the relevant Weissenberg numbers involved. Figure 31 contains the predictions for essentially the same flow conditions as those pertaining in the experiments. A comparison of figure 16 with figure 31 indicates dramatically good agreement in all cases with even the finer details of the flow described.

Finally, for completeness, we remark that simulating the asymmetric flow past a circular cylinder described experimentally in figure 17 is outside the scope of the present work.

4. Conclusion

Numerical simulation in Newtonian and non-Newtonian flow has now reached the point where quite complex flows can be handled and the effect of fluid elasticity assessed (qualitatively at least). Problems still remain, especially those associated with extending the Weissenberg number range, but at least a comprehensive set of experimental results is now available to facilitate future tests of new numerical techniques.

We have benefited from several discussions with Dr W. M. Jones and Dr A. R. Davies.

During the course of the work described in this paper, T.C. and M.F.W. were employed as postdoctoral research associates on research grants financed by the S.R.C.

References

Boger, D. V. 1977/8 *J. non-Newtonian Fluid Mech.* **3**, 87–91.
Cable, P. J. & Boger, D. V. 1978 *A.I.Ch.E. Jl* **24**, 869–879.
Court, H., Davies, A. R. & Walters, K. 1981 *J. non-Newtonian Fluid Mech.* **8**, 95–117.
Crochet, M. J. & Bezy, M. 1979 *J. non-Newtonian Fluid Mech.* **5**, 201–218.
Davies, A. R., Walters, K. & Webster, M. F. 1979 *J. non-Newtonian Fluid Mech.* **4**, 325–344.
Davies, A. R. & Webster, M. F. 1981 *J. comput. Phys.* (To be published.)
Gallagher, R. H., Zienkiewicz, O. C., Oden, J. T., Morandi Cecchi, M. & Taylor, C. (ed.) 1978 *Finite elements in fluids*, vol. 3. London: John Wiley and Sons.
Han, C. D. & Yoo, H. J. 1980 *J. Rheol.* **24**, 55–79.
Holstein, H. 1981 Ph.D. thesis, University of Wales, Aberystwyth.
Hou, T.-H., Tong, P. P. & De Vargas, L. 1977 *Rheol. Acta* **16**, 544–547.
Kawaguti, M. 1965 *Mathematics Research Center Rep.*, no. 574. University of Wisconsin.
Keentok, M., Georgescu, A. G., Sherwood, A. A. & Tanner, R. I. 1980 *J. non-Newtonian Fluid Mech.* **6**, 303–324.
Leal, L. G. 1979 *J. non-Newtonian Fluid Mech.* **5**, 33–78.
Mackley, M. R. 1978 *J. non-Newtonian Fluid Mech.* **4**, 111–136.
Oldroyd, J. G. 1950 *Proc. R. Soc. Lond.* A **200**, 523–541.
Perera, M. G. N. & Walters, K. 1977 *J. non-Newtonian Fluid Mech.* **2**, 49–81.
Petrie, C. J. S. 1979 *Elongational flows*. London: Pitman Press.
Roache, P. J. 1972 *Computational fluid dynamics*. Albuquerque, New Mexico: Hermosa Publications.
Taneda, S. 1979 *J. phys. Soc. Japan* **46**, 1935–1942.
Taylor, C. & Hood, P. 1973 *Comput. Fluids* **1**, 73–100.
Walters, K. 1975 *Rheometry*. London: Chapman and Hall.
Walters, K. 1979 *J. non-Newtonian Fluid Mech.* **5**, 113–124.
Walters, K. (ed.) 1980 *Rheometry: industrial applications*. Chichester: John Wiley and Sons.
Webster, M. F. 1979 Ph.D. thesis, University of Wales, Aberystwyth.

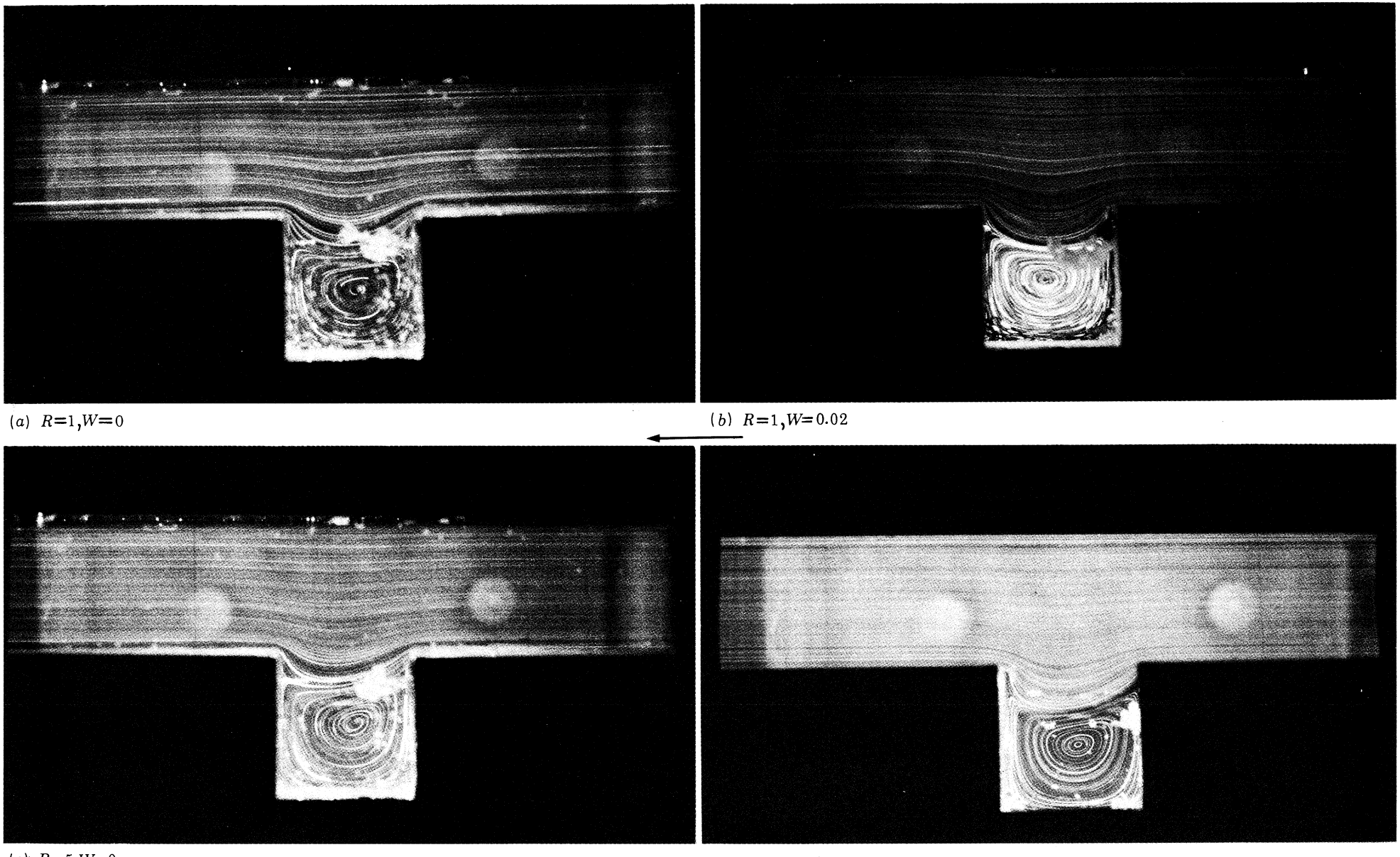

(a) $R=1, W=0$

(b) $R=1, W=0.02$

(c) $R=5, W=0$

(d) $R=5, W=0.1$

FIGURE 5. Flow over a square hole: (*a*) and (*c*) Newtonian, (*b*) and (*d*) liquid B1.

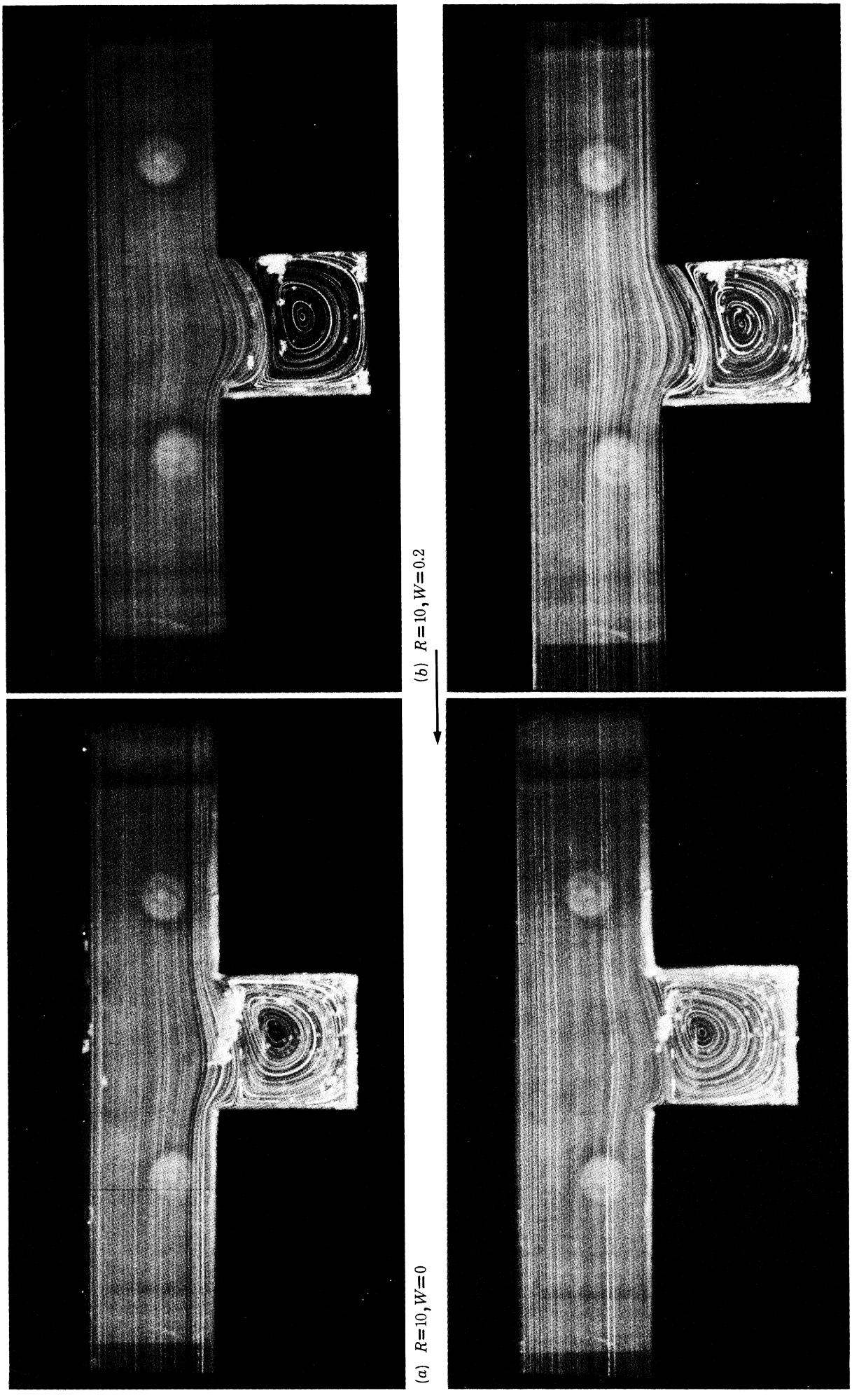

FIGURE 6. Flow over a square hole: (*a*) and (*c*) Newtonian, (*b*) and (*d*) liquid B1.

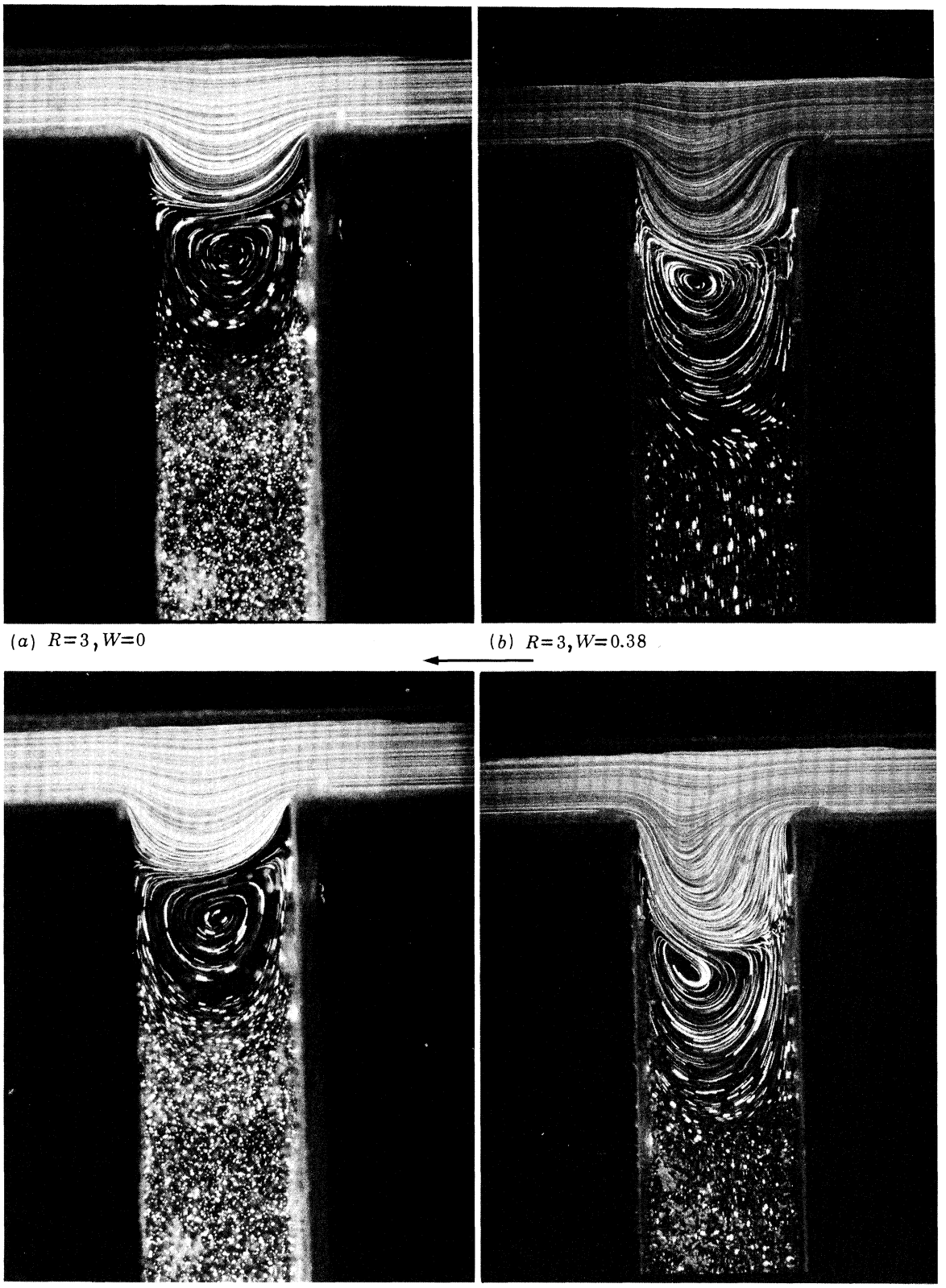

FIGURE 7. Flow over a deep hole: (*a*) and (*c*) Newtonian, (*b*) and (*d*) liquid B3.

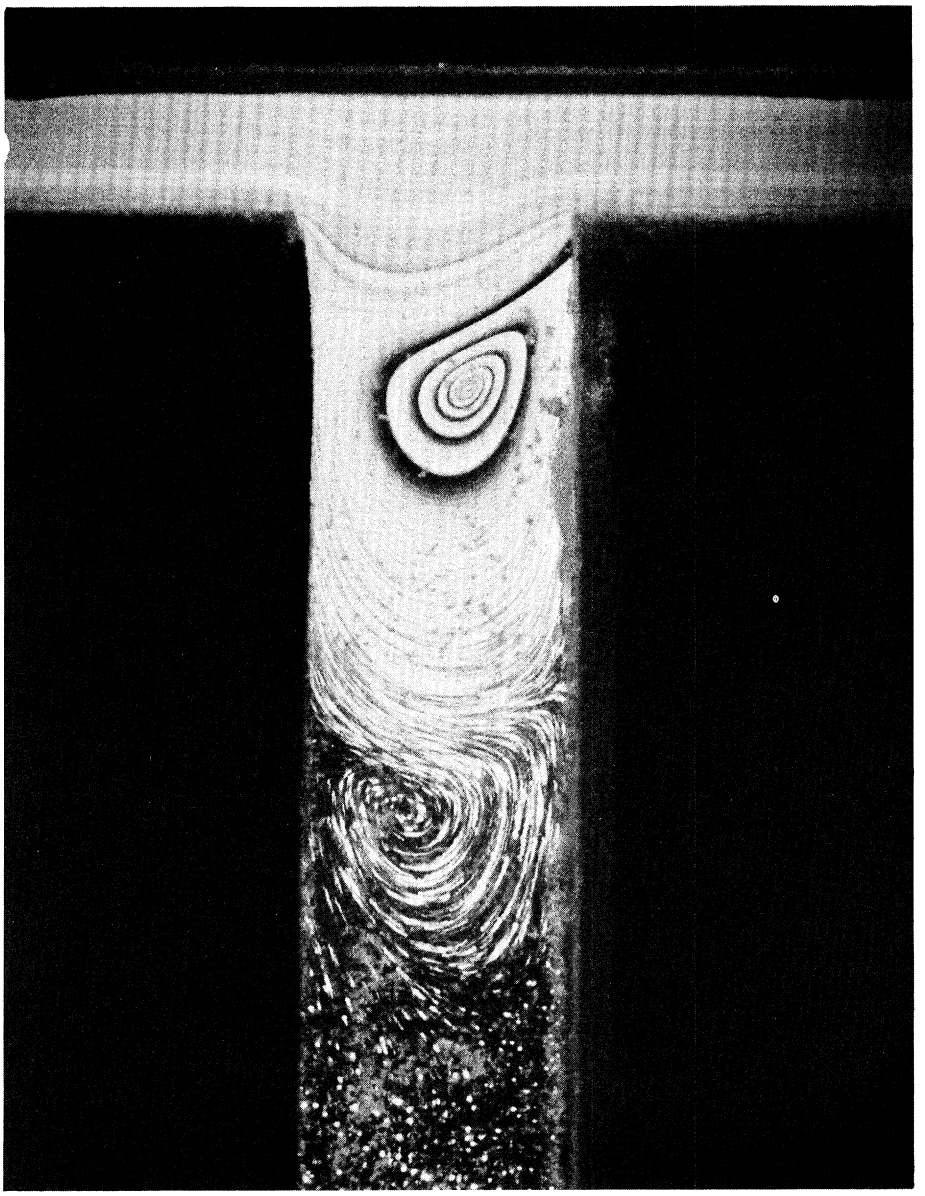

$R=20, W=0$

FIGURE 8. Flow over a deep hole: exposure time, 10 minutes.

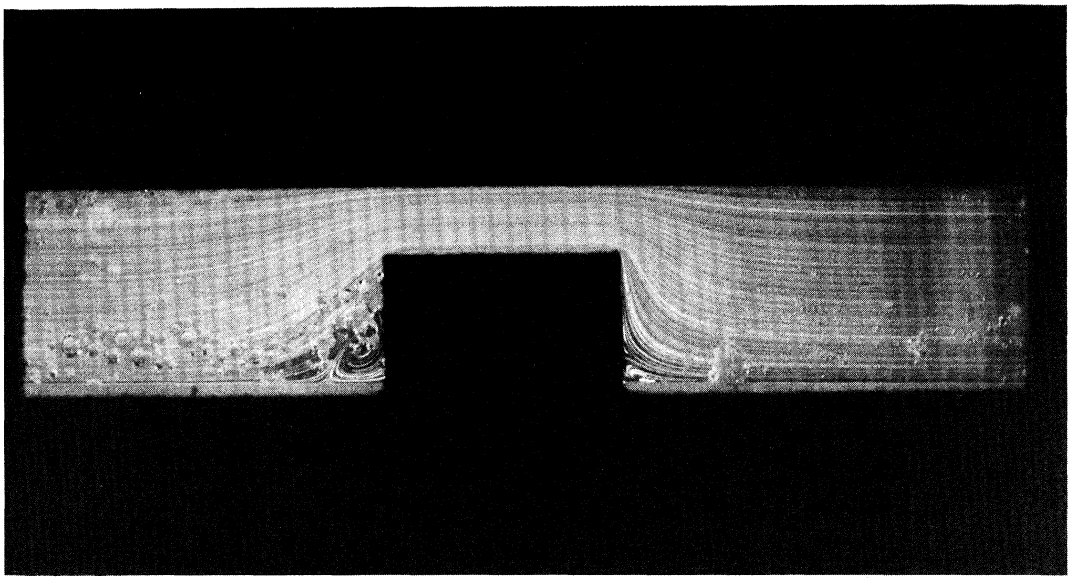

(*a*) $R=5, W=0$

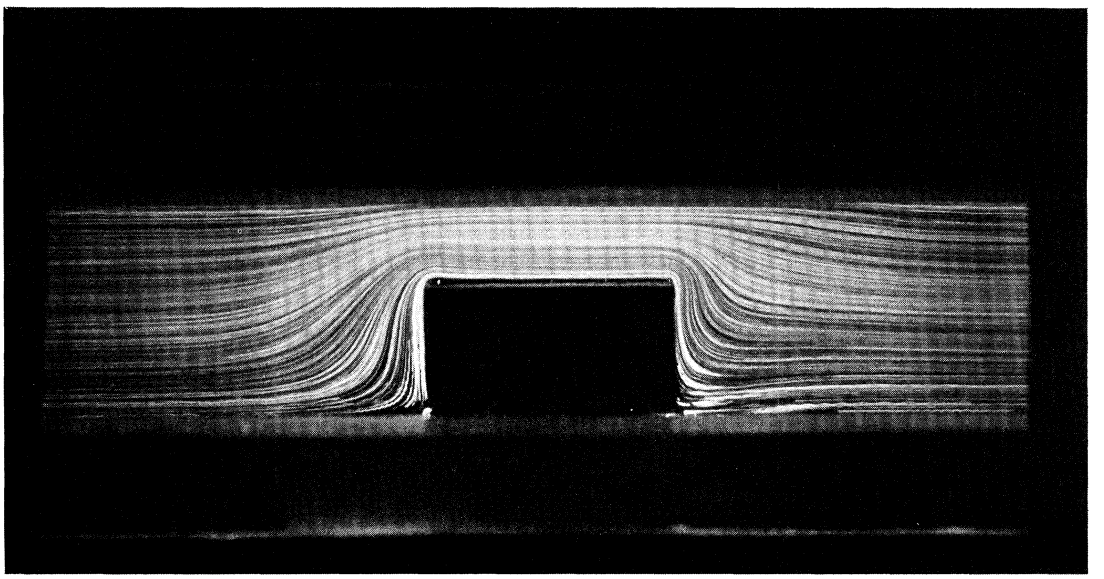

(*b*) $R=5, W=0.1$

FIGURE 9. Flow over a rectangular protuberance: (*a*) Newtonian, (*b*) liquid B1.

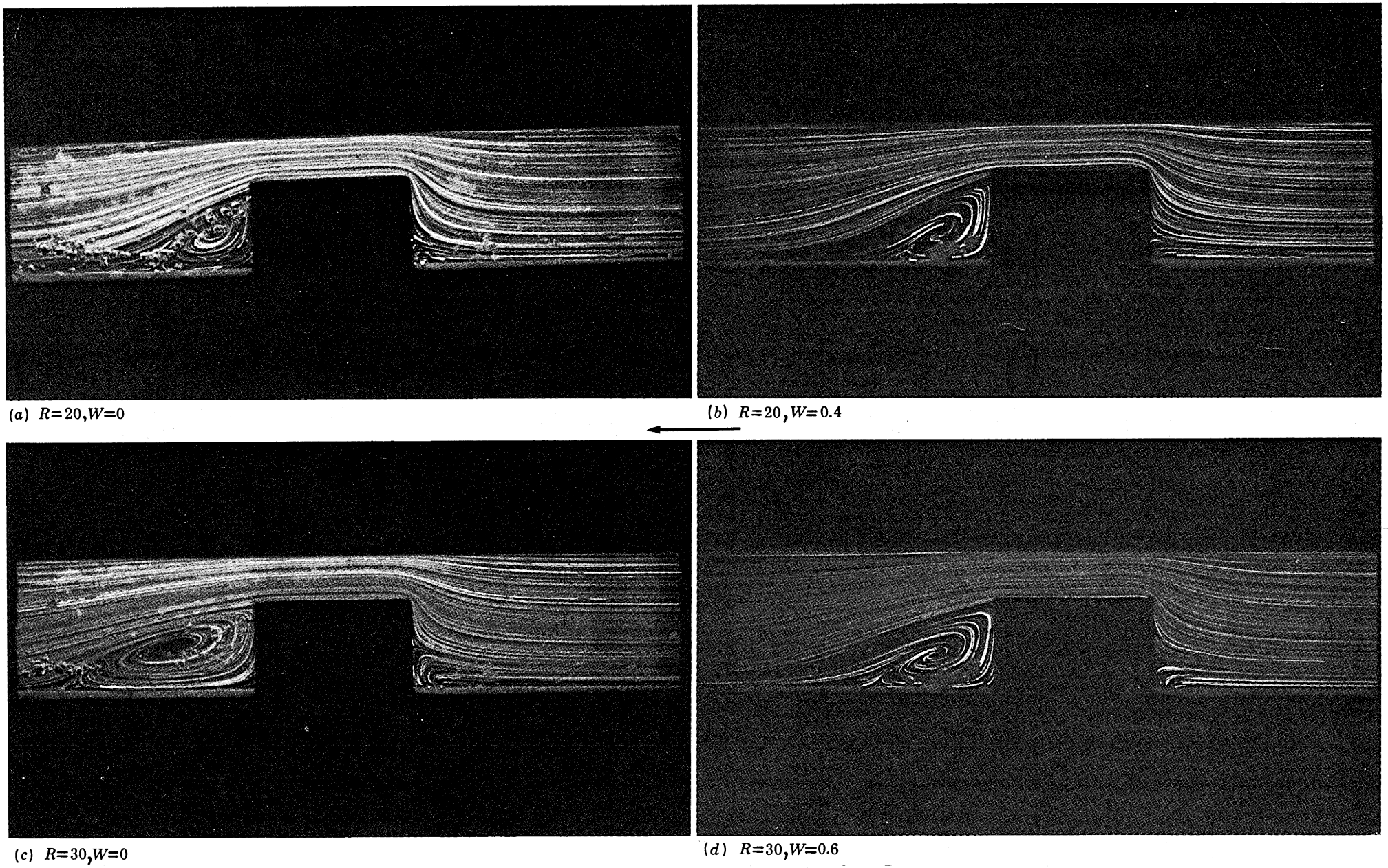

(a) $R=20, W=0$

(b) $R=20, W=0.4$

(c) $R=30, W=0$

(d) $R=30, W=0.6$

FIGURE 10. Flow over a rectangular protuberance: (*a*) and (*c*) Newtonian, (*b*) and (*d*) liquid B1.

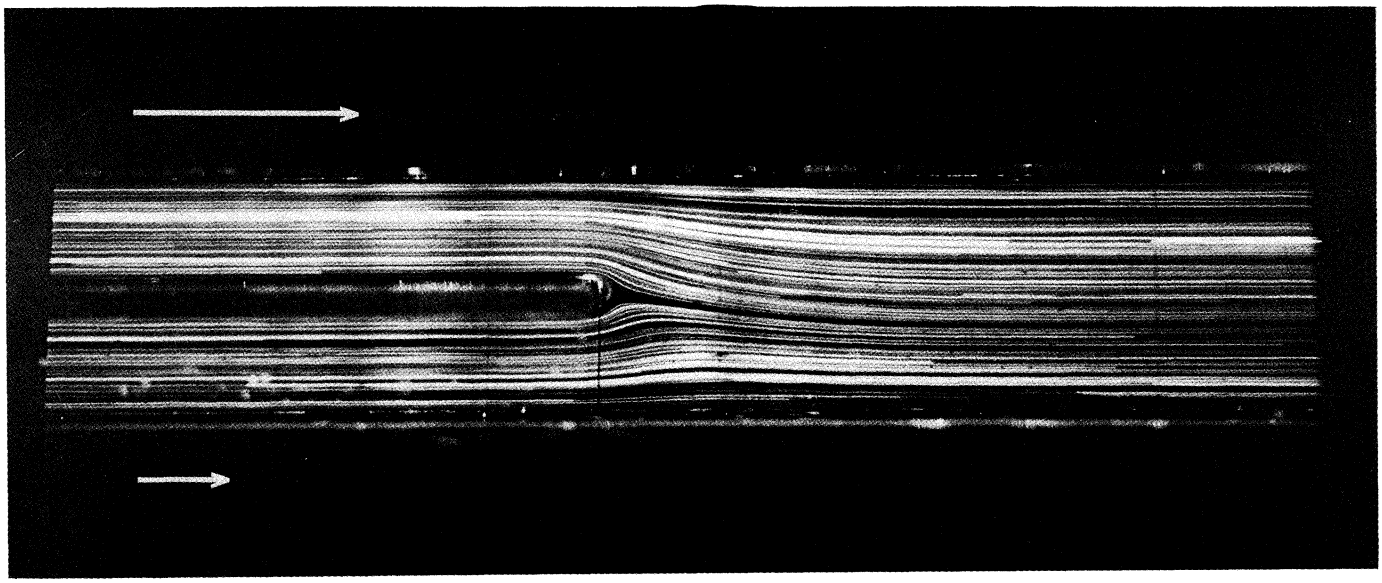

(*a*) $R=10, W=0$

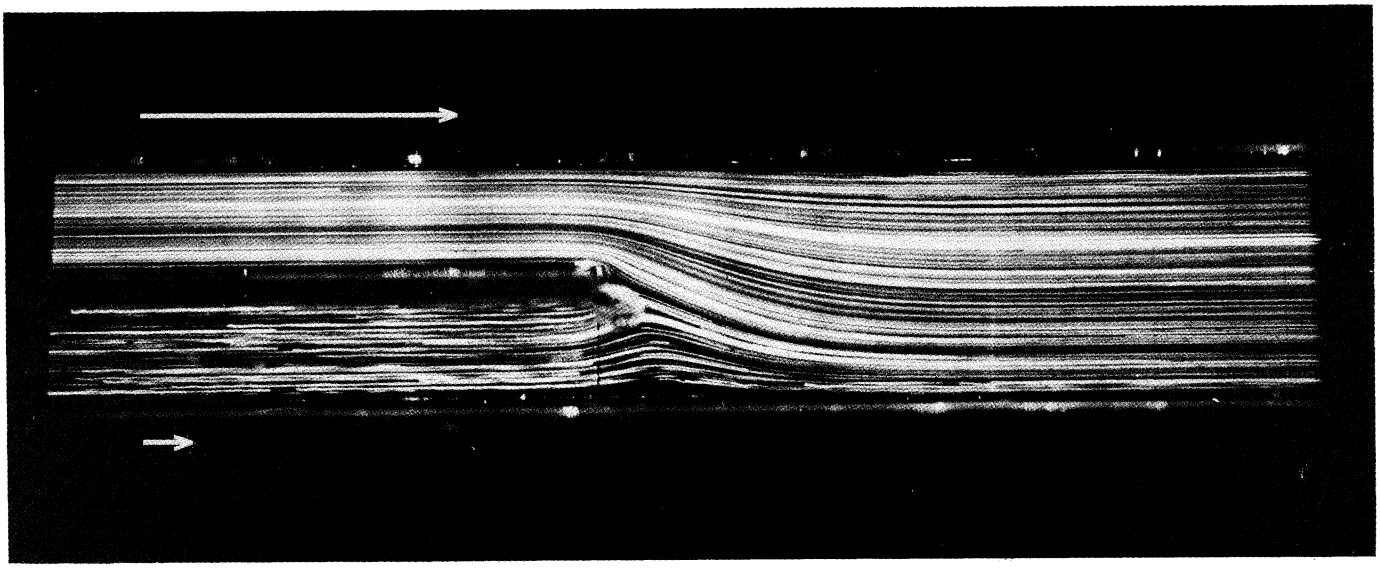

(*b*) $R=10, W=0$

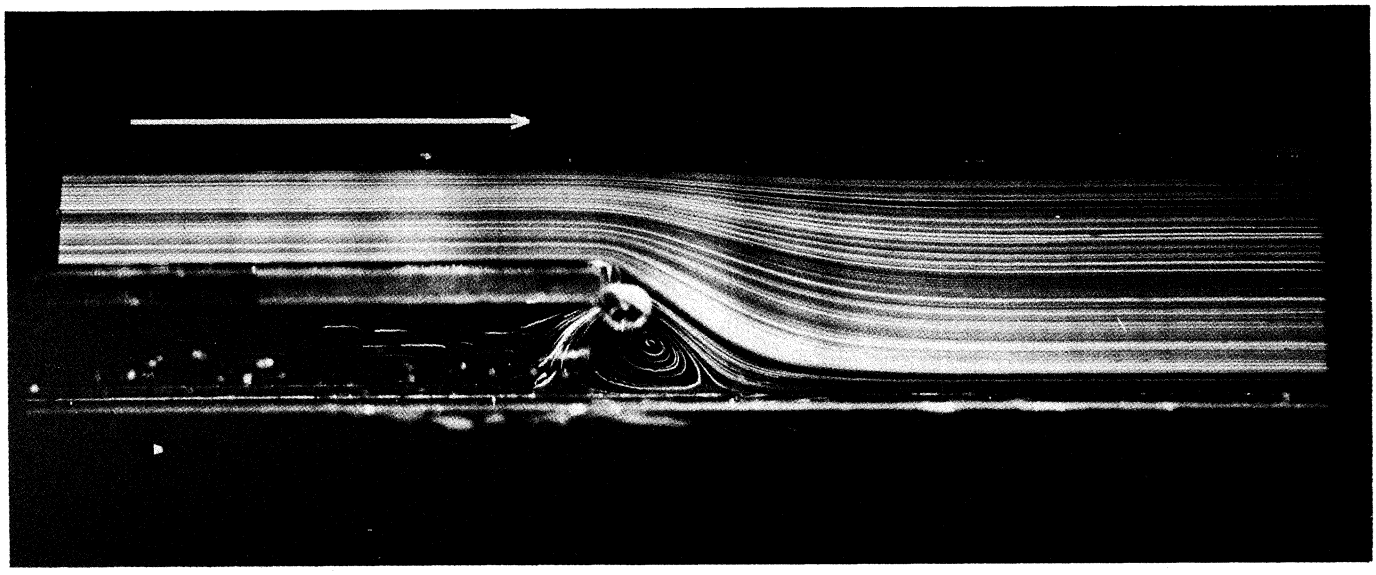

(*c*) $R=10, W=0$

FIGURE 11. Mixing flow: Newtonian liquid; ratio of flow rates is (*a*) 2:1, (*b*) 5:1, (*c*) 100:1; Reynolds number based on flow in wider channel.

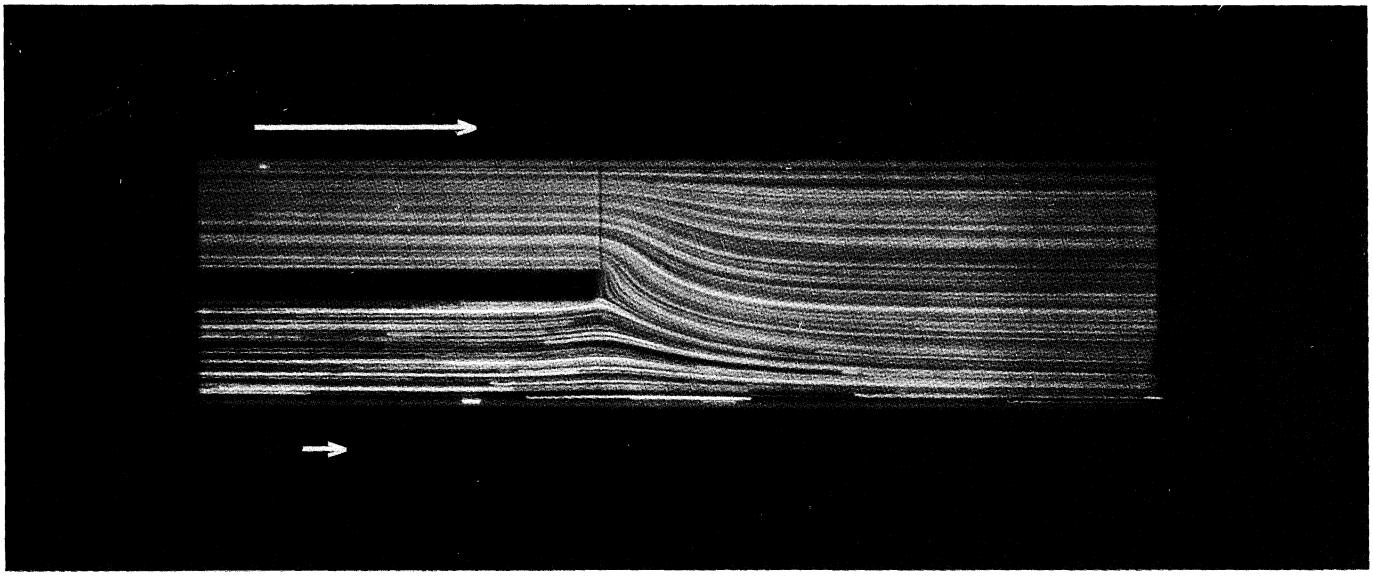

(*a*) $R=5, W=0.25$

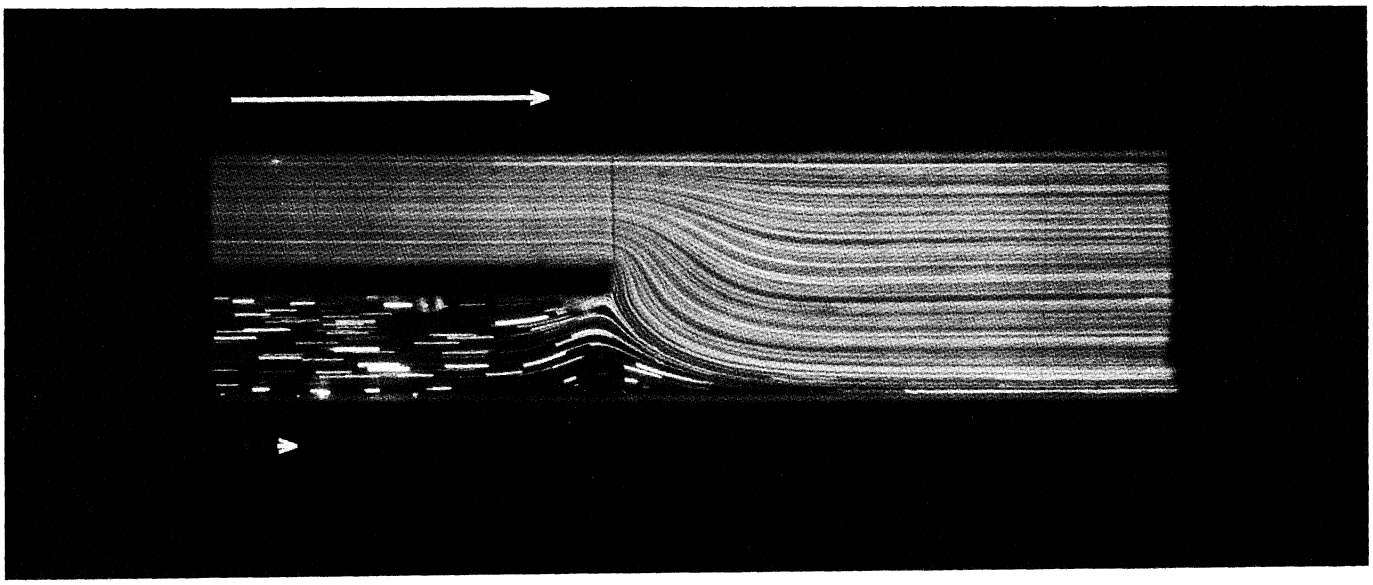

(*b*) $R=5, W=0.25$

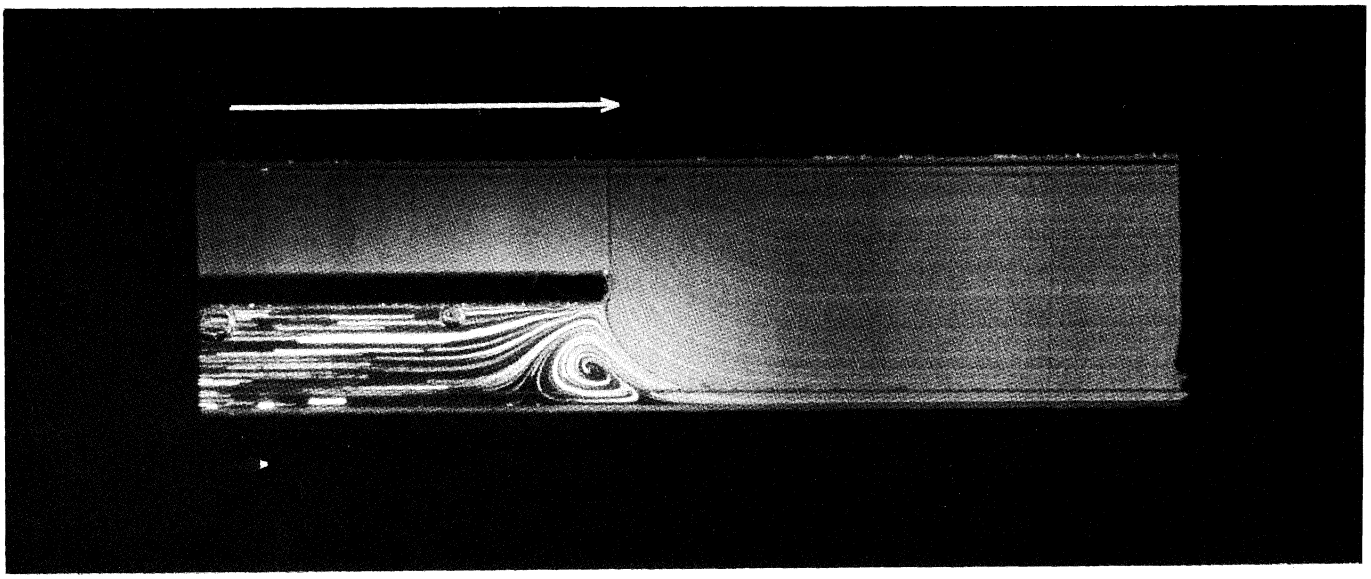

(*c*) $R=5, W=0.25$

FIGURE 12. Mixing flow: liquid B2; ratio of flow rates is (*a*) 5:1, (*b*) 20:1, (*c*) 100:1; Reynolds number and Weissenberg number based on width of wider channel.

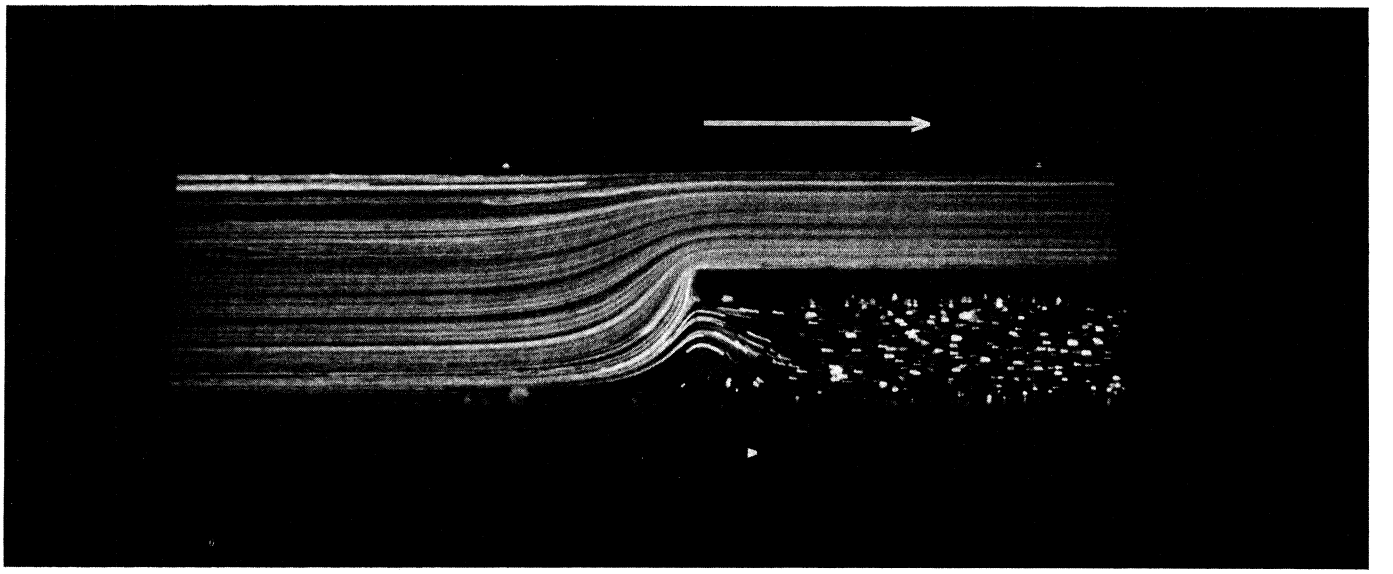

(*a*) $R=5, W=0$

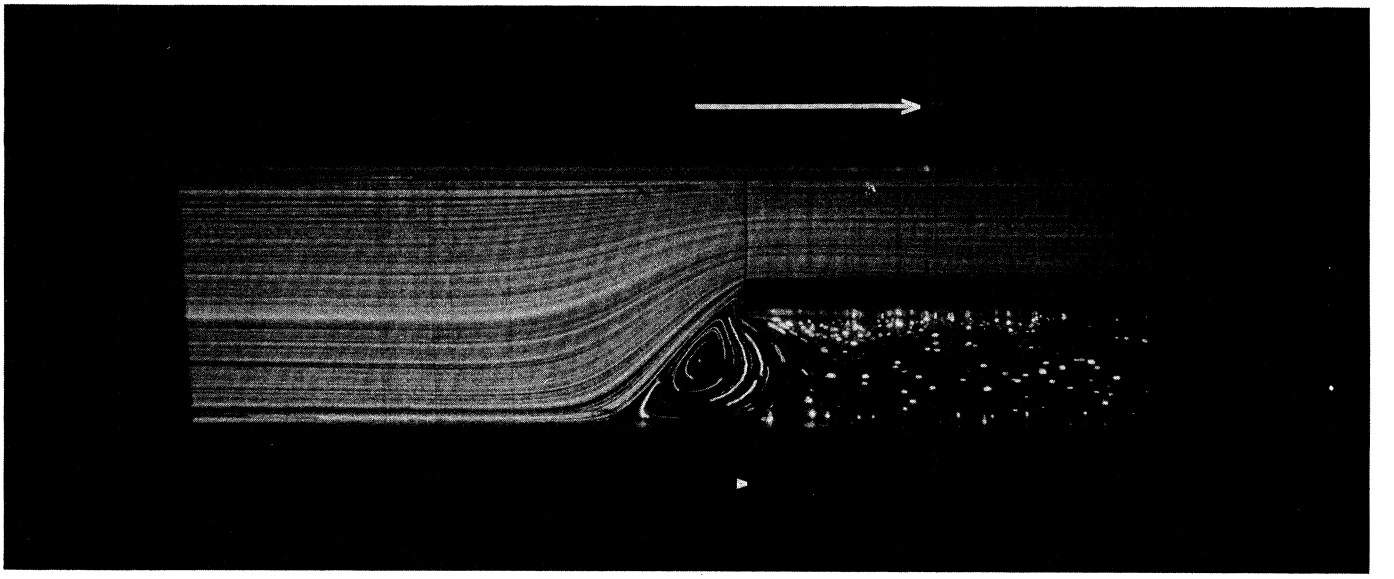

(*b*) $R=5, W=0.25$

FIGURE 13. Separating flow: (*a*) Newtonian liquid, (*b*) liquid B2; ratio of flow rates in the two arms is 100:1; Reynolds number and Weissenberg number based on width of wider channel.

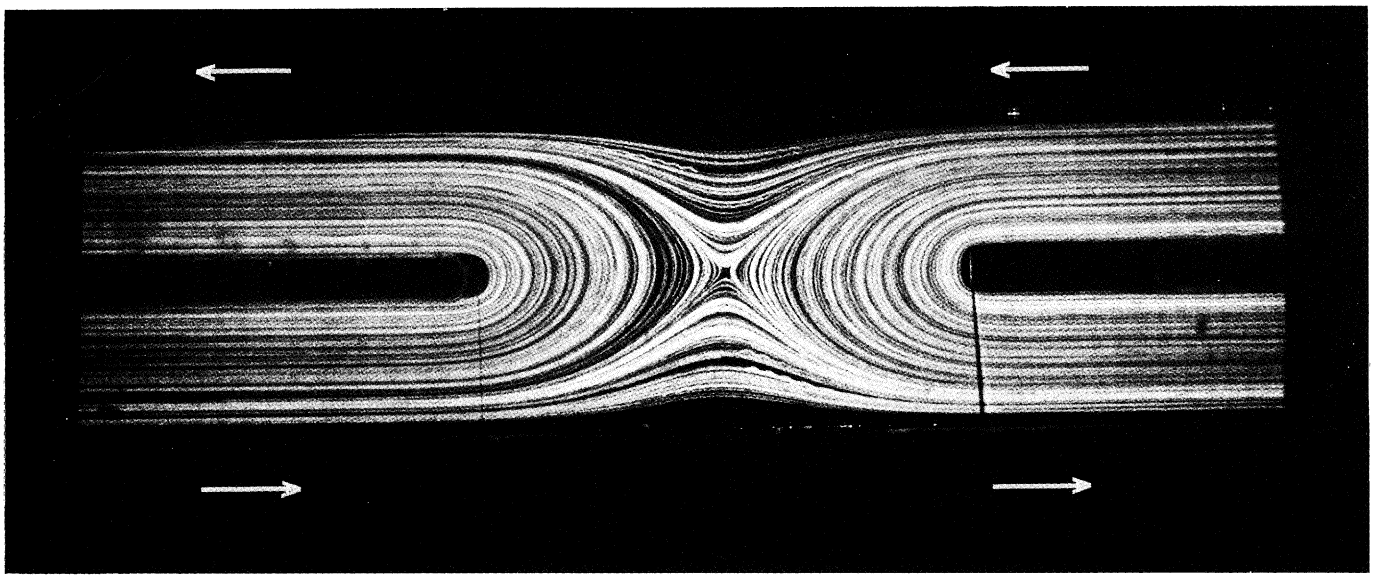

(*a*) $R=5, W=0$

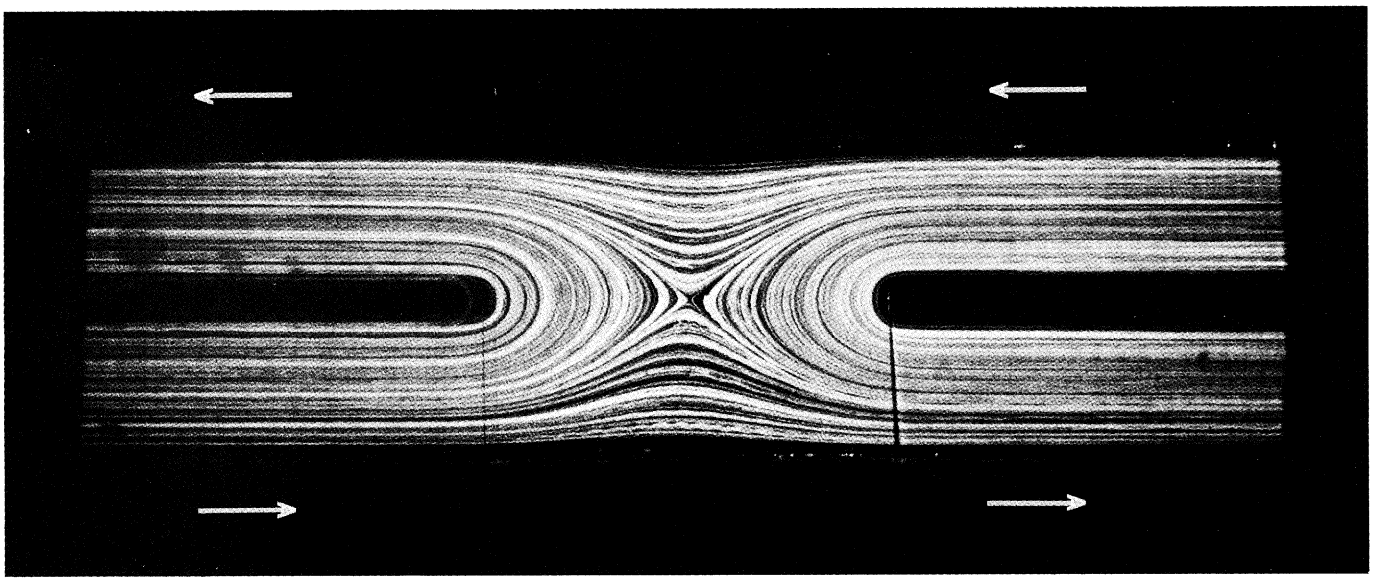

(*b*) $R=5, W=0$

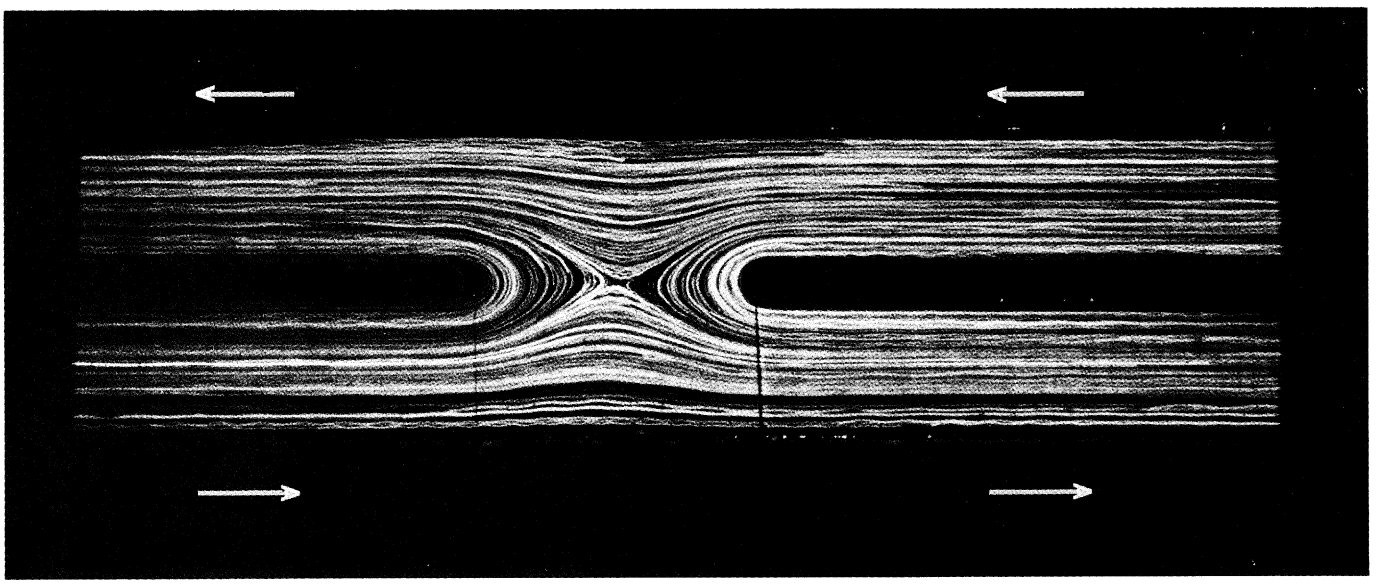

(*c*) $R=5, W=0$

FIGURE 14. Combined mixing and separating flow: Newtonian liquid; variable gap l, (*a*) $l = 18$ mm, (*b*) $l = 15$ mm, (*c*) $l = 10$ mm; flow rate in all arms equal; Reynolds number based on flow in one of the arms.

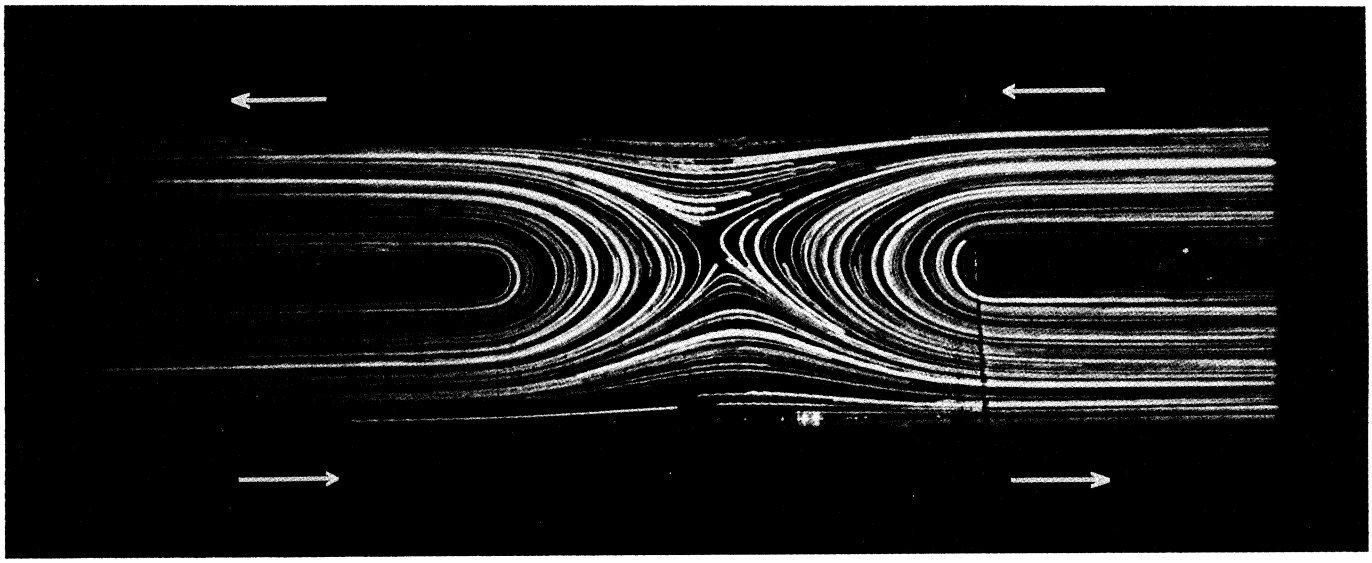

(*a*) $R=5, W=0.75$

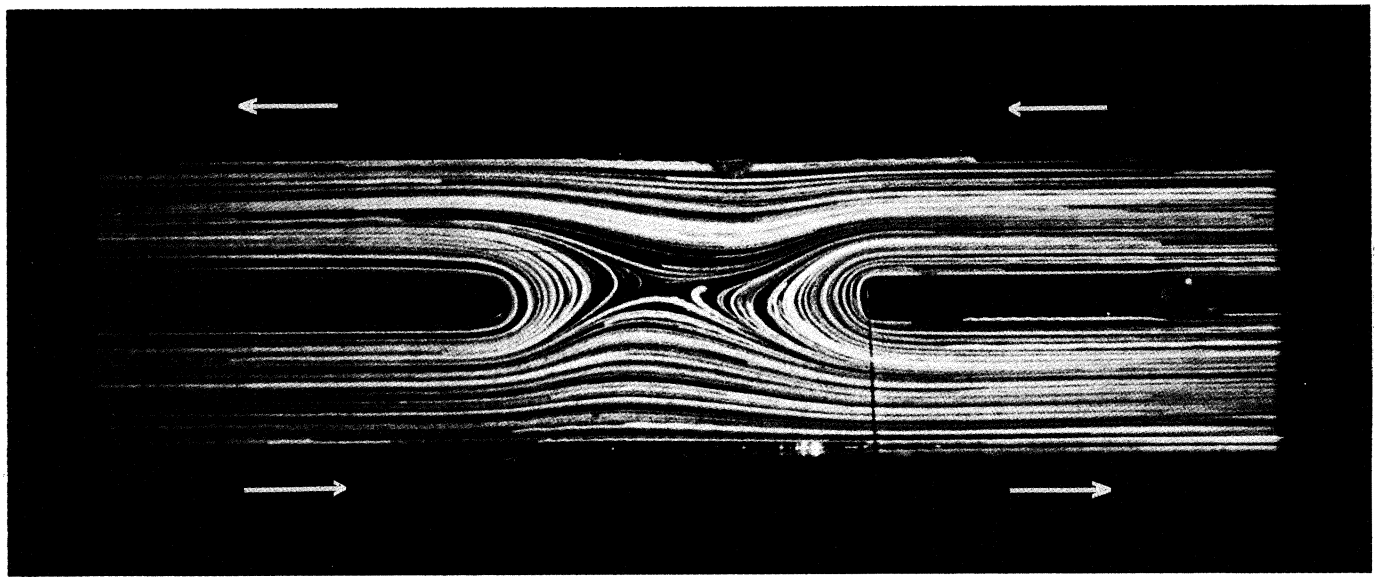

(*b*) $R=5, W=0.75$

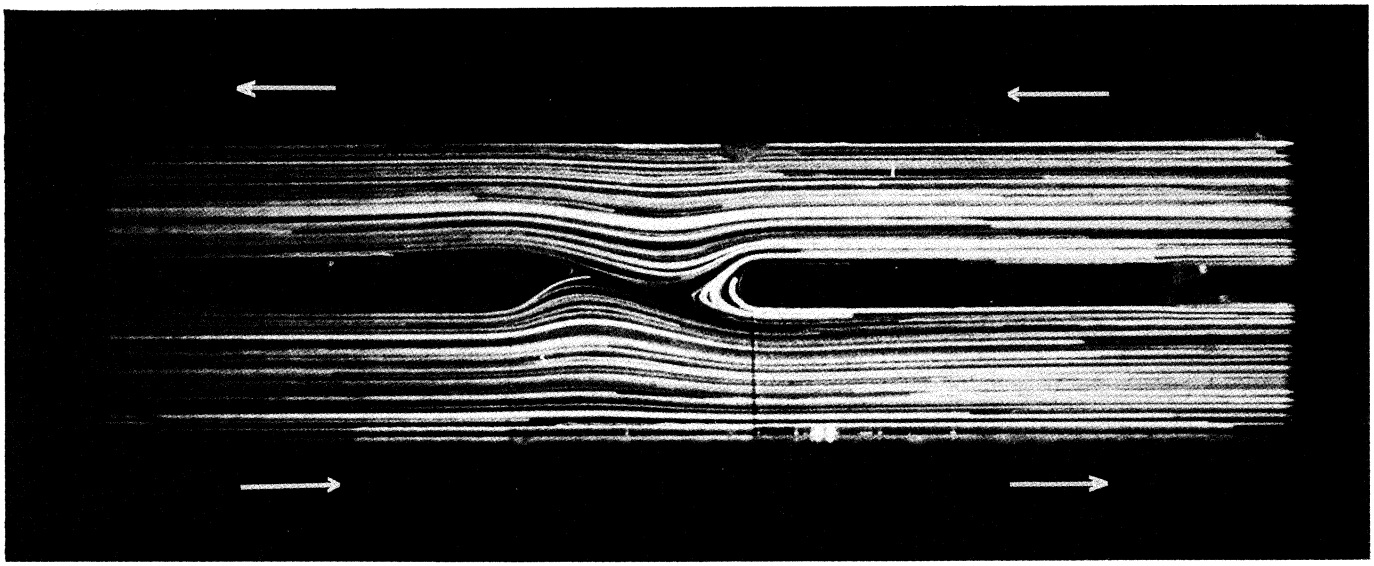

(*c*) $R=5, W=0.75$

FIGURE 15. Combined mixing and separating flow: as for figure 14 with liquid B3; Reynolds number and Weissenberg number based on width of one of the arms.

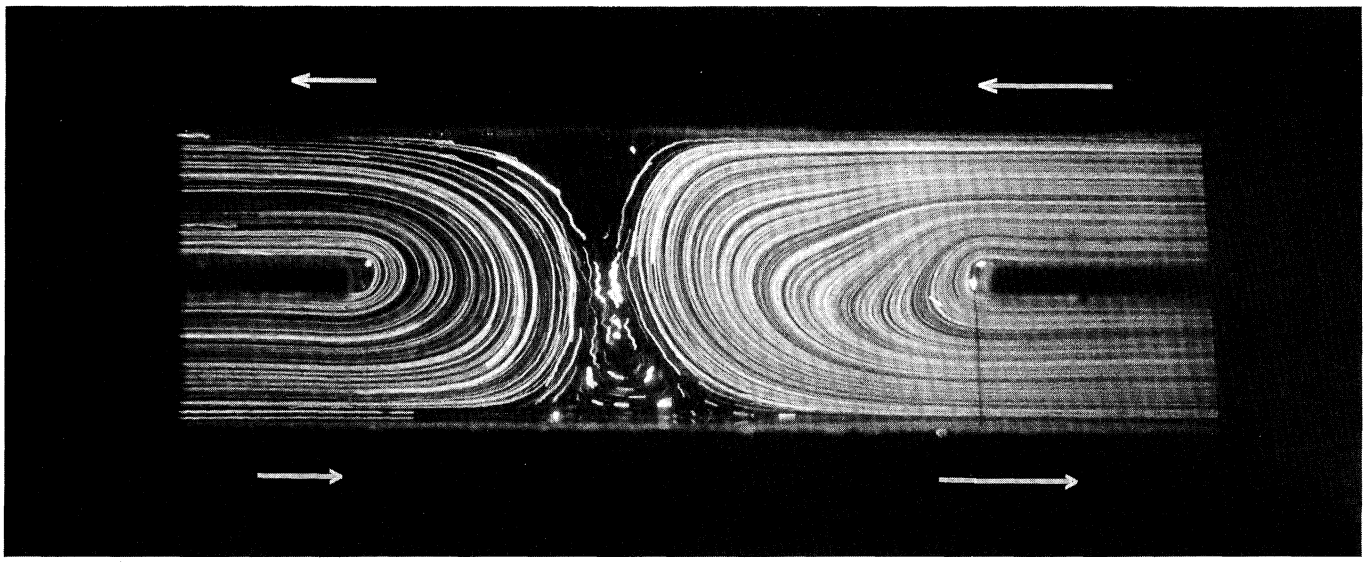

(*a*) $R=1, W=0.23$

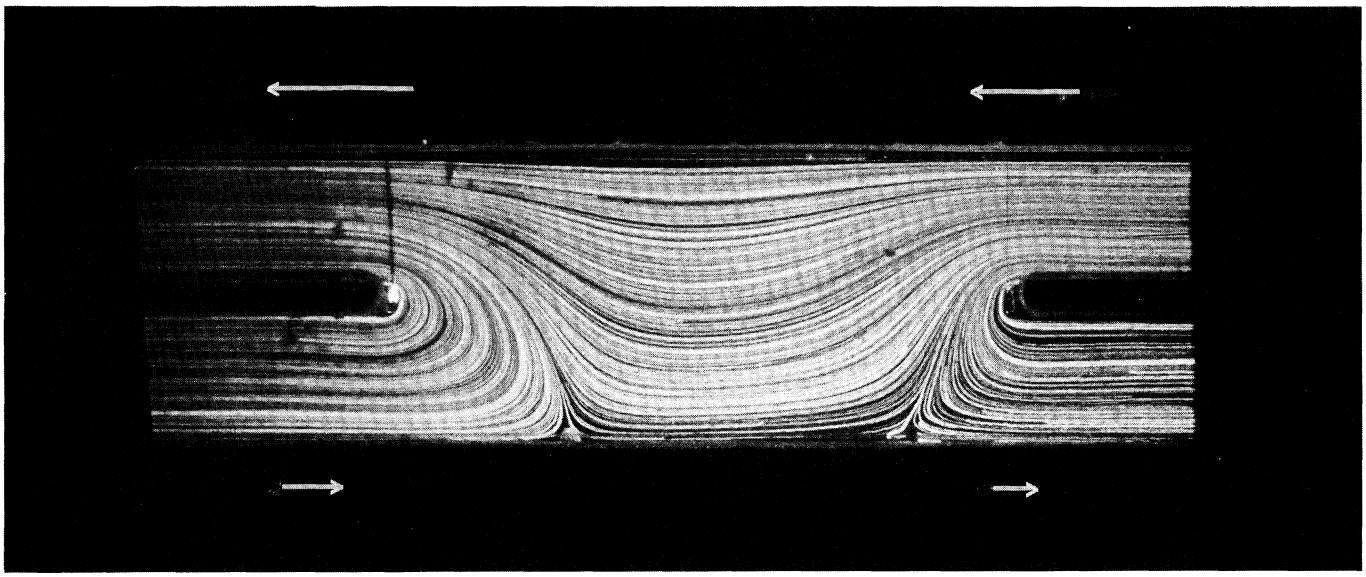

(*b*) $R=0.75, W=0.17$

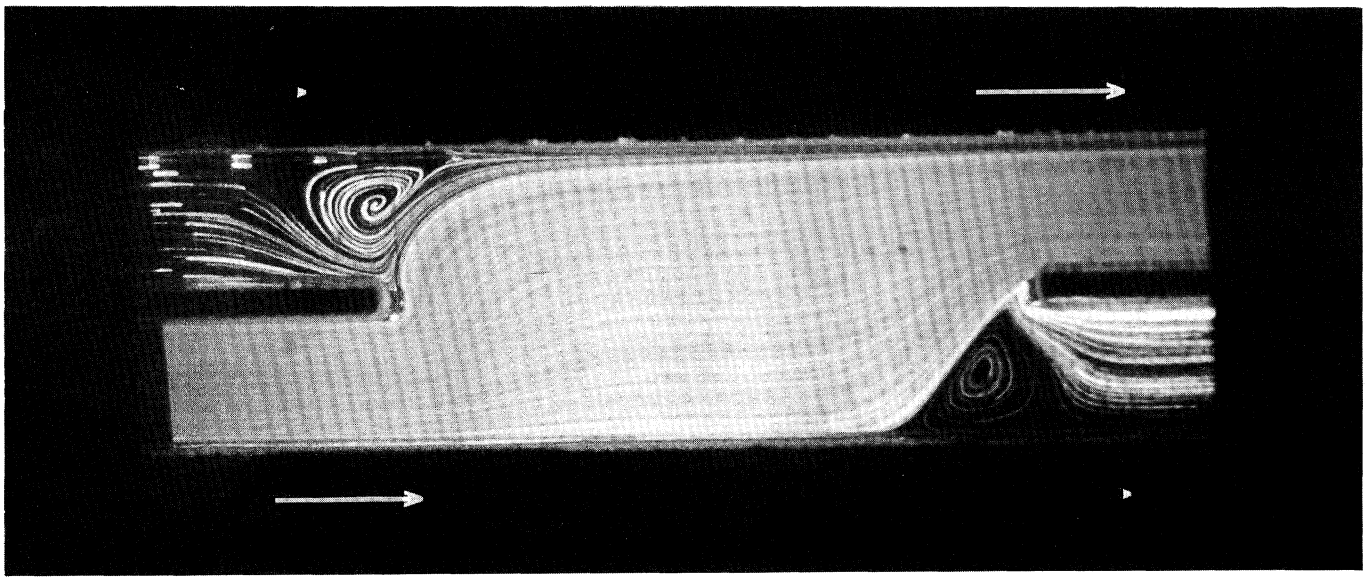

(*c*) $R=1, W=0.23$

FIGURE 16. Combined mixing and separating flow: liquid B2; gap $l = 25$ mm; relative flow rates indicated by lengths of arrows; Reynolds number and Weissenberg number based on flow rate measurement in upper right arm.

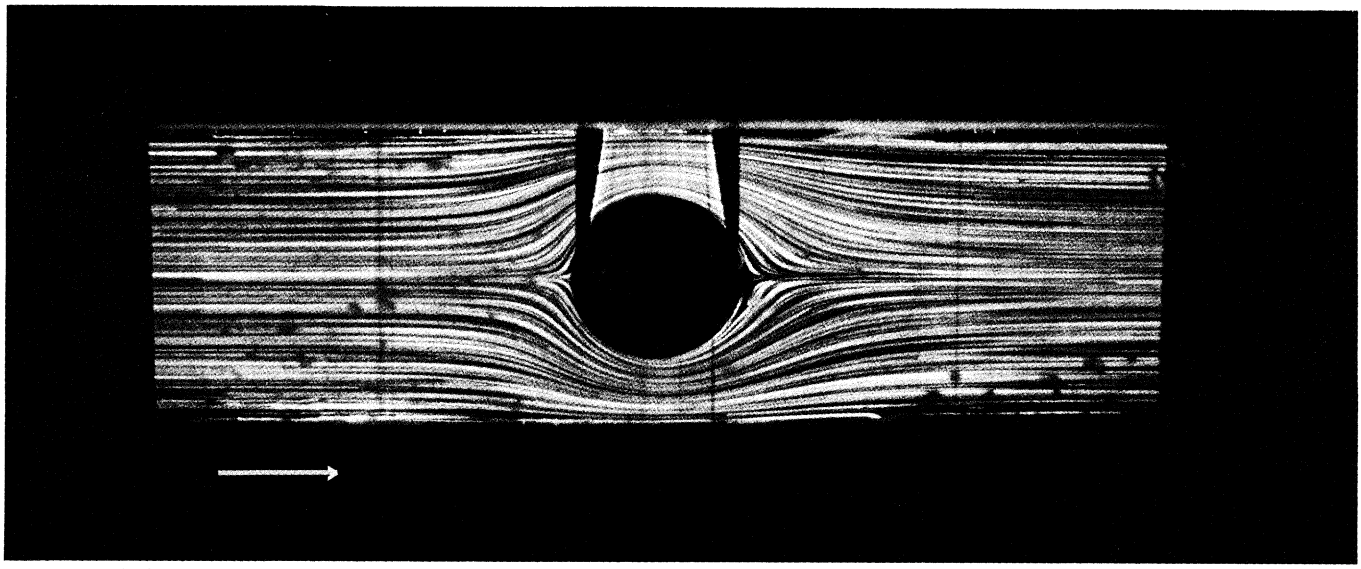

(*a*) $R=5, W=0$

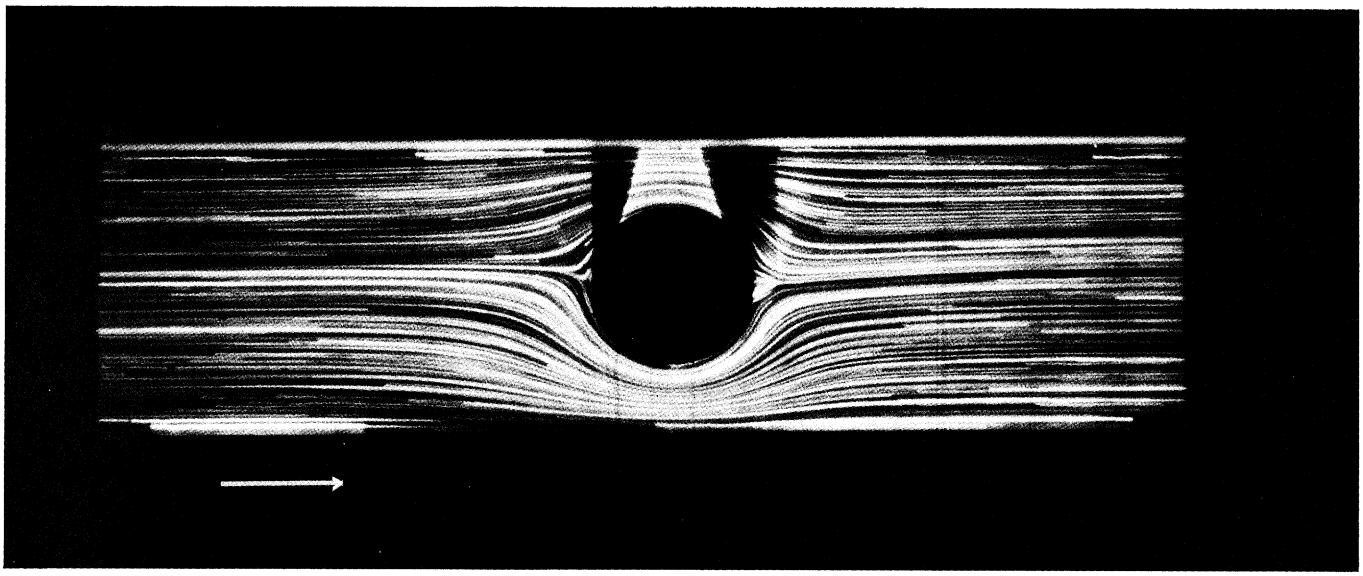

(*b*) $R=5, W=0.1$

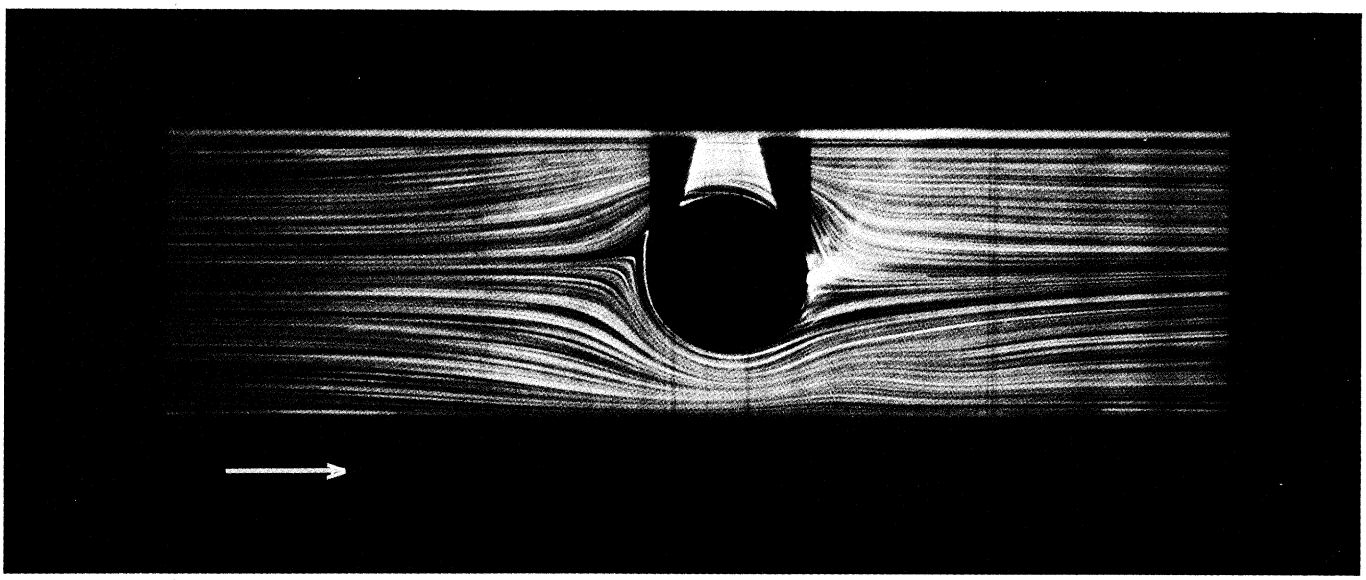

(*c*) $R=10, W=0.2$

FIGURE 17. Flow past a cylinder: (*a*) Newtonian, (*b*) and (*c*) liquid B1.

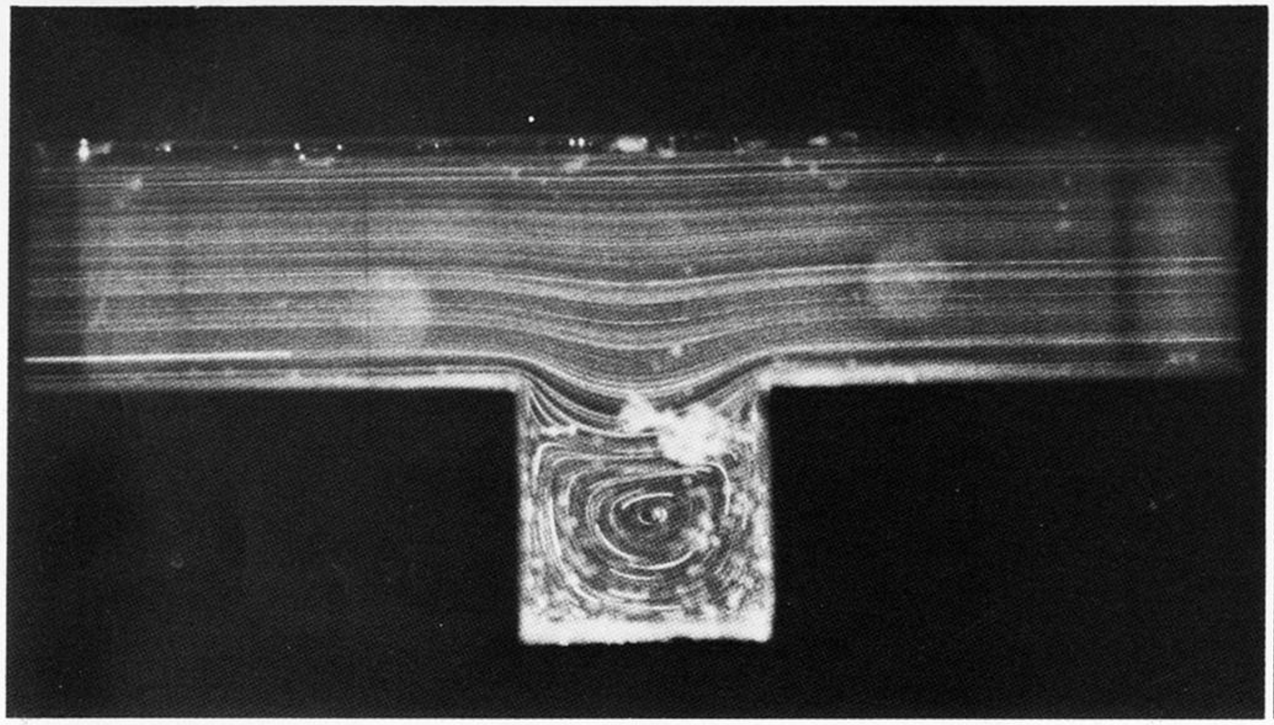

(*a*) $R=1, W=0$

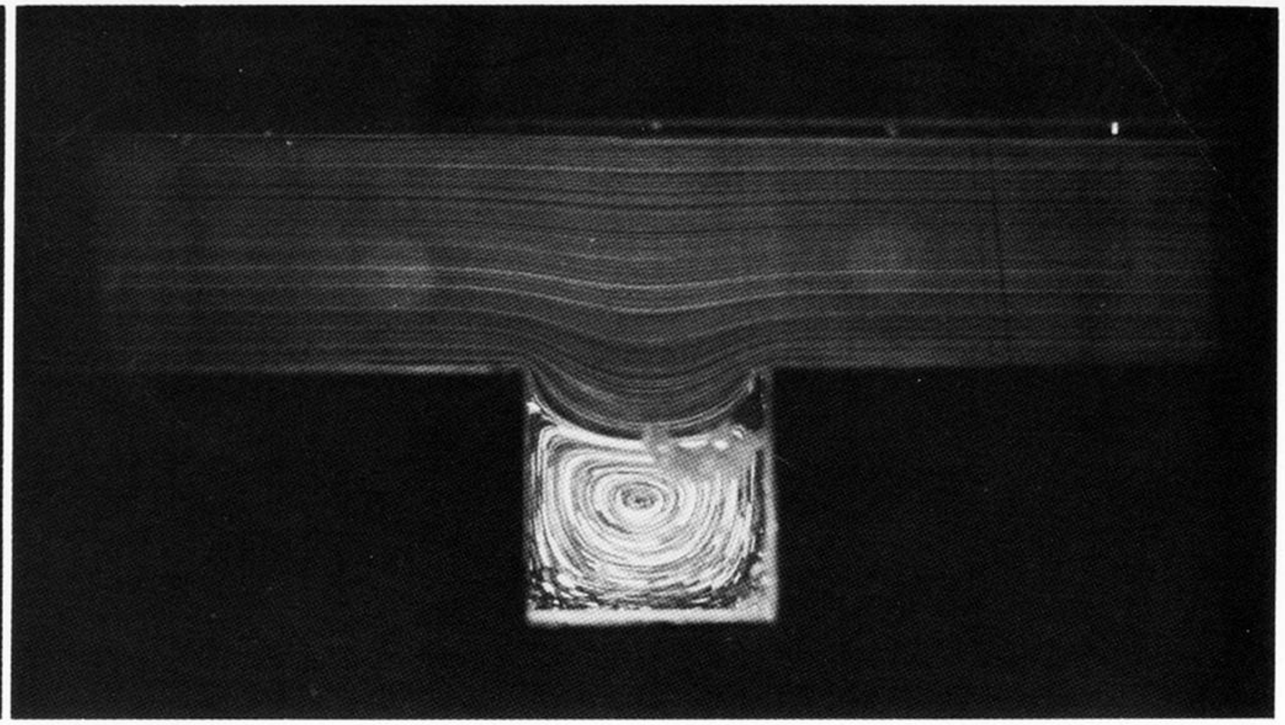

(*b*) $R=1, W=0.02$

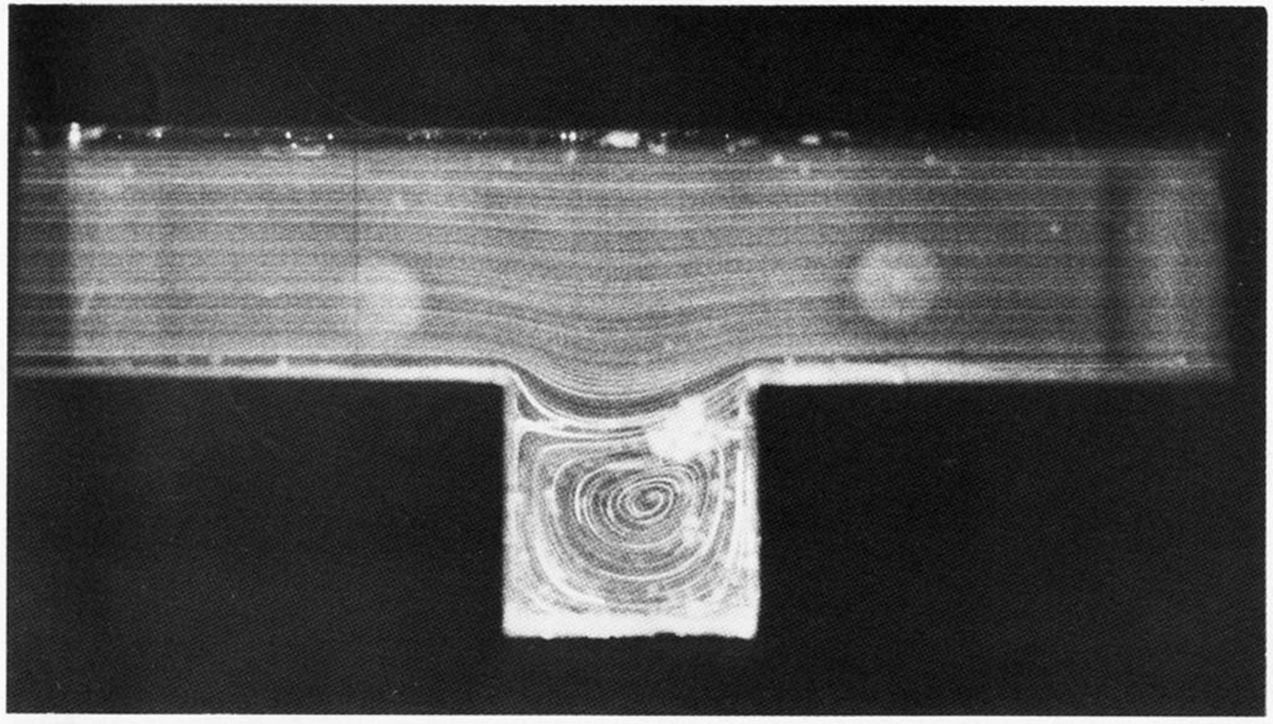

(*c*) $R=5, W=0$

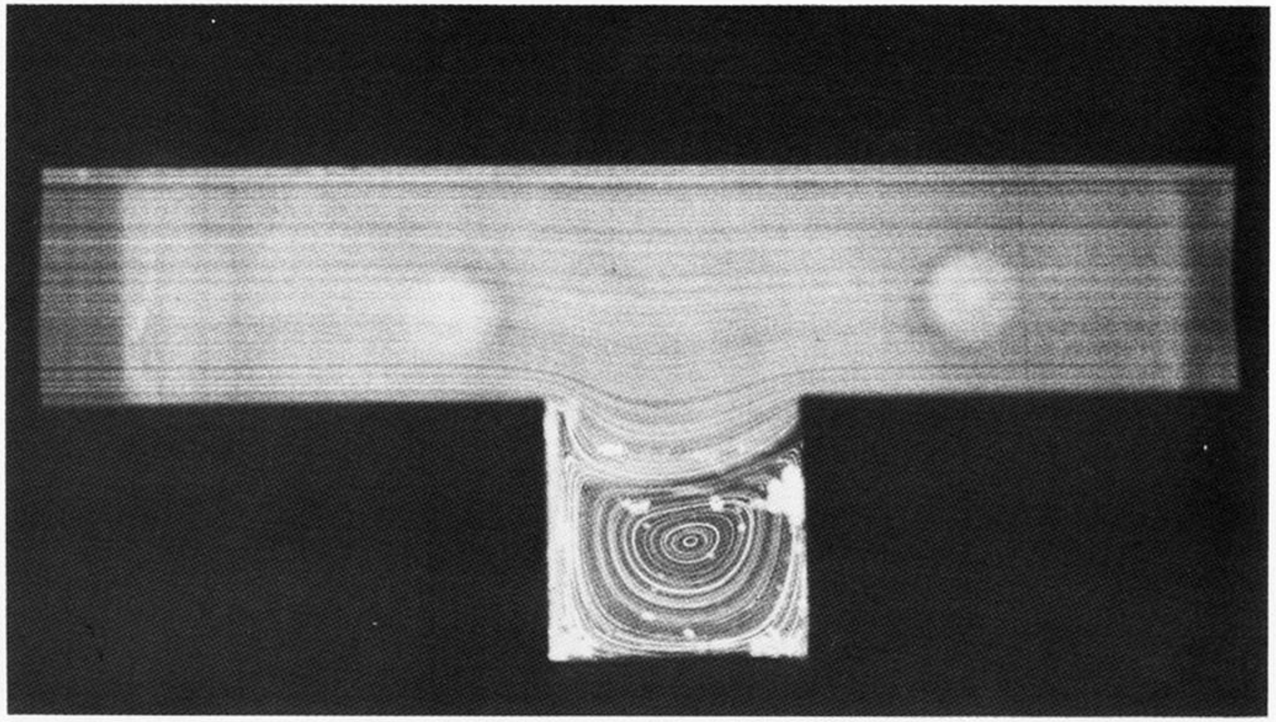

(*d*) $R=5, W=0.1$

FIGURE 5. Flow over a square hole: (*a*) and (*c*) Newtonian, (*b*) and (*d*) liquid B1.

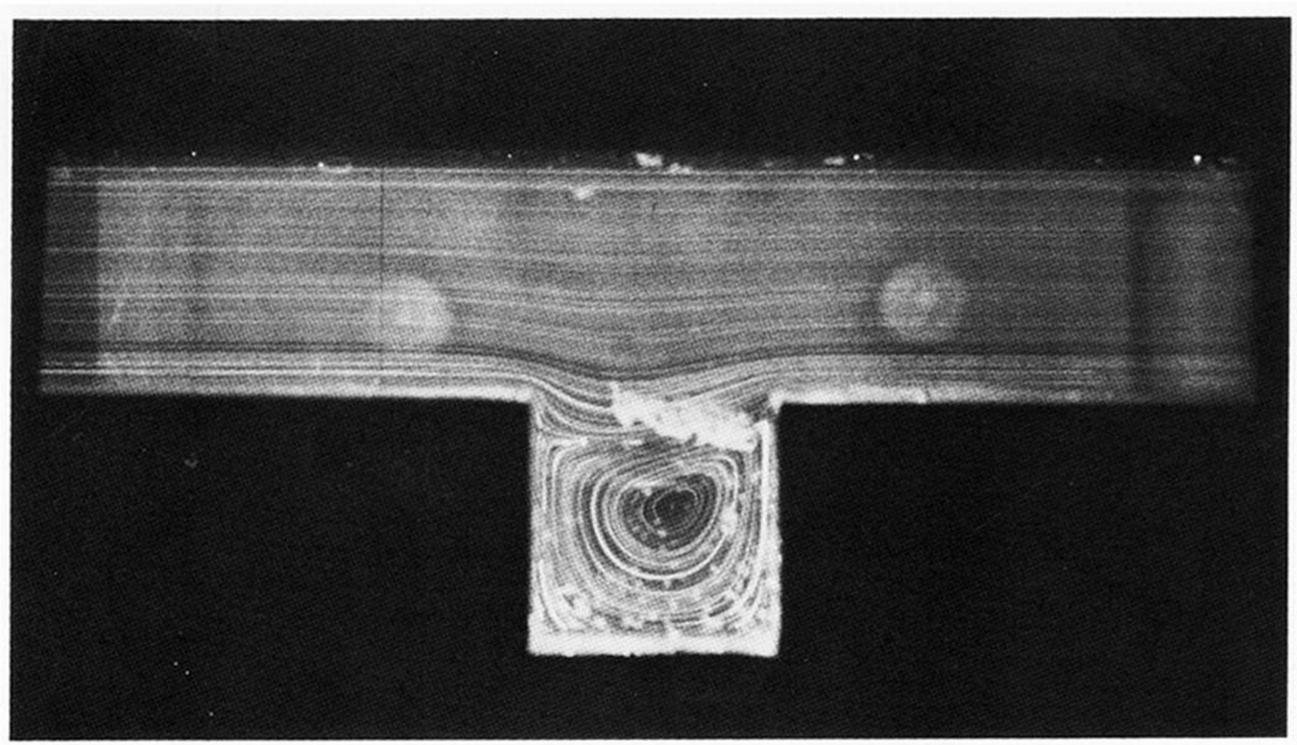

(a) $R=10, W=0$

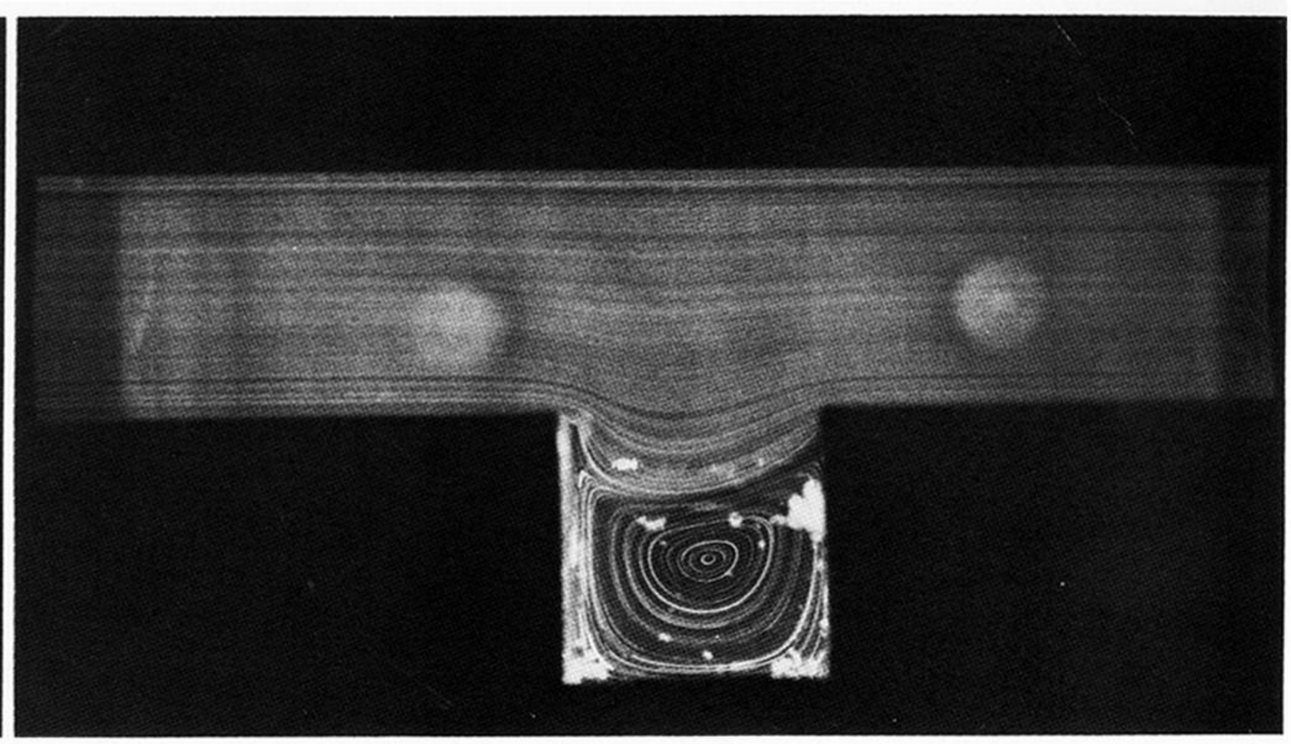

(b) $R=10, W=0.2$

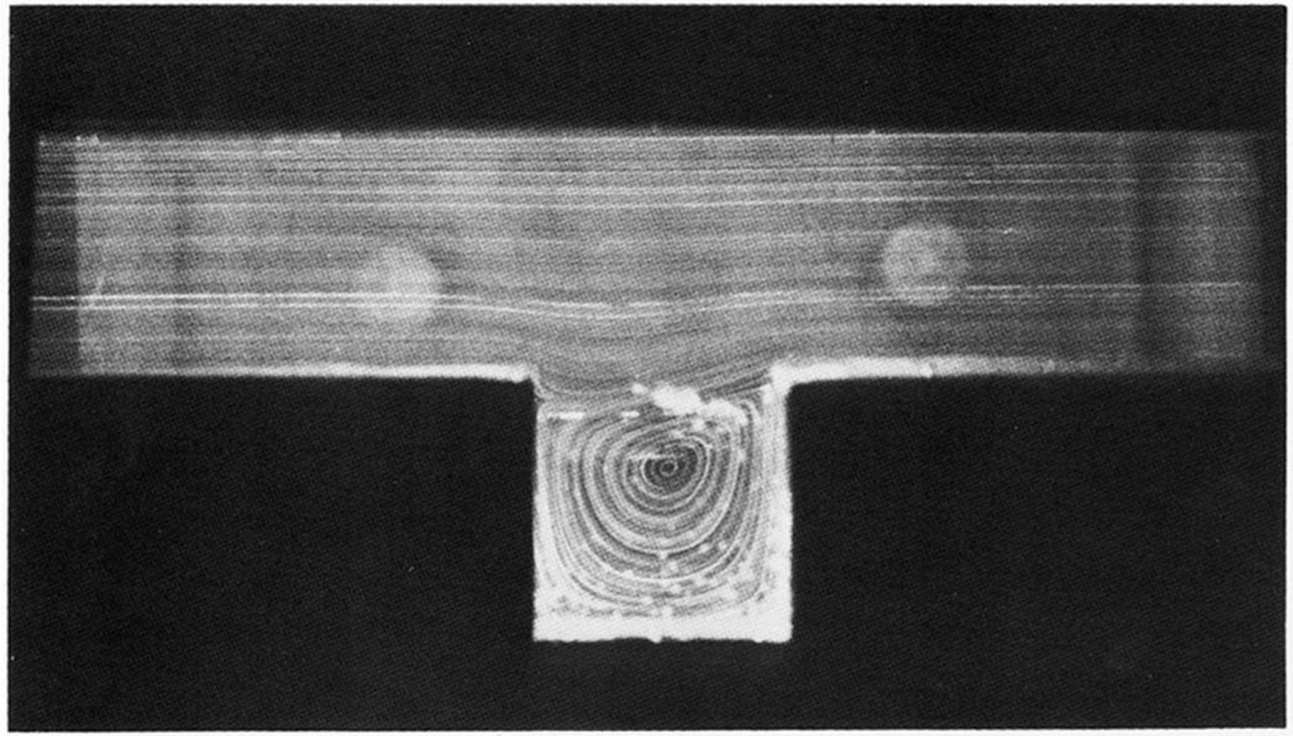

(c) $R=20, W=0$

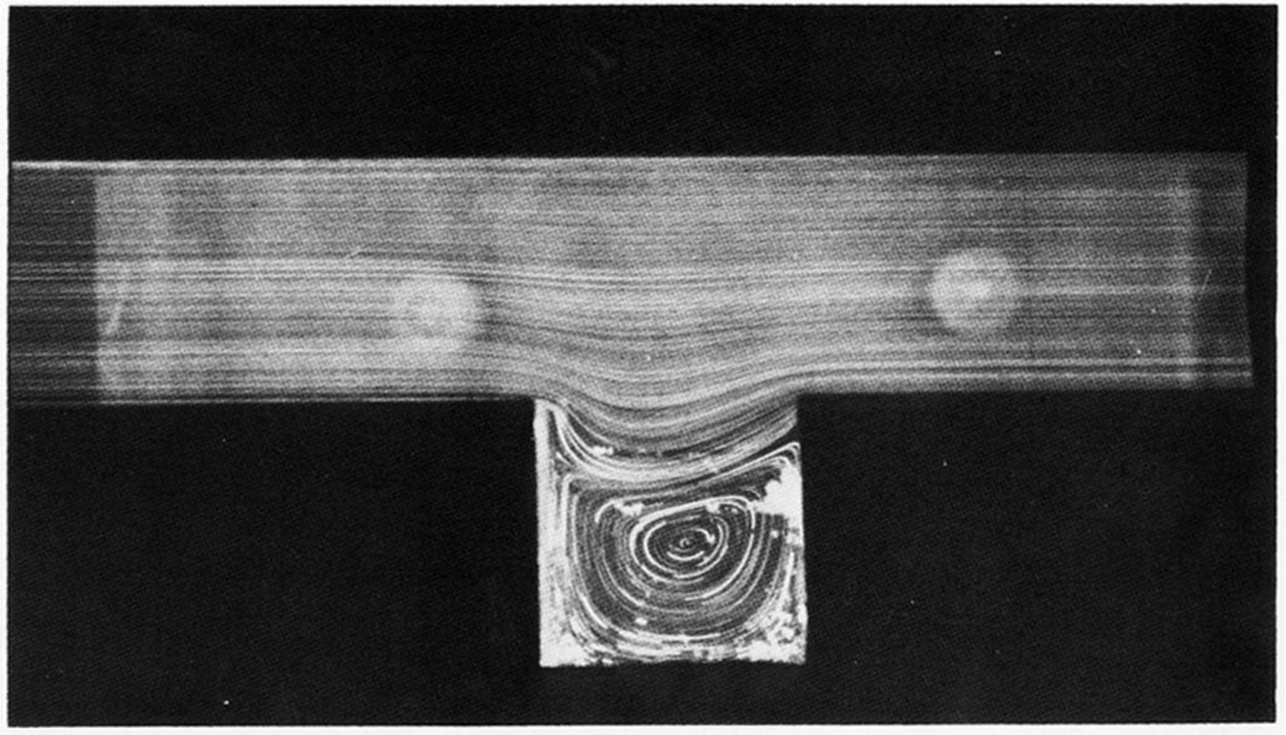

(d) $R=20, W=0.4$

FIGURE 6. Flow over a square hole: (*a*) and (*c*) Newtonian, (*b*) and (*d*) liquid B1.

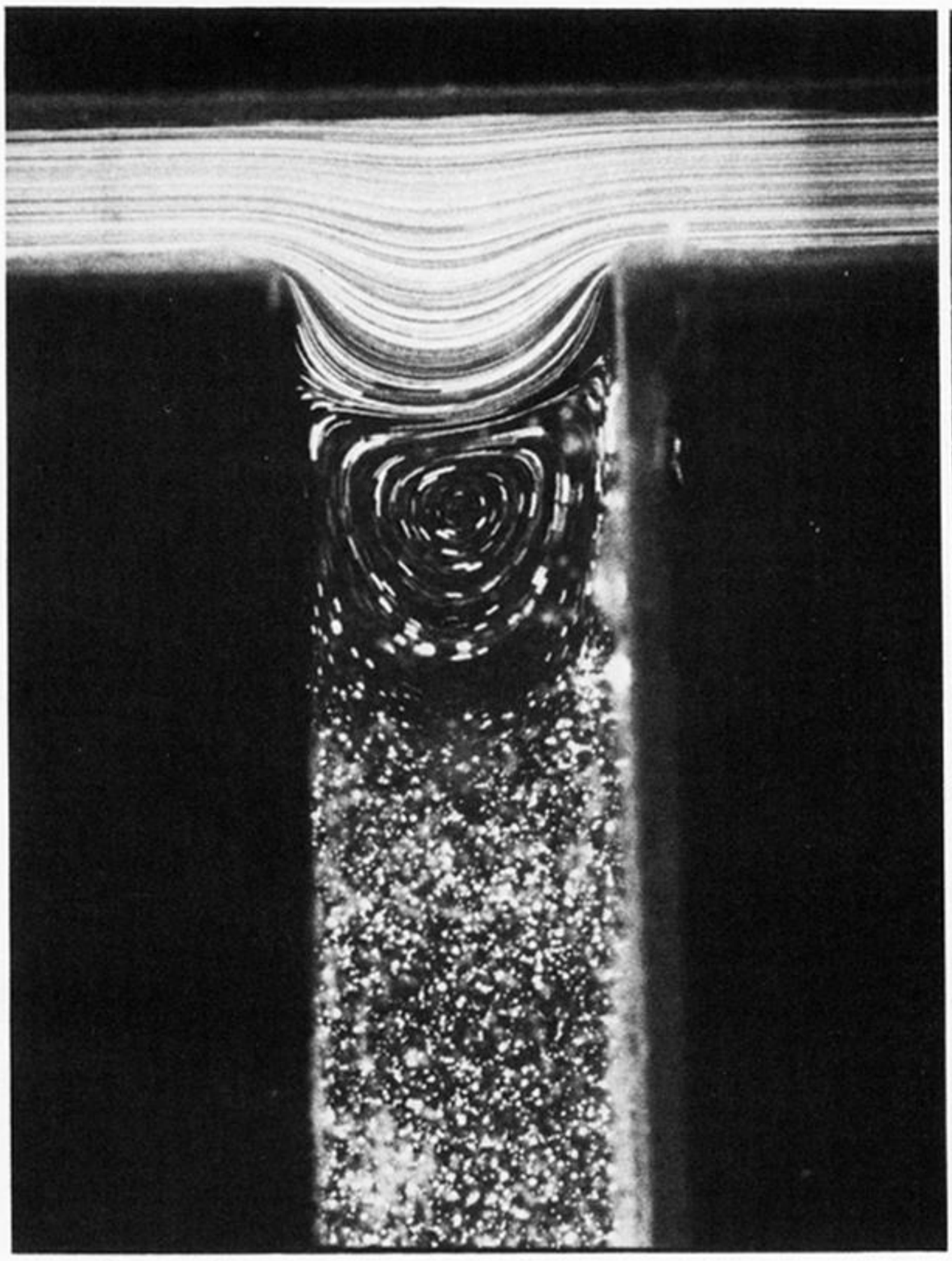

(a) $R=3, W=0$

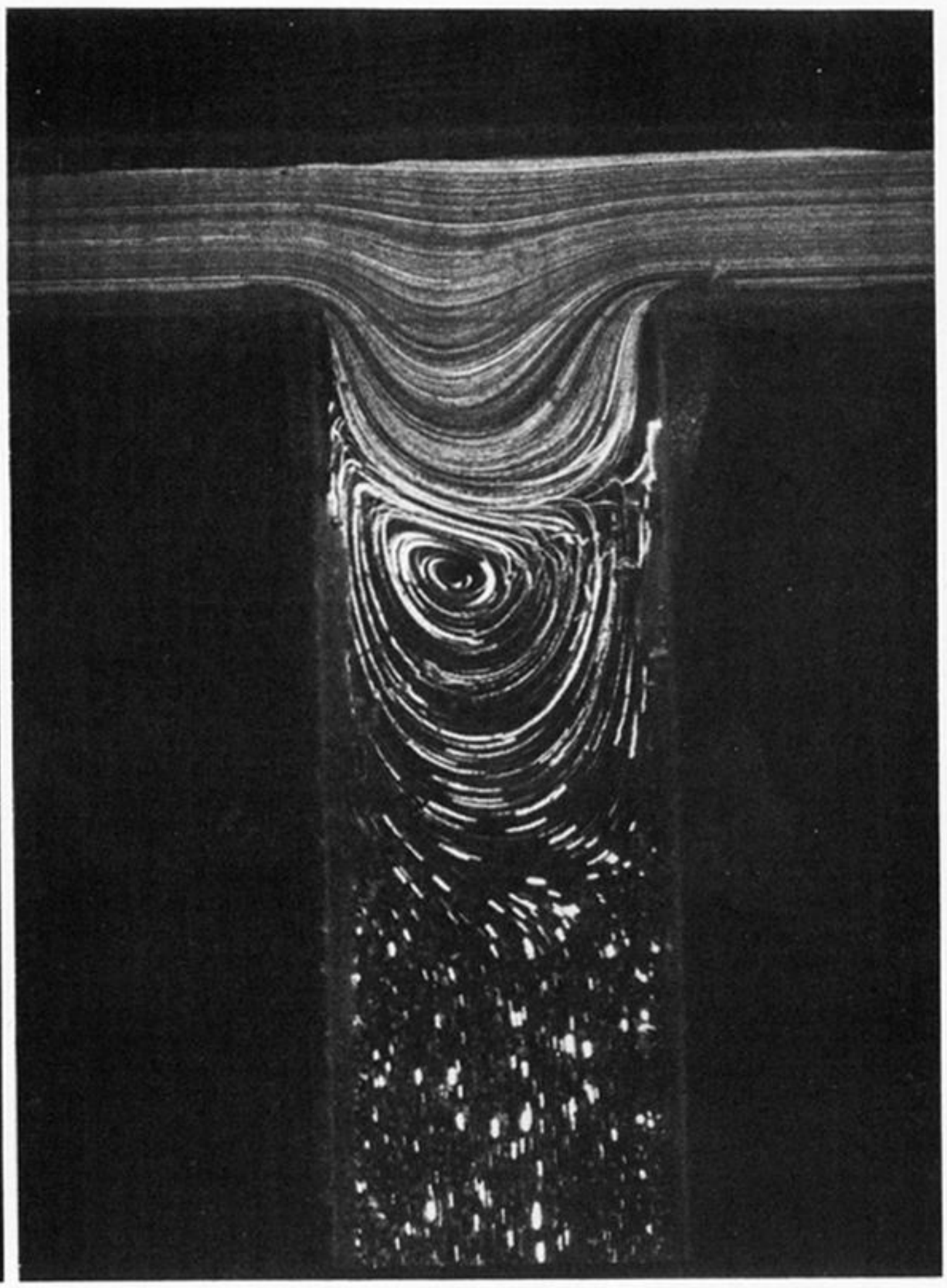

(b) $R=3, W=0.38$

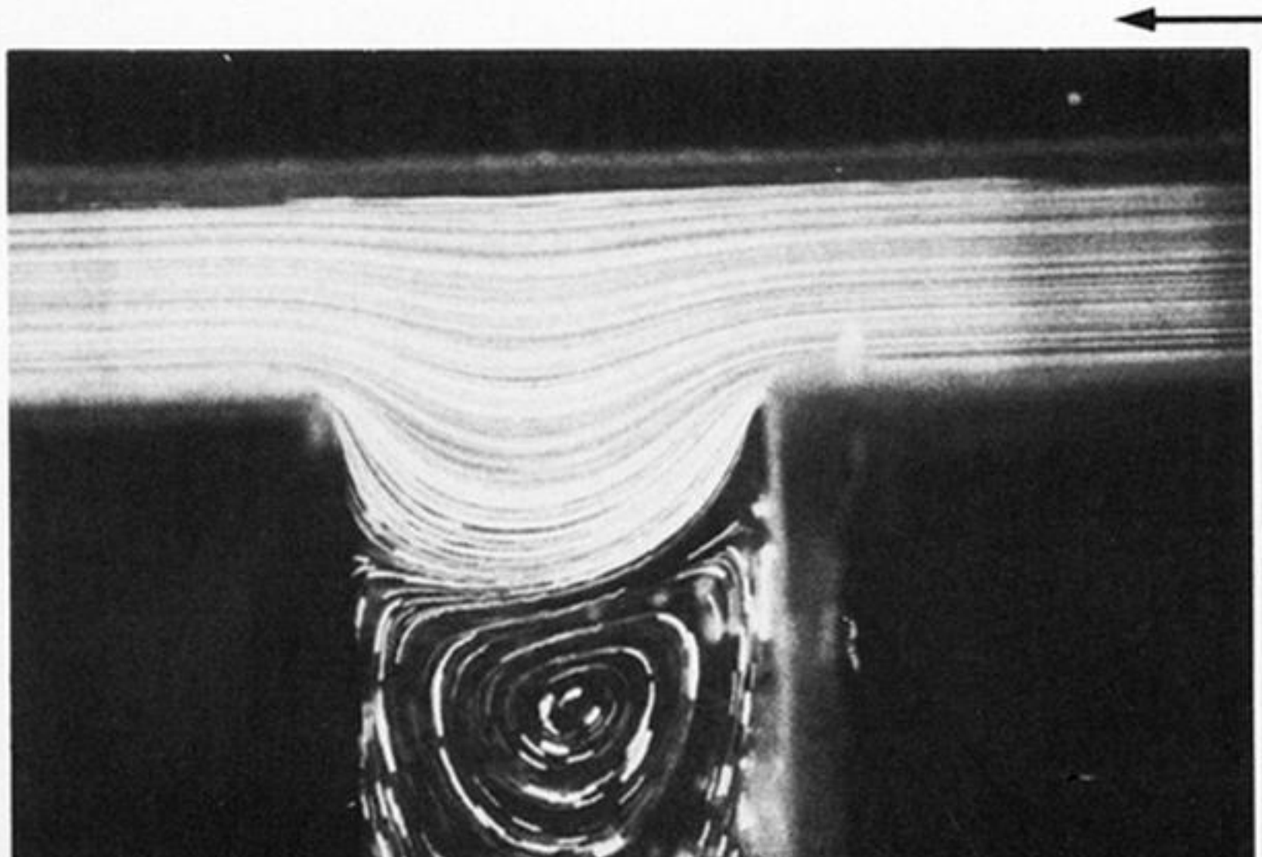

(c) $R=6, W=0$

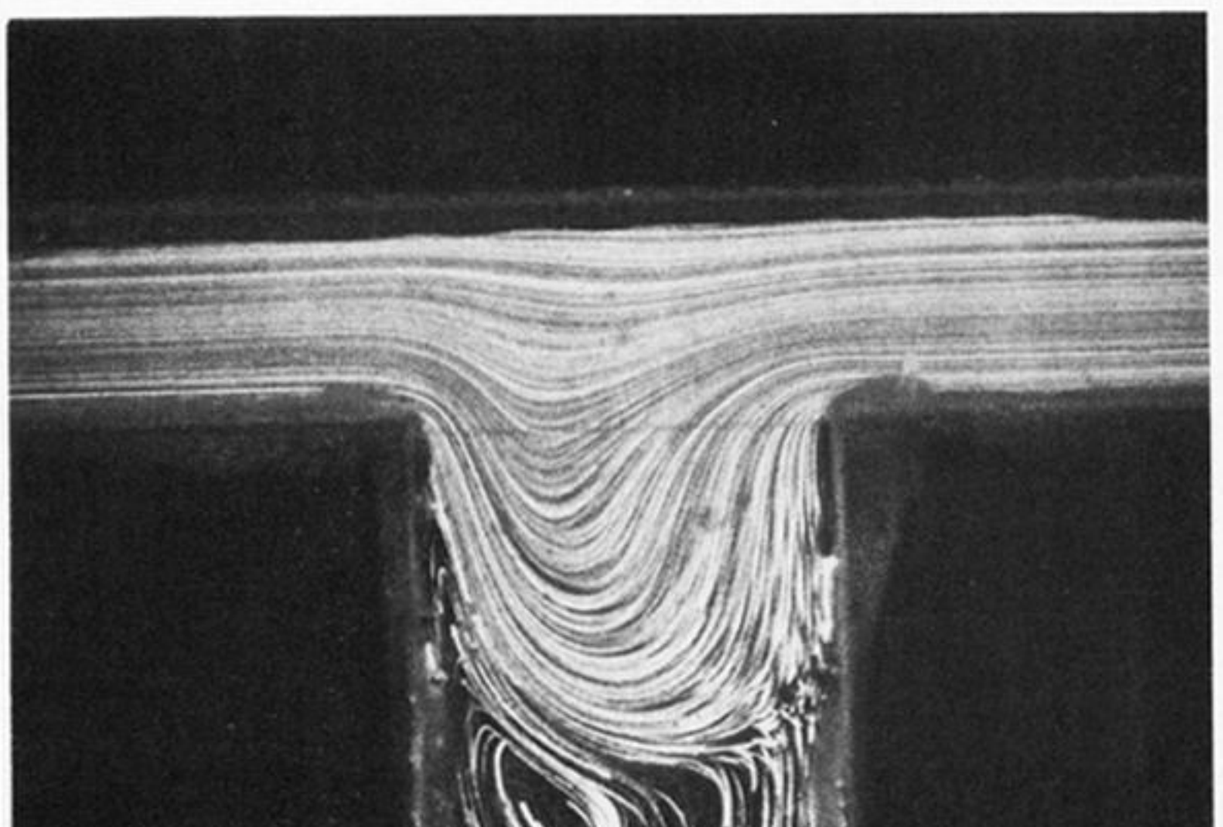

(d) $R=6, W=0.75$

FIGURE 7. Flow over a deep hole: (*a*) and (*c*) Newtonian, (*b*) and (*d*) liquid B3.

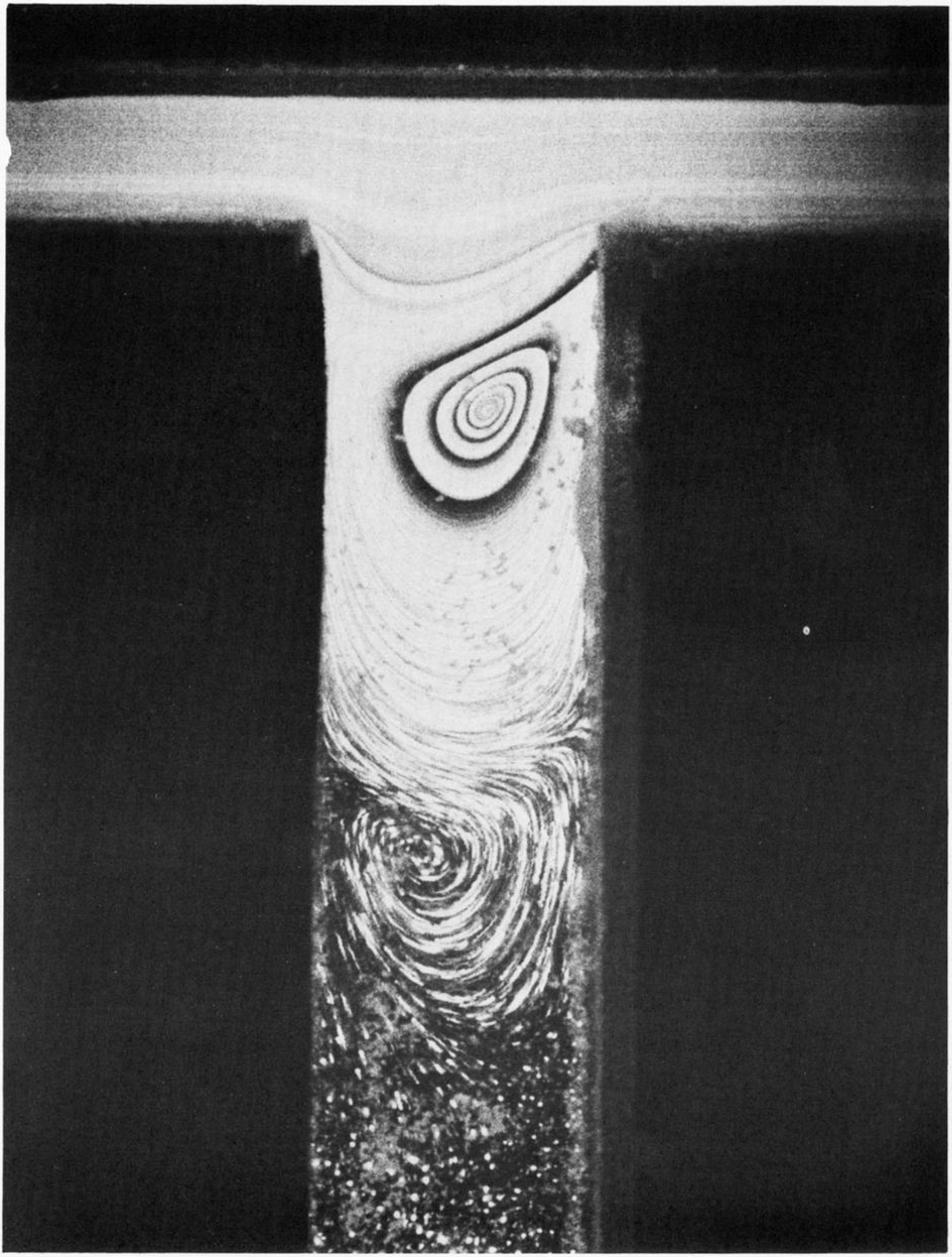

$R=20, W=0$

FIGURE 8. Flow over a deep hole: exposure time, 10 minutes.

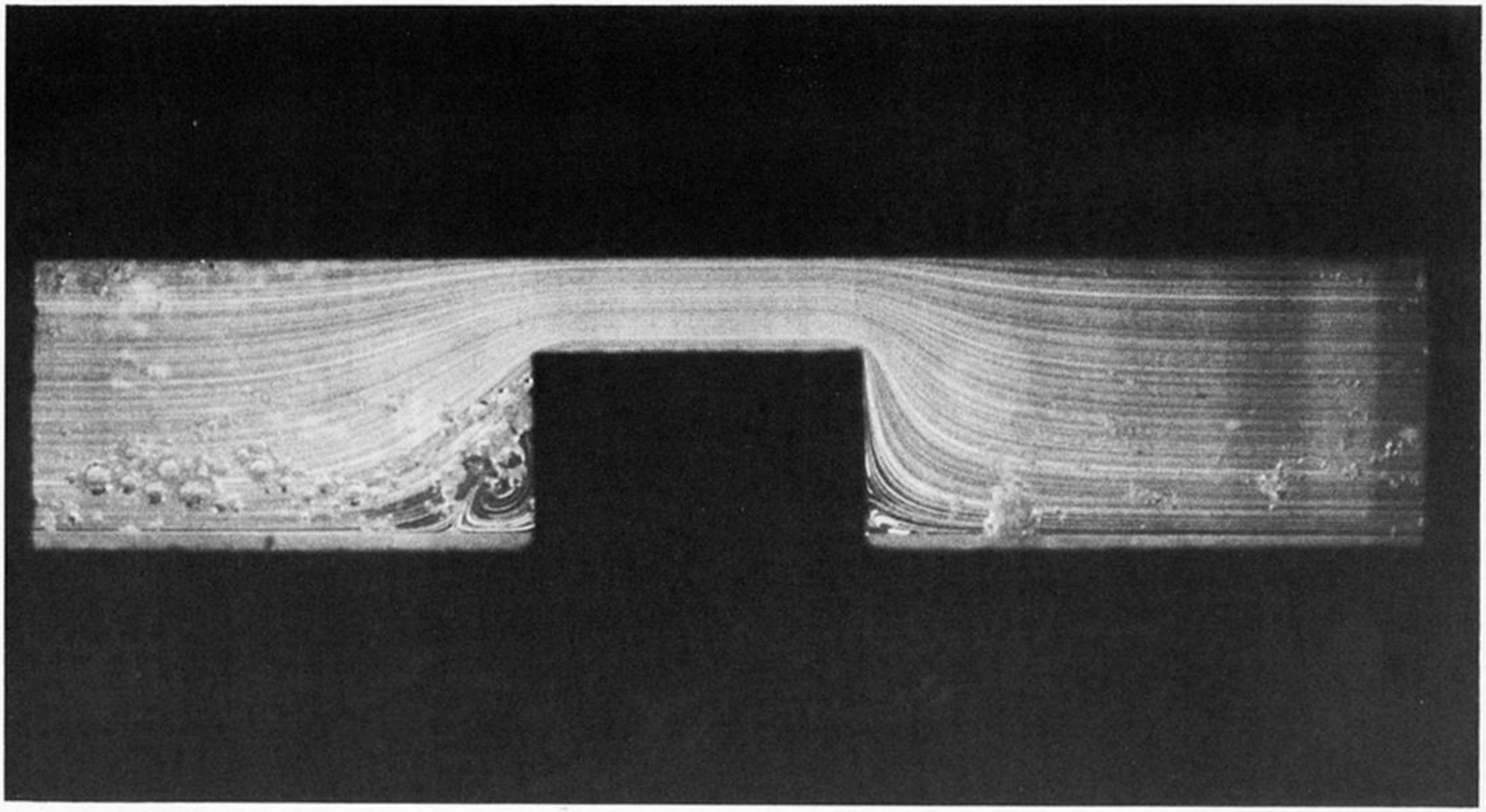

(*a*) $R=5, W=0$

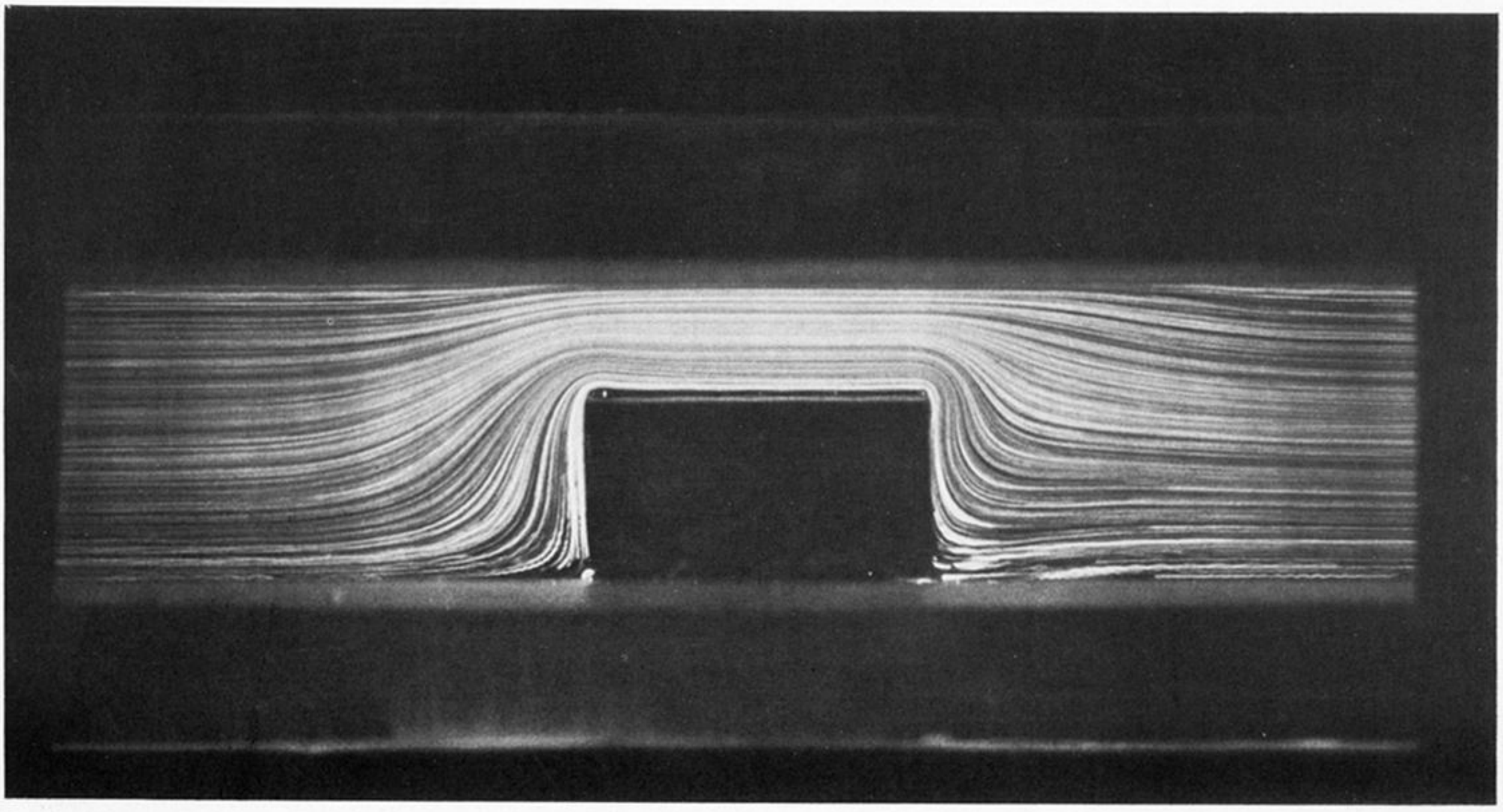

(*b*) $R=5, W=0.1$

FIGURE 9. Flow over a rectangular protuberance: (*a*) Newtonian, (*b*) liquid B1.

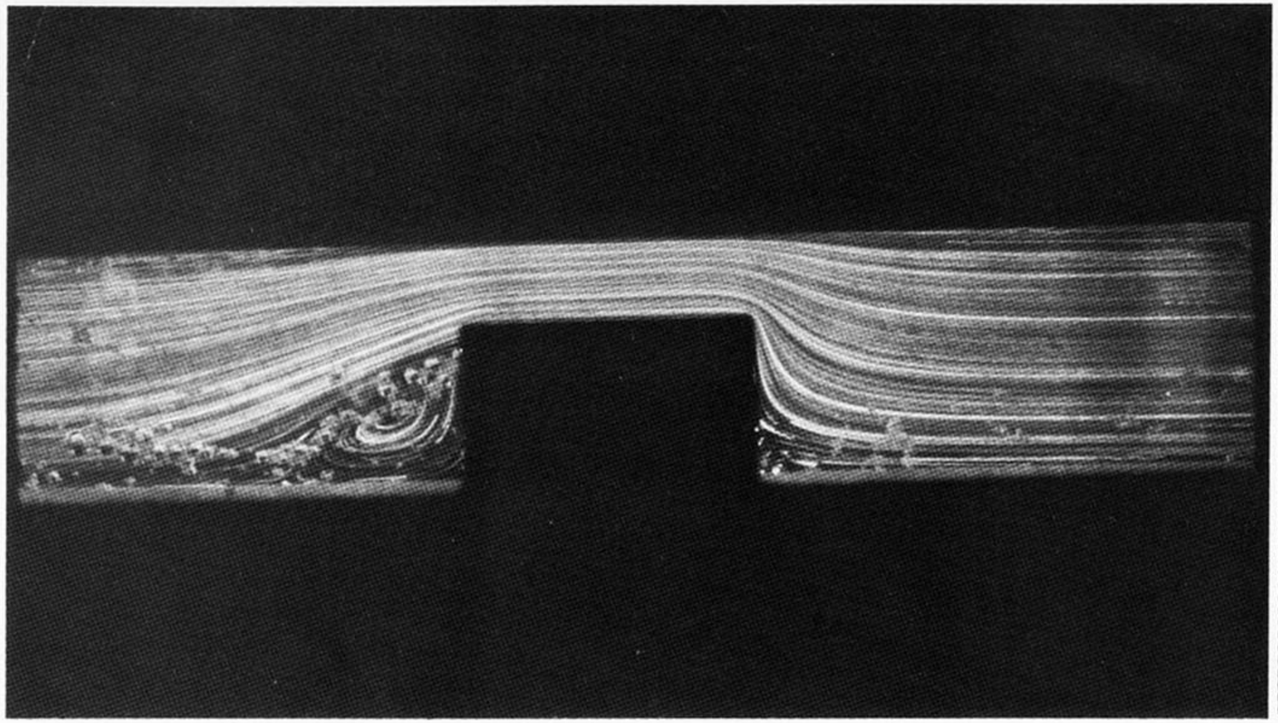

(a) $R=20, W=0$

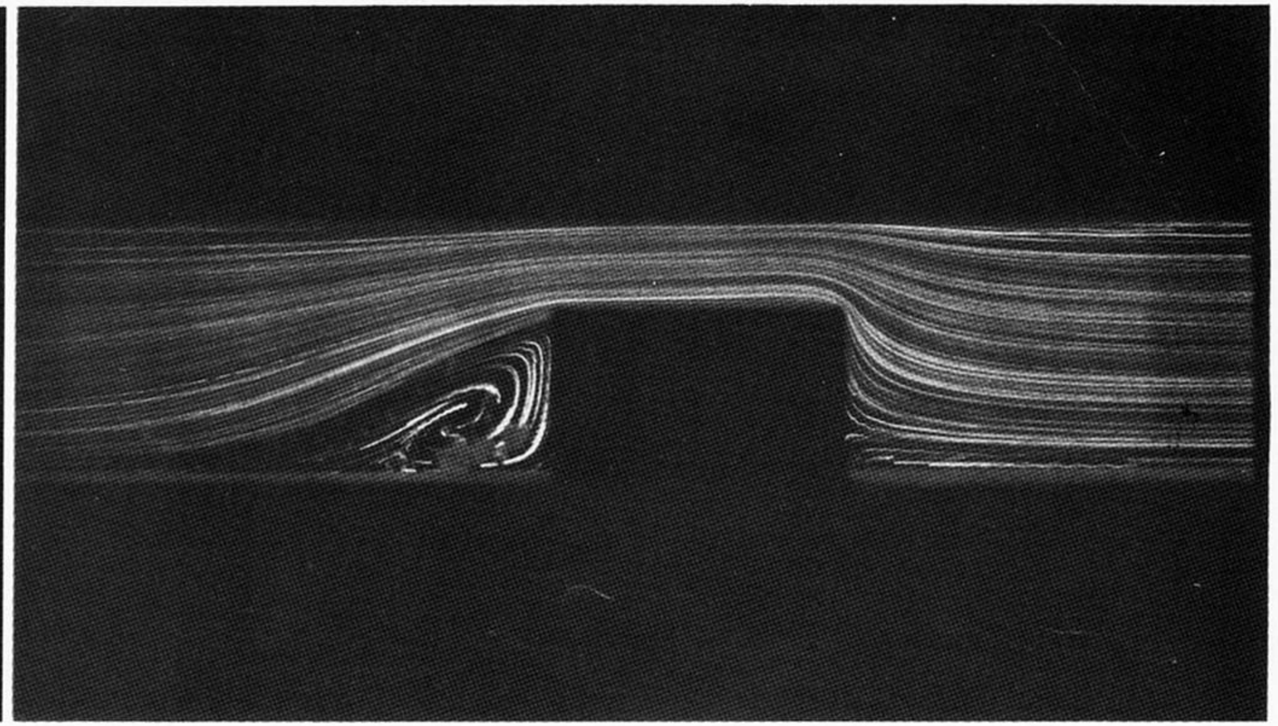

(b) $R=20, W=0.4$

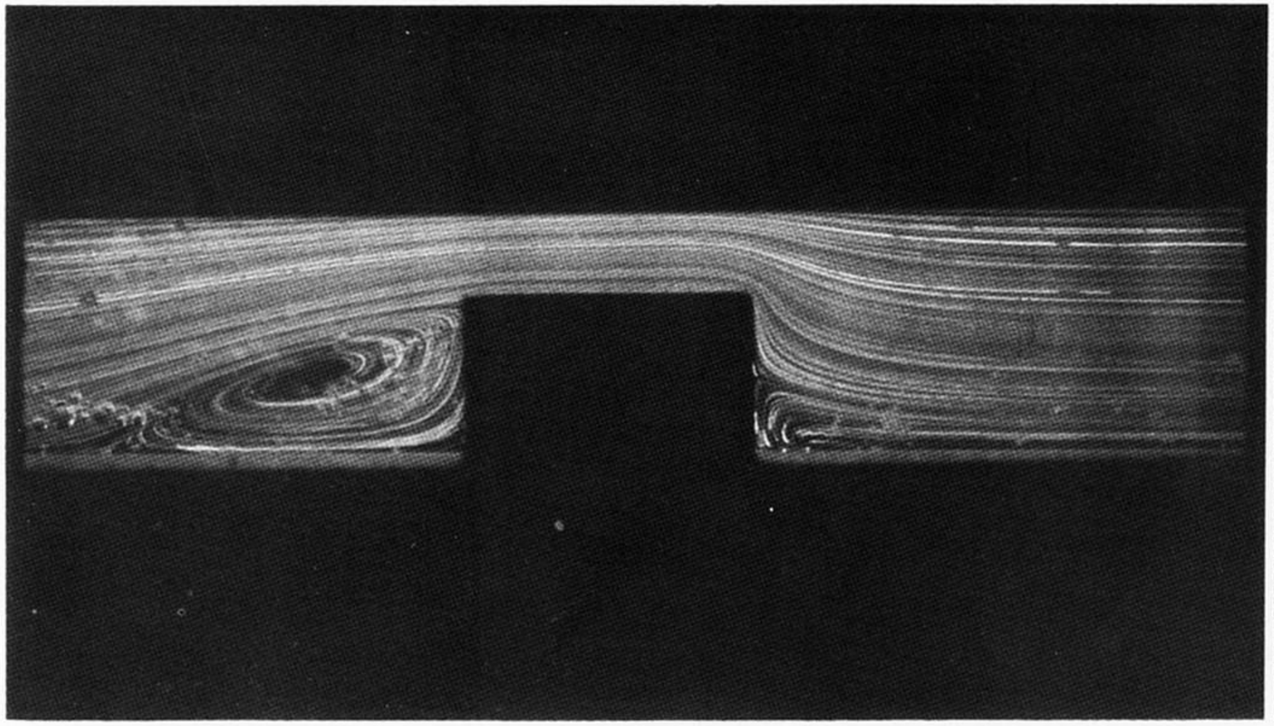

(c) $R=30, W=0$

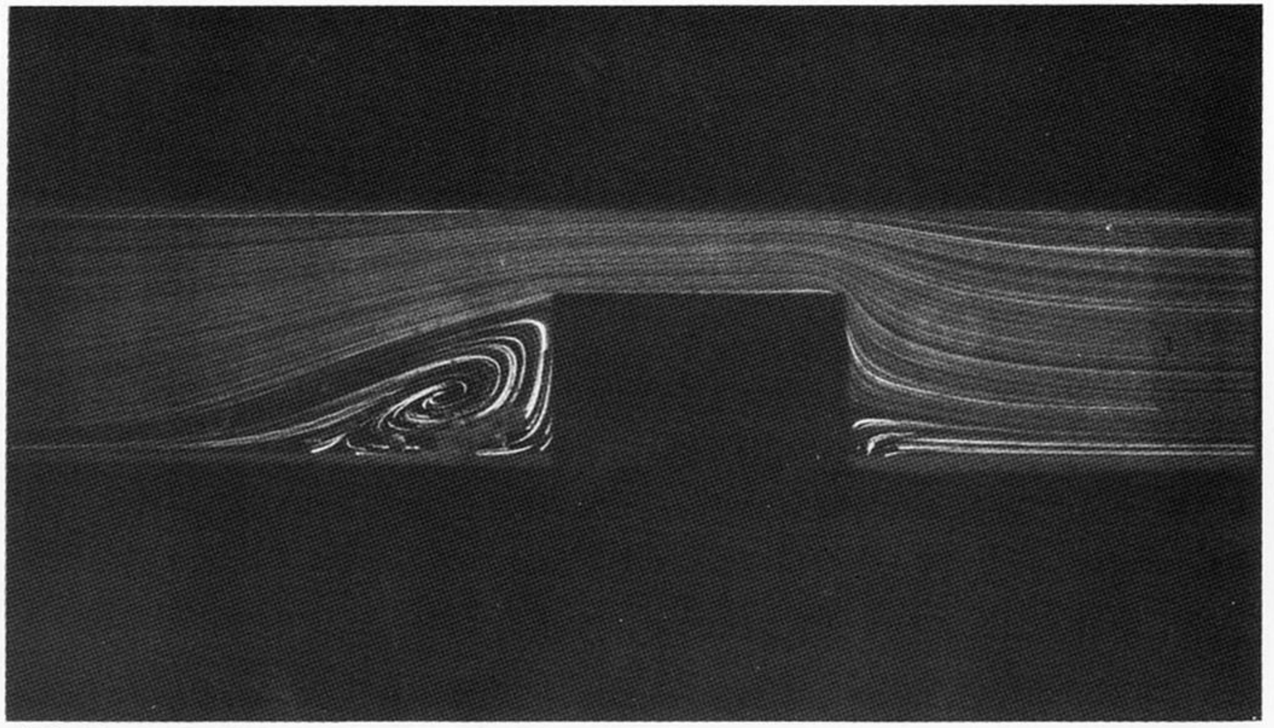

(d) $R=30, W=0.6$

FIGURE 10. Flow over a rectangular protuberance: (*a*) and (*c*) Newtonian, (*b*) and (*d*) liquid B1.

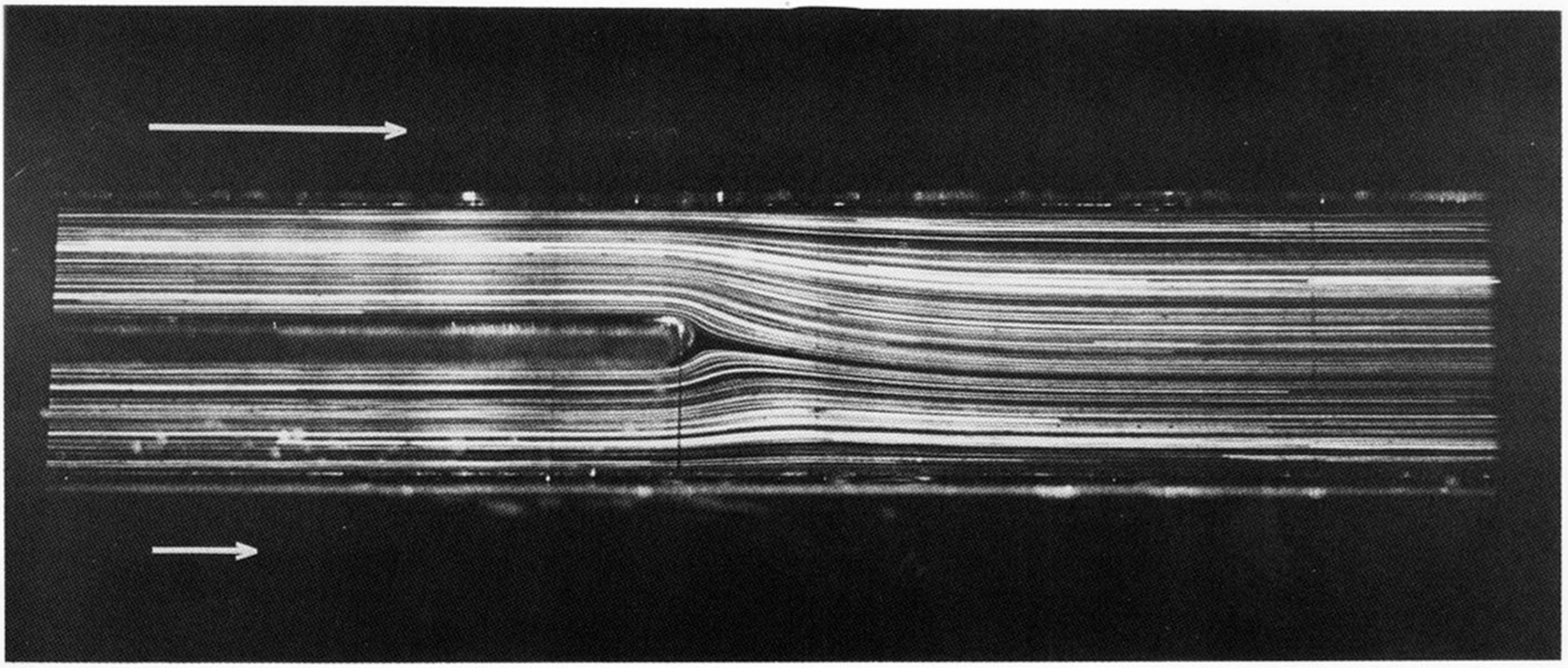

(*a*) $R=10, W=0$

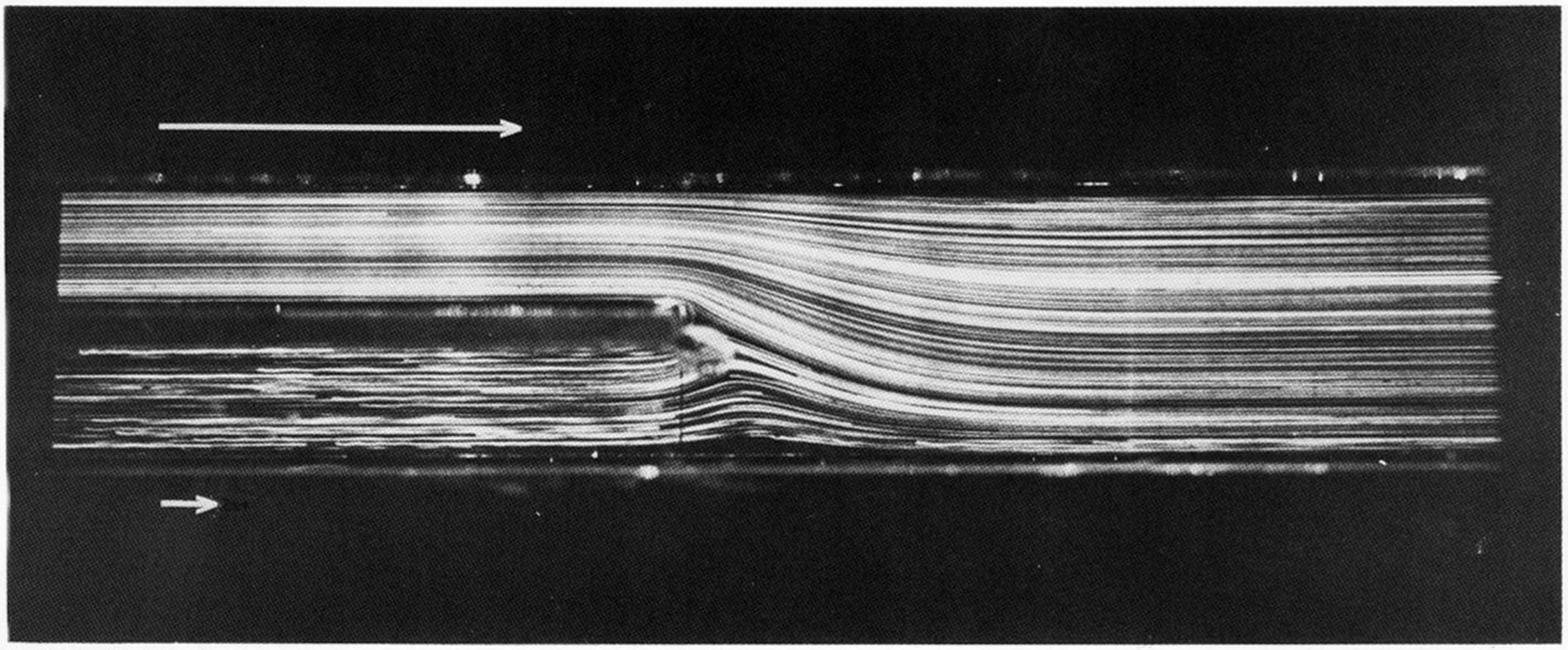

(*b*) $R=10, W=0$

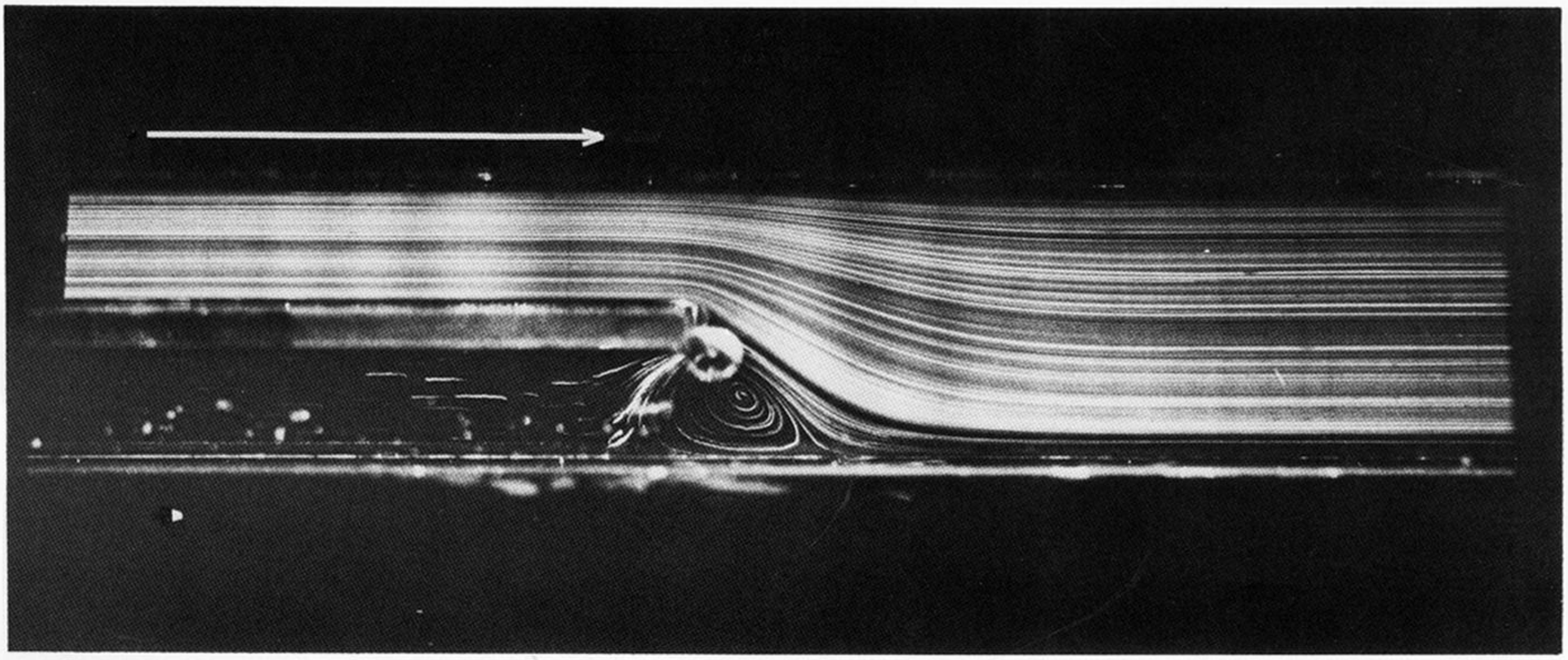

(*c*) $R=10, W=0$

FIGURE 11. Mixing flow: Newtonian liquid; ratio of flow rates is (*a*) 2:1, (*b*) 5:1, (*c*) 100:1; Reynolds number based on flow in wider channel.

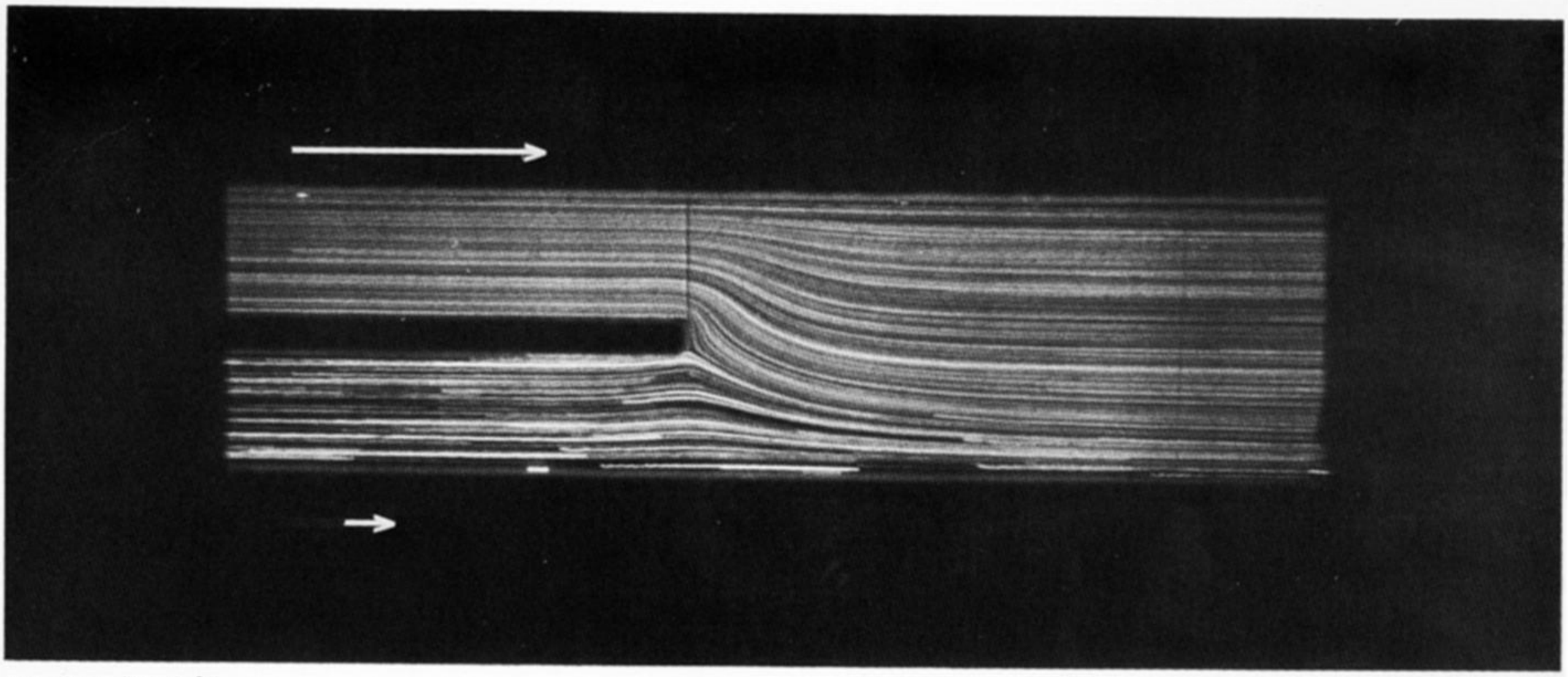

(*a*) $R=5, W=0.25$

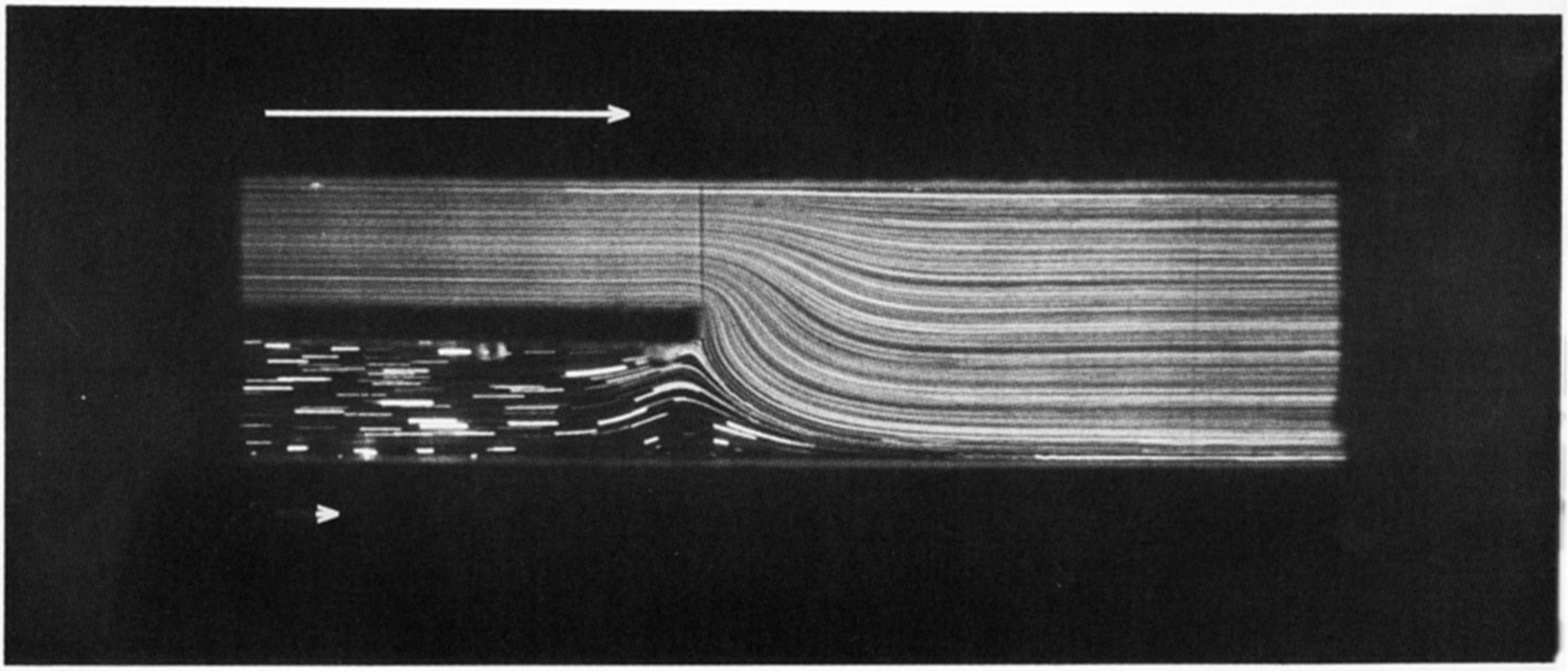

(*b*) $R=5, W=0.25$

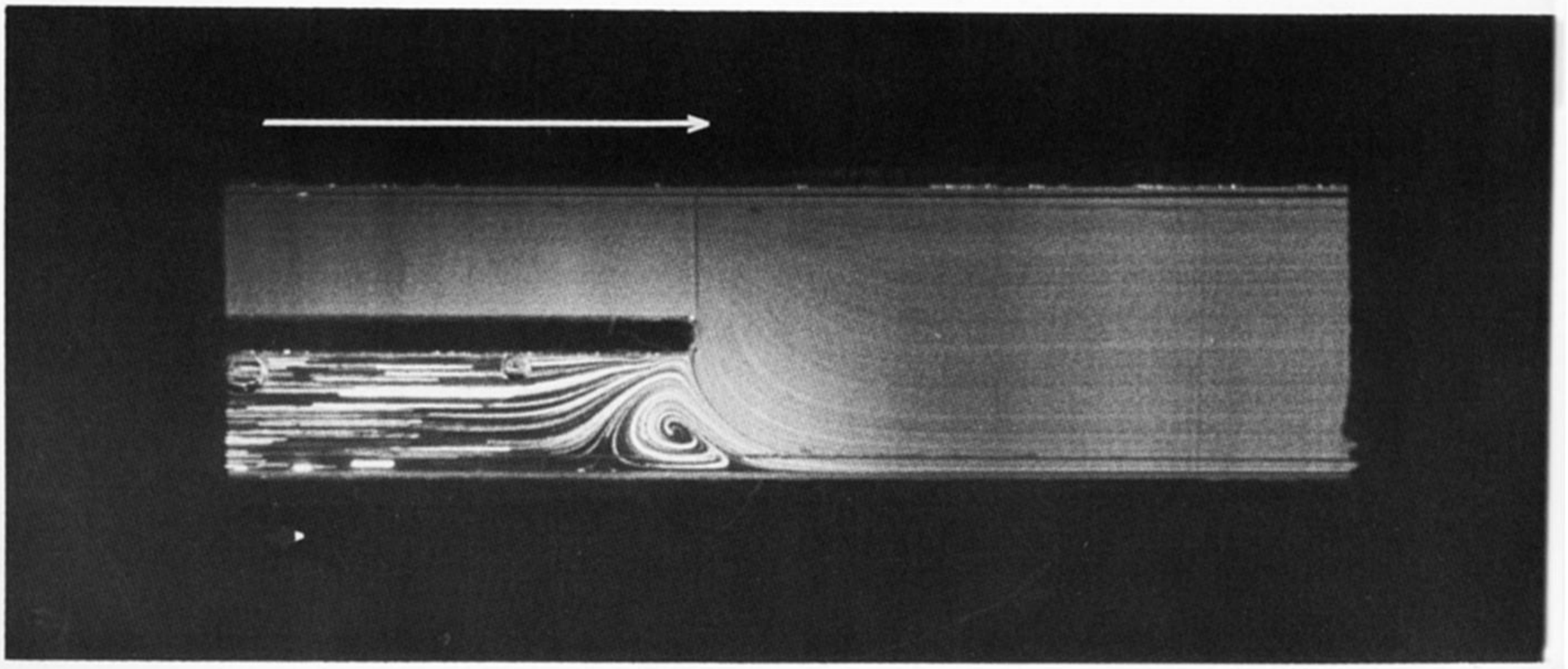

(*c*) $R=5, W=0.25$

FIGURE 12. Mixing flow: liquid B2; ratio of flow rates is (*a*) 5:1, (*b*) 20:1, (*c*) 100:1; Reynolds number and Weissenberg number based on width of wider channel.

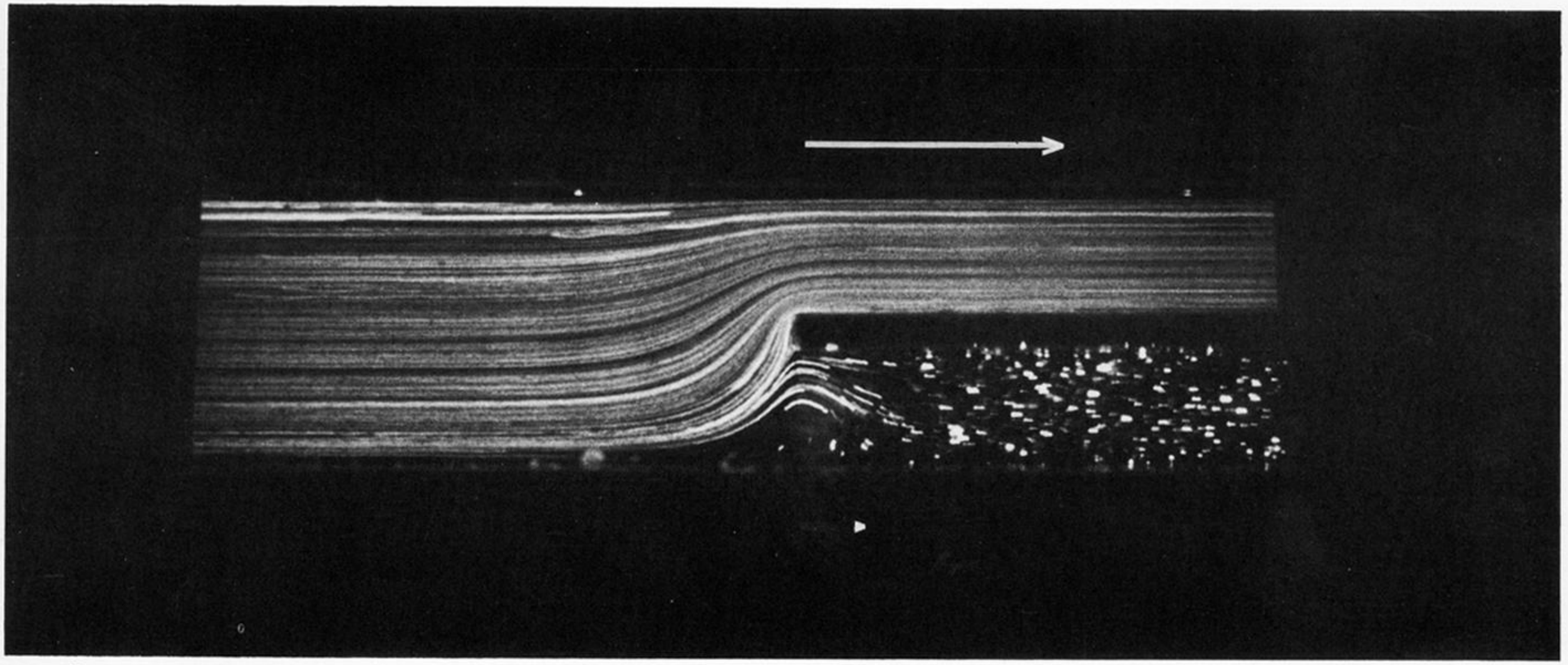

(*a*) $R=5, W=0$

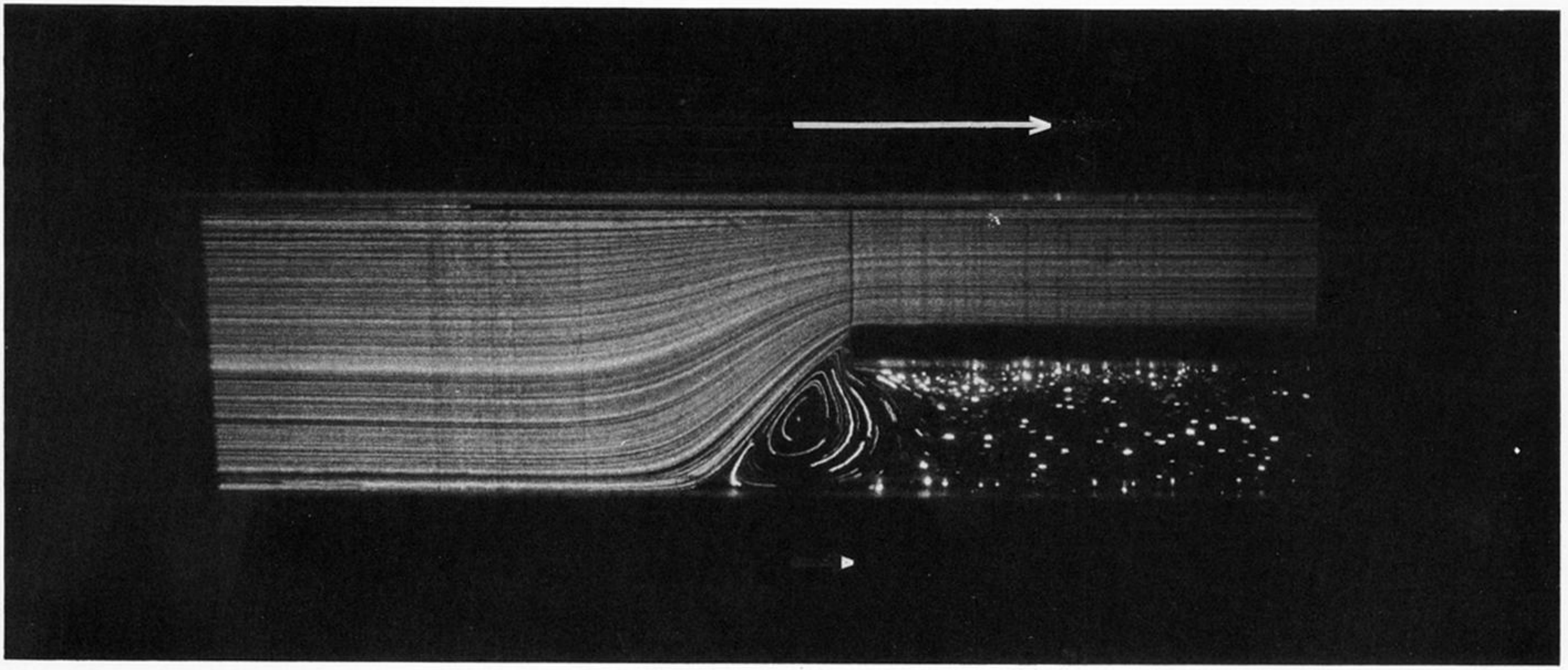

(*b*) $R=5, W=0.25$

FIGURE 13. Separating flow: (*a*) Newtonian liquid, (*b*) liquid B2; ratio of flow rates in the two arms is 100:1; Reynolds number and Weissenberg number based on width of wider channel.

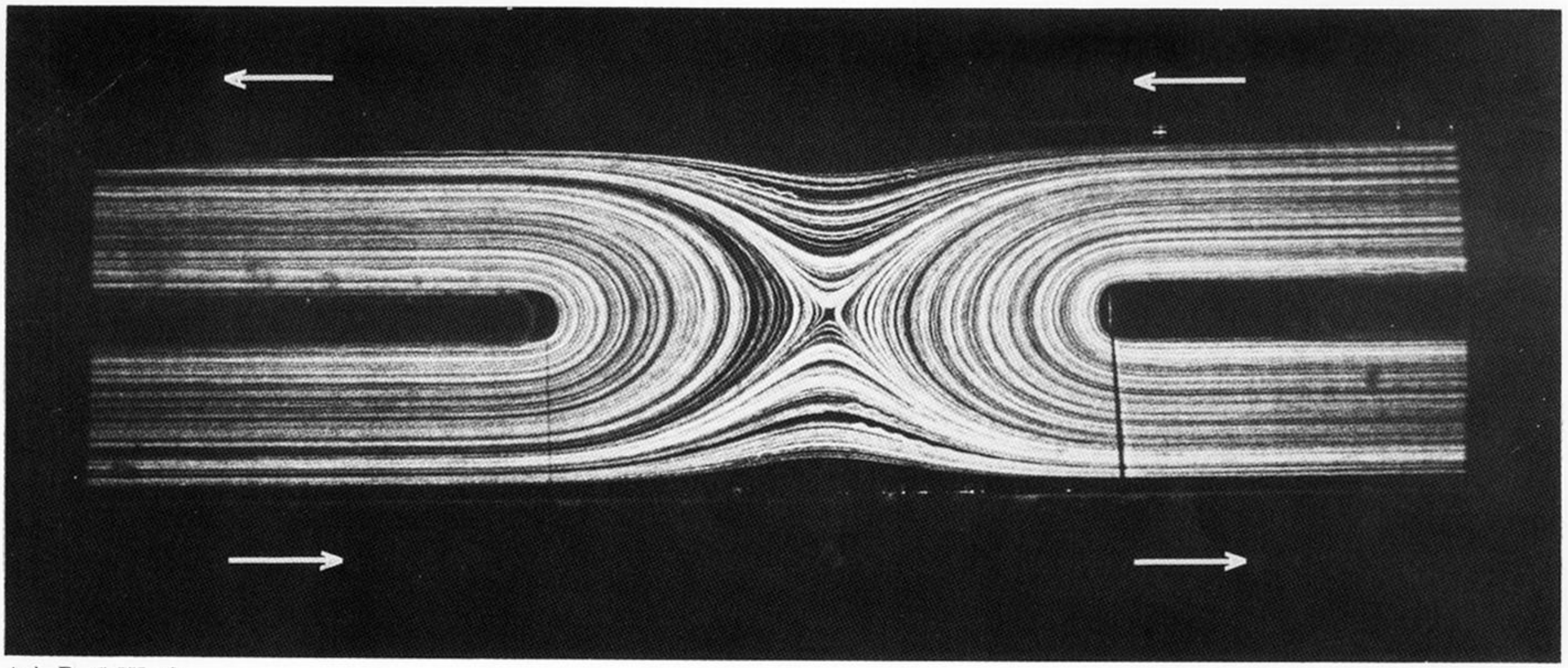

(*a*) $R=5, W=0$

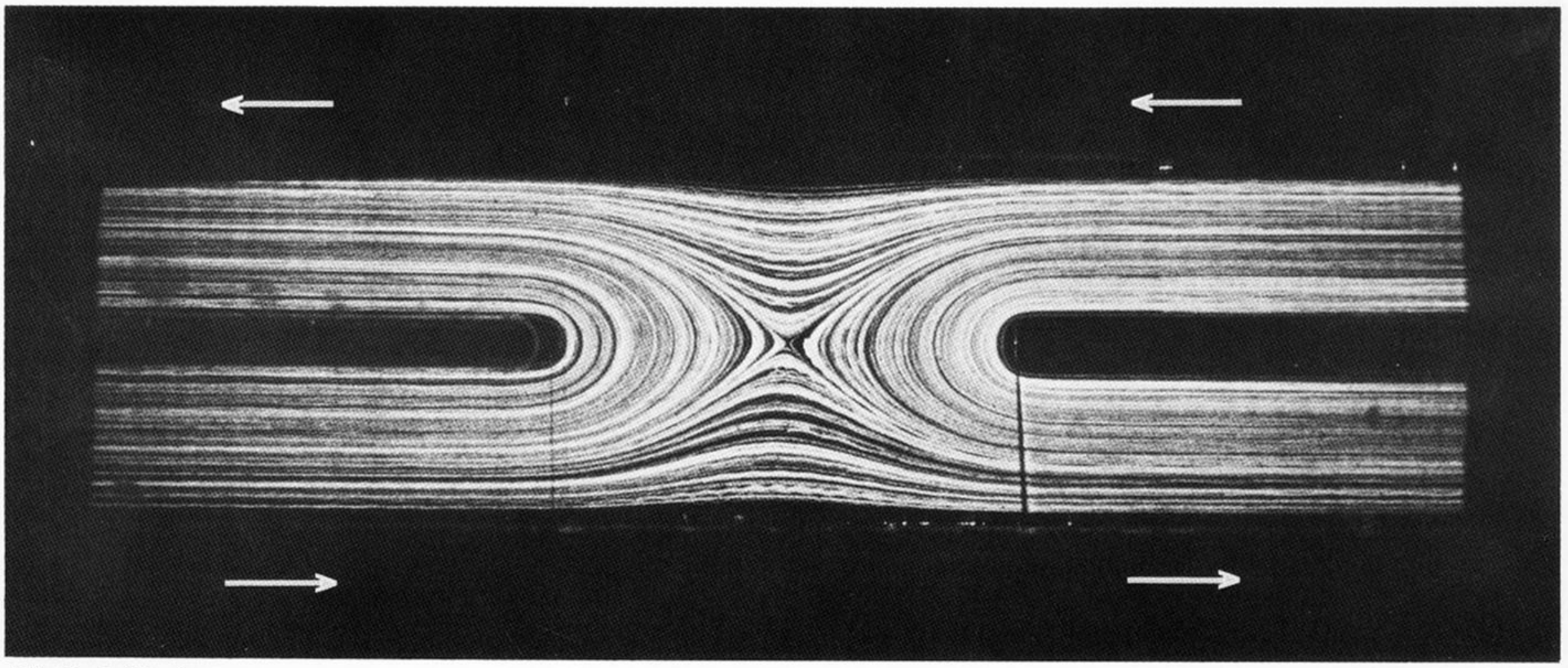

(*b*) $R=5, W=0$

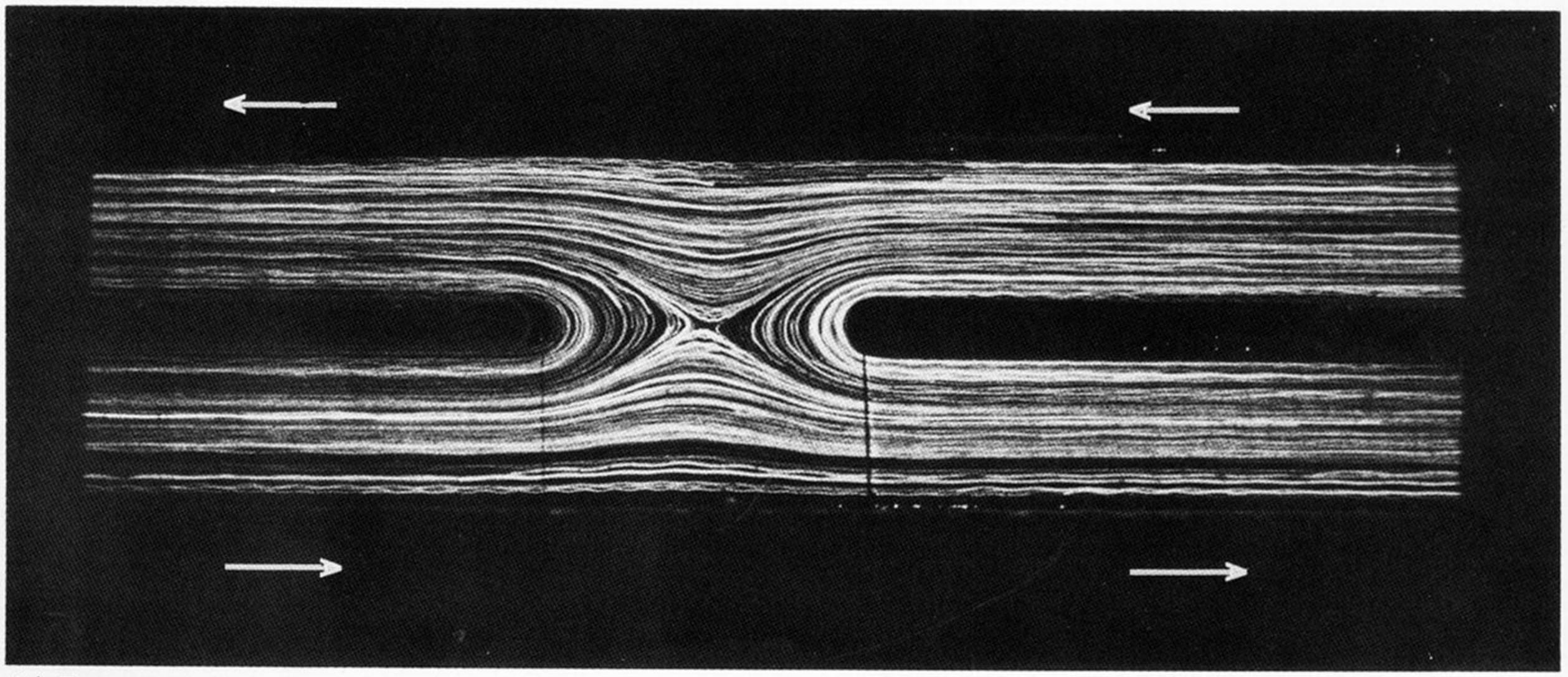

(*c*) $R=5, W=0$

FIGURE 14. Combined mixing and separating flow: Newtonian liquid; variable gap l, (*a*) $l = 18$ mm, (*b*) $l = 15$ mm, (*c*) $l = 10$ mm; flow rate in all arms equal; Reynolds number based on flow in one of the arms.

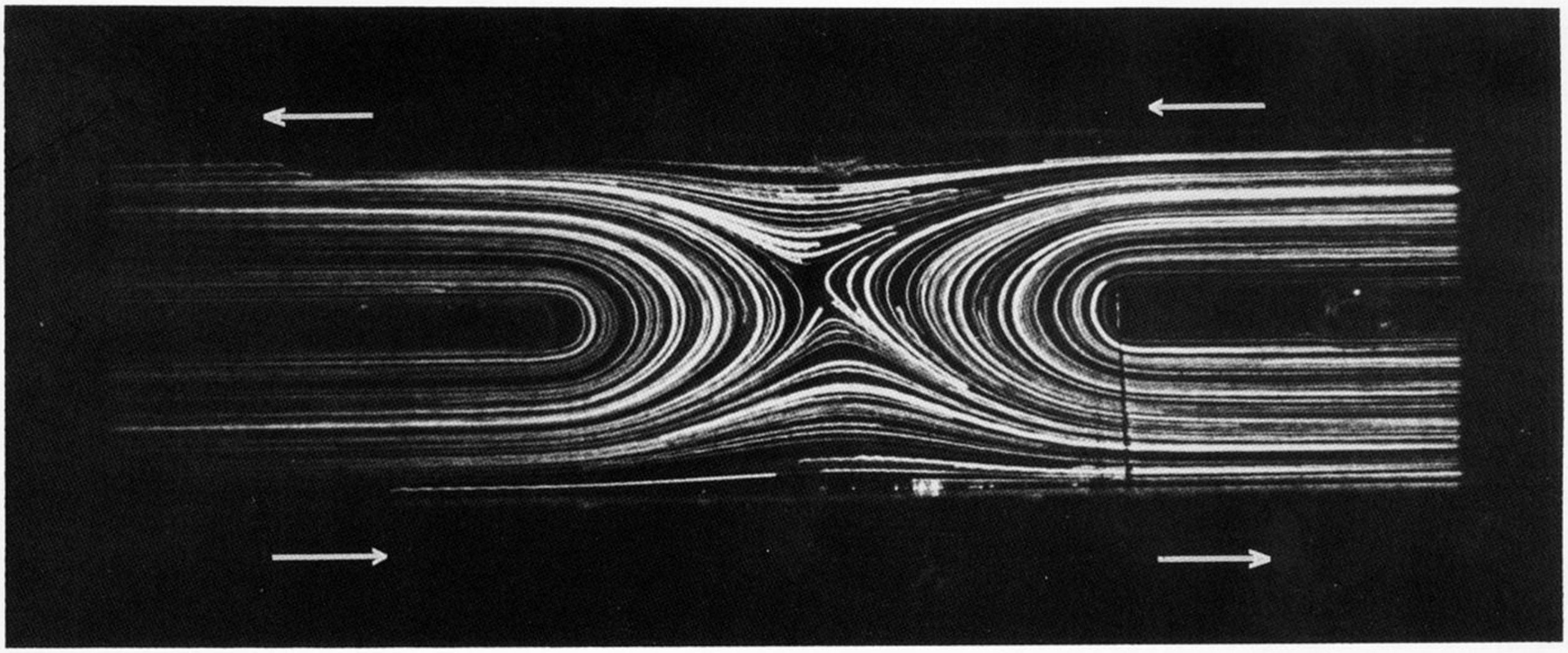

(*a*) $R=5, W=0.75$

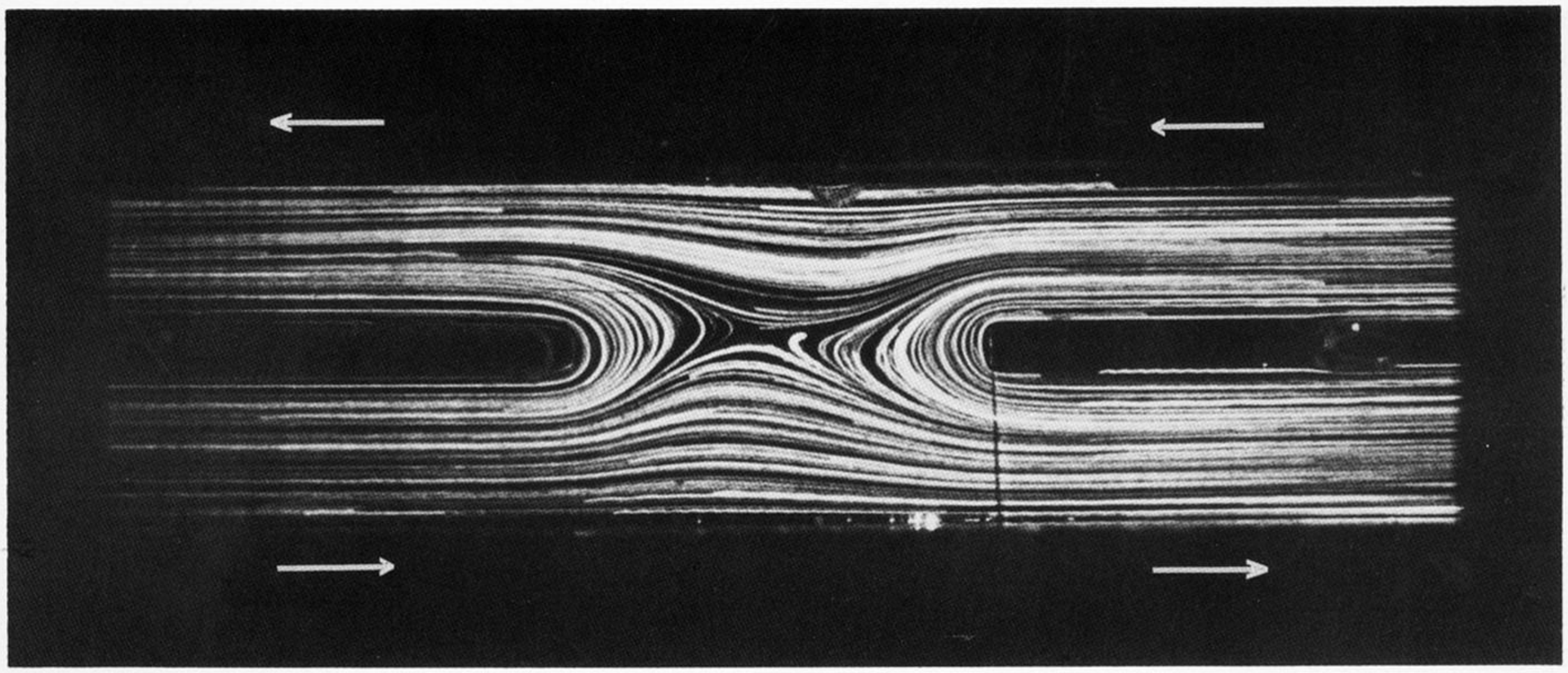

(*b*) $R=5, W=0.75$

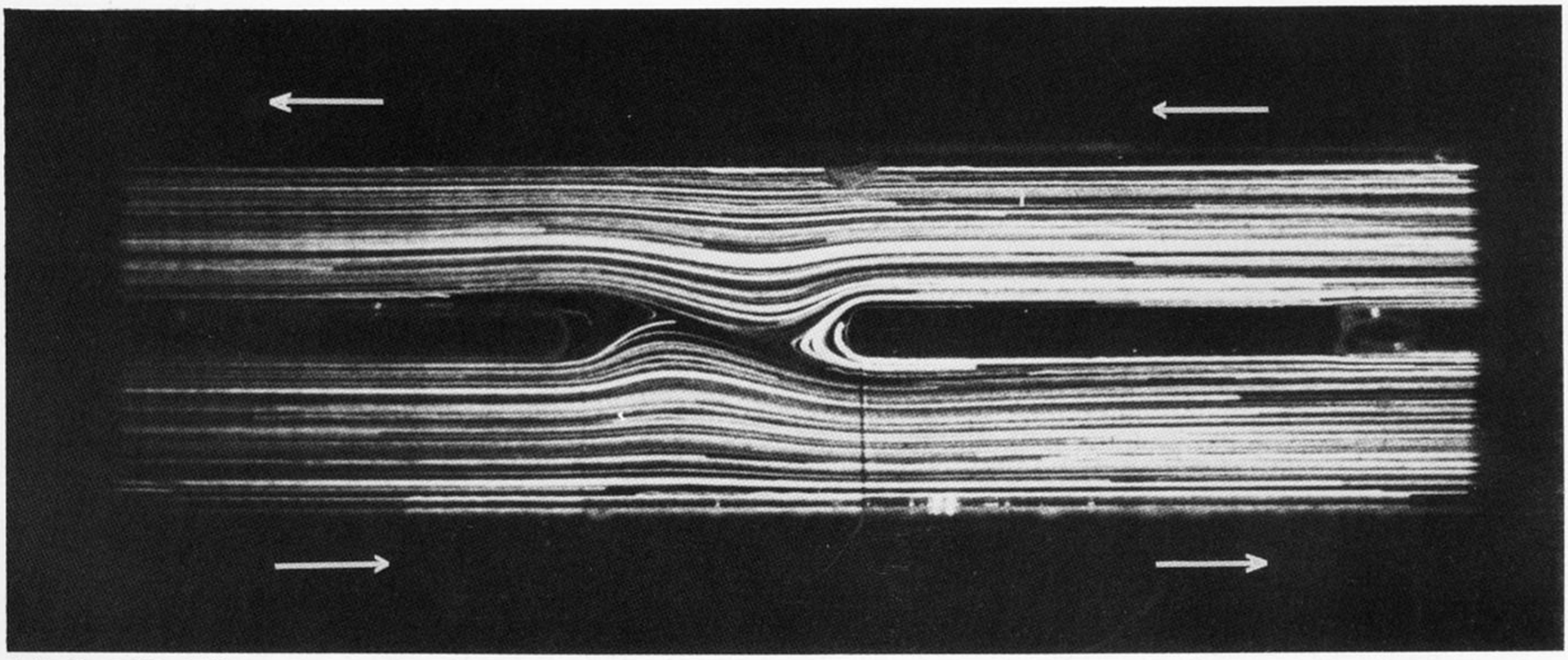

(*c*) $R=5, W=0.75$

FIGURE 15. Combined mixing and separating flow: as for figure 14 with liquid B3; Reynolds number and Weissenberg number based on width of one of the arms.

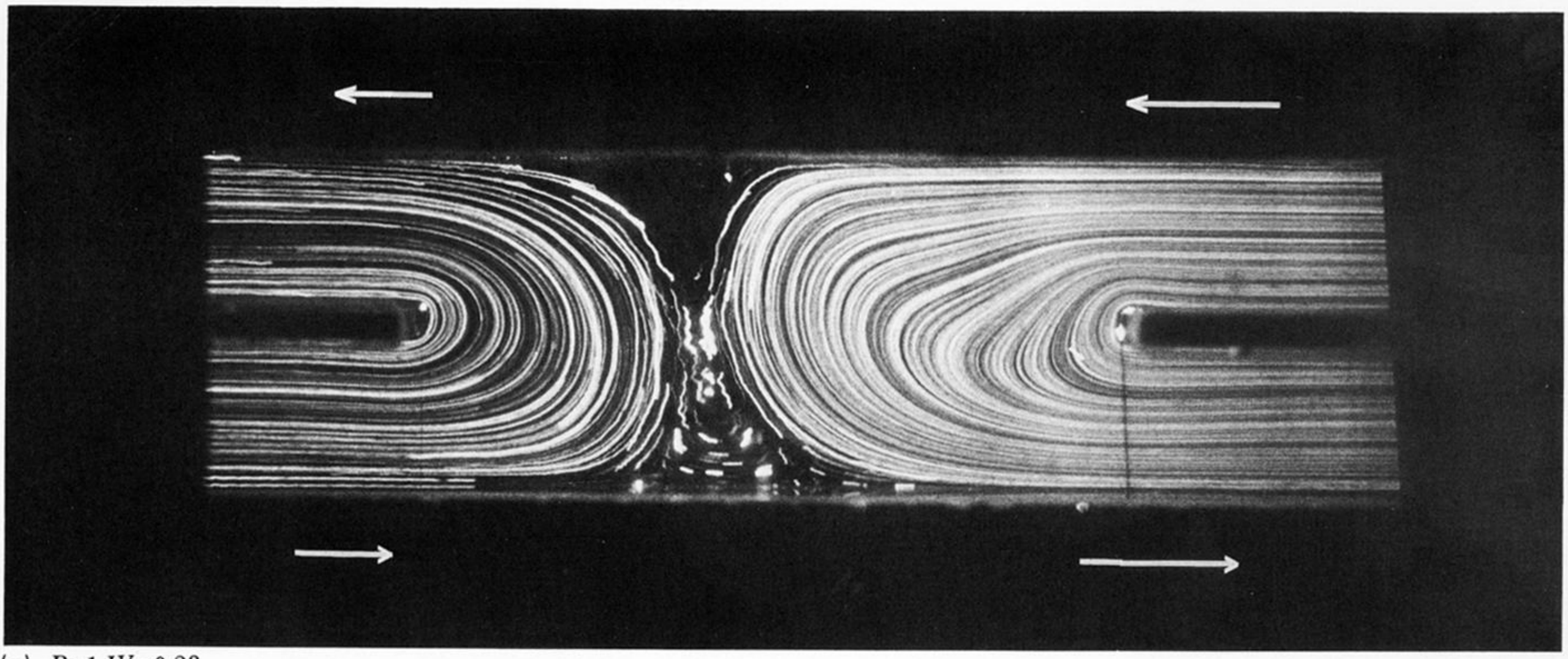

(*a*) $R=1, W=0.23$

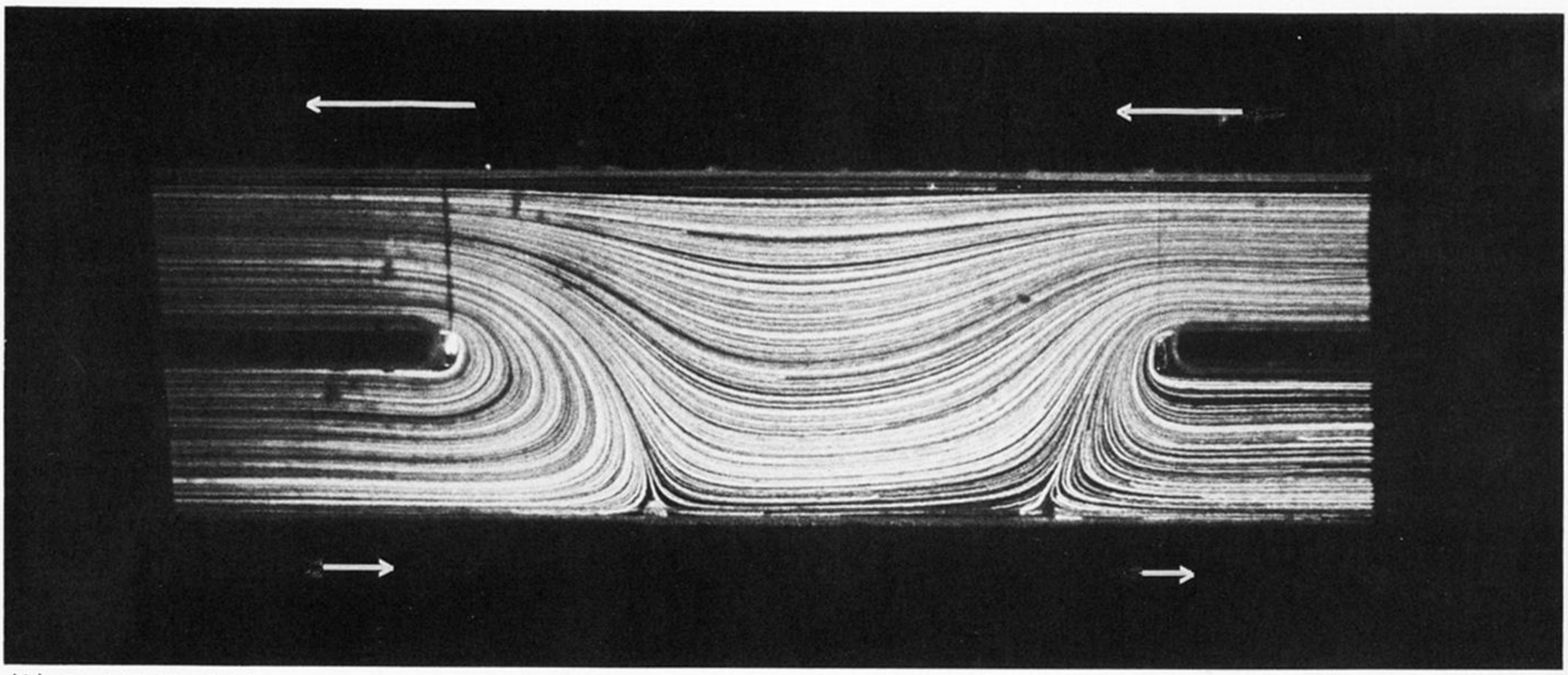

(*b*) $R=0.75, W=0.17$

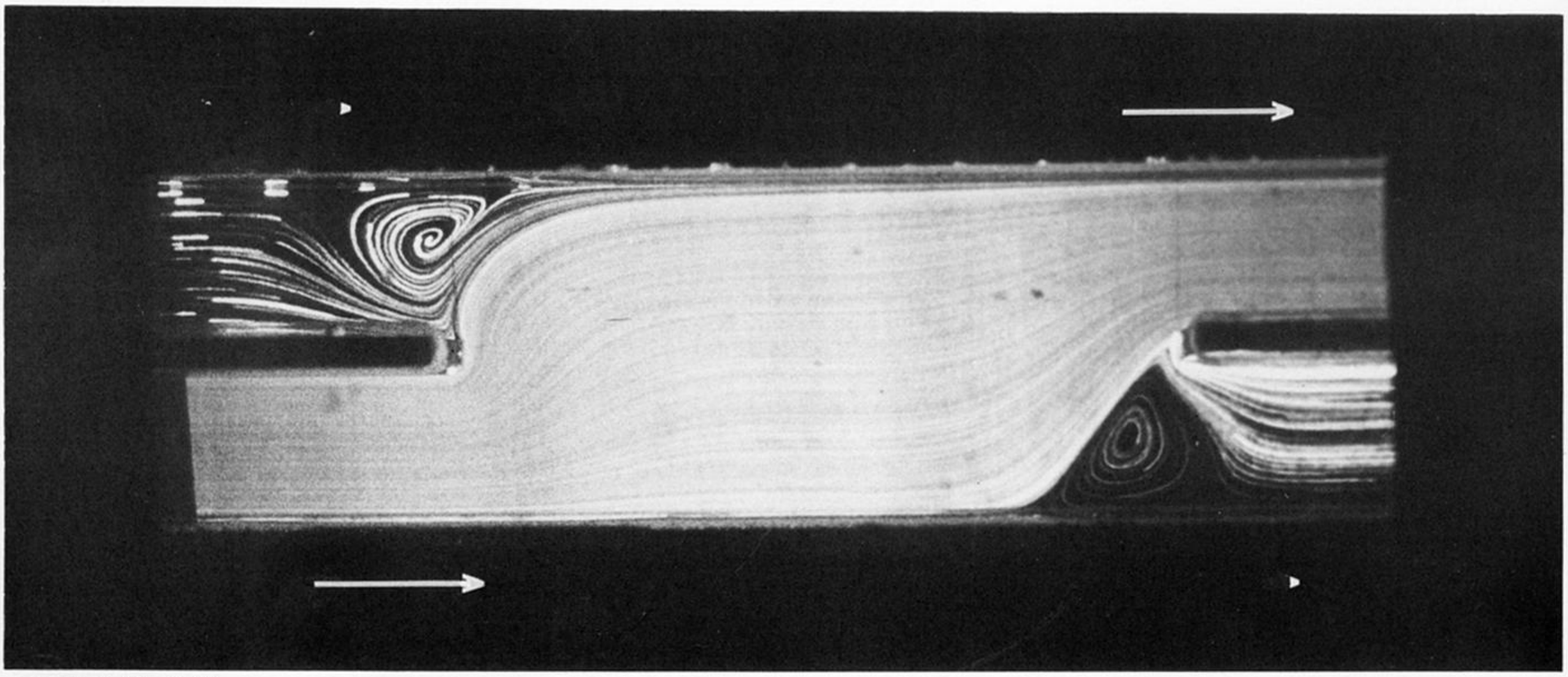

(*c*) $R=1, W=0.23$

FIGURE 16. Combined mixing and separating flow: liquid B2; gap $l = 25$ mm; relative flow rates indicated by lengths of arrows; Reynolds number and Weissenberg number based on flow rate measurement in upper right arm.

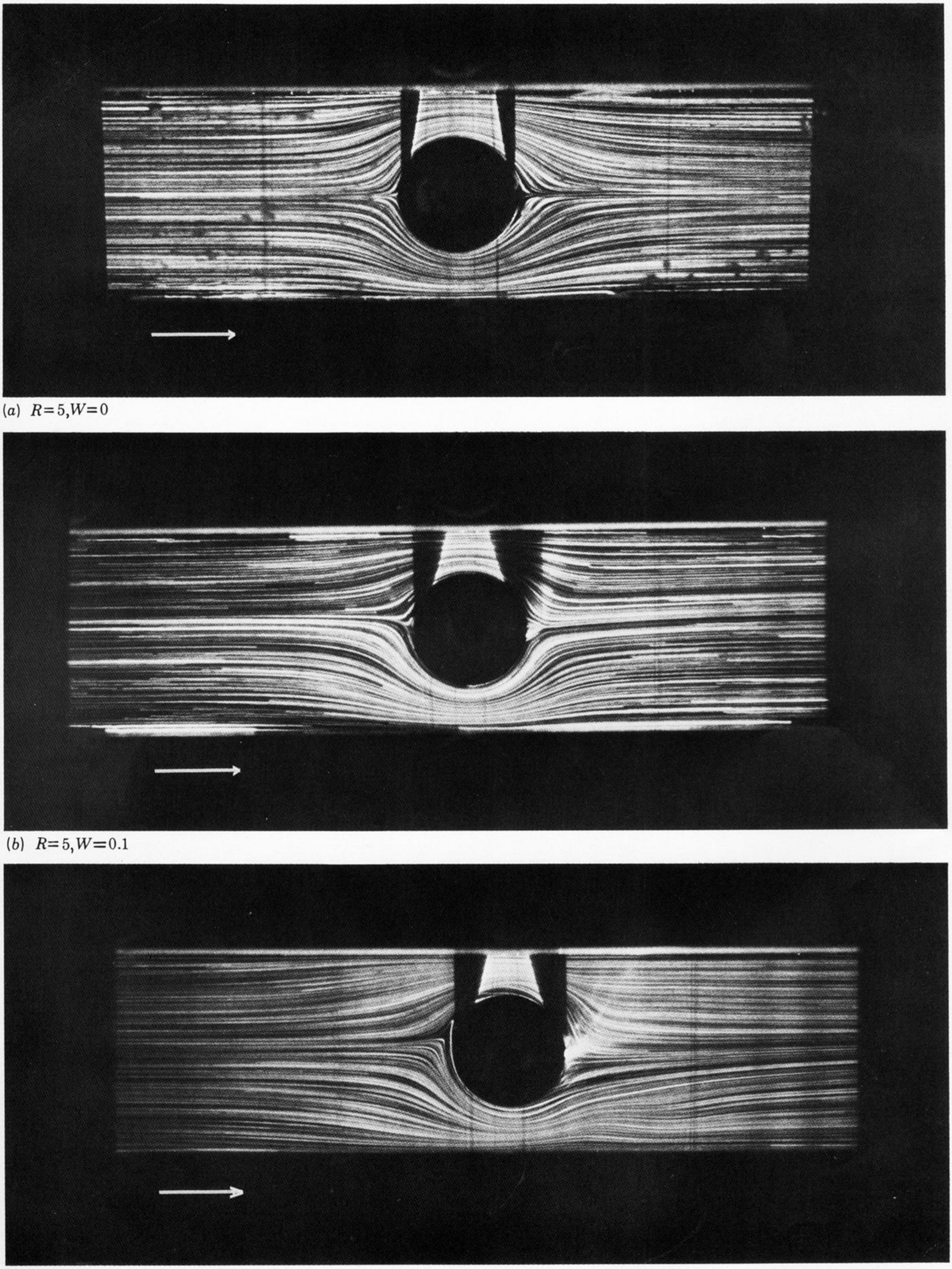

(*a*) $R=5, W=0$

(*b*) $R=5, W=0.1$

(*c*) $R=10, W=0.2$

FIGURE 17. Flow past a cylinder: (*a*) Newtonian, (*b*) and (*c*) liquid B1.